
**Plasmonic Generation of Attosecond
Pulses and Attosecond Imaging of
Surface Plasmons.
Modeling and Simulation of Experimental
Proposals.**

Mattia Lupetti

Dissertation in Cotutelle
an der Fakultät für Physik der Ludwig–Maximilians–Universität München,
Betreuer Prof. Dr. Armin Scrinzi,

und

an der Fakultät für Mathematik der Universität Wien,
Betreuer Prof. Dr. Norbert Mauser,

vorgelegt von
Mattia Lupetti
aus Montegranaro, Italien

Erstgutachter: Prof. Dr. Armin Scrinzi (LMU München)

Zweitgutachter: Prof. Dr. Norbert Mauser (Univ. Wien)

Beurteiler (Univ. Wien): Prof. Dr. Peter Hommelhof (Univ. Erlangen)

Beurteilerin (Univ. Wien): Prof. Dr. Mechthild Thalhammer (Univ. Innsbruck)

München und Wien, 11.5.2015

Tag der mündlichen Prüfung: 8.6.2015

Dedicated to my fiancée

Contents

Zusammenfassung	vii
Summary	viii
1 Introduction	1
2 Attosecond Physics	5
2.1 Three step model	6
2.2 Attosecond pulse generation	8
2.3 Attosecond Streak Camera	10
3 Surface Plasmon Polaritons	13
3.1 Classical theory of SPPs	14
3.1.1 SPPs as poles of the complex reflection coefficient	16
3.2 Quantum theory of SPPs	18
3.2.1 Random Phase Approximation (RPA)	22
3.2.2 Wave function of the plasmon state	28
3.3 Excitation of SPPs	31
3.4 Ultrafast plasmon dynamics	34
3.5 Standard SPP imaging techniques	36
3.6 Plasmonics in attosecond physics	40
4 A Plasmon Enhanced Attosecond Extreme Ultraviolet Source	45
4.1 Bow-tie structures for plasmonic enhanced HHG	46
4.2 Tapered plasmonic waveguides for HHG	47
4.3 Analysis of cylinder plasmon polaritons	48
4.3.1 Propagation in hollow waveguides	51
4.4 Geometry of the tapered waveguide	52
4.5 Waveguiding of XUV pulses by the waveguide	54
4.6 PEAX temporal characterization	58
4.7 PEAX spatial properties	61
4.8 Comparison with standard gas harmonics	62
4.9 Discussion and experimental issues	63
5 Attosecond Photoscopy of Surface Excitations	65
5.1 Experimental setup	66
5.2 Theory of attosecond photoscopy	67
5.3 Low-speed approximation	69

5.4	Approximation of the photoelectron distribution function	71
5.4.1	Unidirectional distribution of the photoelectrons	71
5.4.2	Isotropic distribution of the photoelectrons	72
5.5	Numerical simulation of the photoscopic spectrogram	72
5.6	Analytic model for the SPP field on a grating	74
5.7	Origin of the dark and bright modes	77
5.8	Results	78
6	Modeling and Simulation of SPPs	81
6.1	Limitations of PMLs	83
6.2	Exterior Complex Scaling (ECS)	83
6.3	Scaling of Maxwell's equations	85
6.4	Numerical implementation of 1D scaling	88
6.5	Maxwell's equations in two dimensions	90
7	Conclusions	91
A	Check of the numerics for the attosecond photoscopy technique	93
	Bibliography	95
	Acknowledgments	104

Zusammenfassung

Attosekundenpulse sind ultrakurze extrem-ultraviolette (XUV) Pulse, die durch einen nicht-linearen, von einer nah-infraroten (NIR) Laserquelle stimulierten Anregungsprozess erzeugt werden. Attosekundenpulse können verwendet werden, um die Elektronendynamik eines ultraschnellen Prozesses durch die “Attosecond Streaking” Technik zu messen, mit einer Auflösung auf der Attosekundenskala. In dieser Dissertation wird gezeigt, dass sowohl die Erzeugung von Attosekundenpulsen als auch die Messung ultraschneller Prozesse mittels Attosekundenpulse auf Fälle erweitert werden können, bei denen die Anregungs- und Streakingsfelder von Oberflächenplasmonen generiert werden, welche bei nahinfraroten Wellenlängen auf Nanostrukturen angeregt werden. Oberflächenplasmonen sind optische Moden, die aus einer kollektiven Schwingung der Elektronen an der Oberfläche in Resonanz mit einer externen Quelle entstehen.

Im ersten Abschnitt dieser Dissertation wird das Konzept der High Harmonic Generation (HHG) in plasmonisch erhöhten Feldern, wie in Ref. [Par+11] vorgeschlagen, durch numerische Simulationen analysiert. Ein NIR Puls wird mit einem Oberflächenplasmon, das sich in einem konischen, mit Edelgas gefüllten, Hohlleiter ausbreitet, gekoppelt. Die Intensität des plasmonischen Feldes steigt mit der Verringerung des Durchmessers des Hohlleiters, sodass die Felderhöhung an seiner Spitze groß genug wird, um hohe harmonische Strahlung zu generieren. In Ref. [LKS13] wird nachgewiesen, dass die Herstellung von isolierten Attosekundenpulsen mit außergewöhnlichen Zeit- und Raumstrukturen möglich ist. Trotzdem ist deren Intensität um mehrere Größenordnungen niedriger als die, die in Experimenten mit fokussierten Laserpulsen erreicht werden kann.

Im zweiten Abschnitt wird eine experimentelle Technik für die Abbildung plasmonischer Oberflächenanregungen vorgeschlagen [Lup+14], wobei Attosekundenpulse verwendet werden, um das Feld an der Oberfläche mittels “Momentum Streaking” der photoionisierten Elektronen zu messen. Dieses Konzept ist eine Erweiterung der “Attosecond Streak Camera” [Kie+04], welches ich “Attosecond Photoscopy” nenne. Es ermöglicht die Abbildung eines Plasmons in Zeit und Raum während des Anregungsprozesses. Anhand von numerischen Simulationen wird es gezeigt, dass die wesentlichen Parameter des plasmonischen Resonanzaufbaus mit subfemtosekunden-Präzision bestimmt werden können.

Zuletzt wird die Methode für die numerische Lösung der Maxwell-Gleichungen diskutiert, mit Fokus auf das Problem der absorbierenden Randbedingungen. Neue Einsichten in die mathematische Formulierung der Randbedingungen der Maxwell-Gleichungen werden vorgestellt.

Summary

Attosecond pulses are ultrashort radiation bursts produced via high harmonic generation (HHG) during a highly nonlinear excitation process driven by a near infrared (NIR) laser pulse. Attosecond pulses can be used to probe the electron dynamics in ultrafast processes via the attosecond streaking technique [Gou+04], with a resolution on the attosecond time scale. In this thesis it is shown that both the generation of attosecond (AS) pulses and the probing of ultrafast processes by means of AS pulses, can be extended to cases in which the respective driving and streaking fields are produced by surface plasmons excited on nanostructures at NIR wavelengths. Surface plasmons are optical modes generated by collective oscillations of the surface electrons in resonance with an external source.

In the first part of this thesis, the idea of high harmonic generation (HHG) in the enhanced field of a surface plasmon proposed in [Par+11] is analyzed in detail by means of numerical simulations. A NIR pulse is coupled into a surface plasmon propagating in a hollow core tapered waveguide filled with noble gas. The plasmon field intensity increases for decreasing waveguide radius, such that at the apex the field enhancement is sufficient for producing high harmonic radiation. It is shown [LKS13] that with this setup it is possible to generate isolated AS pulses with outstanding spatial and temporal structure, but with an intensity of orders of magnitude smaller than in standard gas harmonic arrangements.

In the second part, an experimental technique for the imaging of surface plasmonic excitations on nanostructured surfaces is proposed [Lup+14], where AS pulses are used to probe the surface field by means of photoionization. The concept constitutes an extension of the attosecond streak camera [Kie+04] to “Attosecond Photoscopy”, which allows space- and time-resolved imaging of the plasmon dynamics during the excitation process. It is numerically demonstrated that the relevant parameters of the plasmonic resonance buildup phase can be determined with subfemtosecond precision.

Finally, the method used for the numerical solution of the Maxwell’s equations is discussed, with particular attention to the problem of absorbing boundary conditions. New insights into the mathematical formulation of the absorbing boundary conditions for Maxwell’s equations are provided.

List of Publications

This work is based on the following publications.

1. Lupetti, M., Kling, M. F., and Scrinzi, A. (2013). Plasmon- Enhanced-Attosecond-Extreme Ultraviolet Source. *Physical Review Letters*, 110 (22):223903
2. Lupetti, M., Hengster, J., Uphues, T., and Scrinzi, A. (2014). Attosecond Photography of Plasmonic Excitations. *Physical Review Letters*, 113(11):113903
3. Lupetti, M. and Scrinzi A. (2015). Attosecond XUV Pulses and Surface Plasmon Polaritons: Two Case Studies. *In: Kitzler, M. and Gräfe, S., ed. Ultrafast dynamics driven by intense light pulses. From atoms to solids, from lasers to intense X-rays.* Springer Series on Atomic, Optical, and Plasma Physics. *In publication.*

1

Introduction

The imaging of a physical process evolving with a given time scale has to be performed with a device, whose response time is smaller than that of the process under investigation.

The last decades have seen a very fast technological development in laser science and technique, such that accessing unprecedented timescales by appropriately fast devices has become feasible, and in some cases routine. This is for example the case of “femtochemistry”, where chemical reactions occurring at the femtosecond level ($1 \text{ fs} = 10^{-15}$ seconds) are “filmed” by means of even shorter laser pulses. Thanks to the emergence of widely tunable femtosecond laser pulses it was possible to gain understanding of ultrafast physical, chemical and biological processes.

However, while femtochemistry is able to resolve the dynamics in molecules, pure electronic motion occurs on a much shorter timescale, and therefore requires a much faster imaging technique, on the attosecond level ($1 \text{ as} = 10^{-3}$ fs, see Table (1.1)).

Table 1.1: Timescales of typical physical processes.

	ΔE	τ	Imaging technique
Man walking	Joule	1 s	Camera
Molecular vibrations	meV	100 fs	Femtosecond pulses
Outer electrons in atoms	1 – 20 eV	100 as	Attosecond streak camera
Debye screening in metals	1 – 10 eV	100 as	Attosecond photostopy
Inner electrons in atoms	10 – 100 keV	100 zs - 1 as	?
Nuclear fusion d-t	10 MeV	$\ll 1$ as	?

The capability of generating light sources short enough to allow the temporal investigation of sub-femtosecond dynamics is a relatively recent accomplishment, since in 2001 the generation of an isolated pulse of sub-femtosecond duration was experimentally demonstrated [Hen+01] for the first time. The breakthrough that set the physics community on the way to attosecond science though, dates back to 1979, when P. Agostini [Ago+79] discovered the phenomenon of above threshold ionization (ATI). In the experiment it was

shown that when an atom is ionized by a strong field, the photoelectron spectrum not only shows the expected peak corresponding to the minimum amount of photons required to overcome the ionization potential, but also extra peaks corresponding to higher multiples of the fundamental laser frequency. This feature of photoionization in strong field contradicted the common understanding of atomic physics, according to which an electron would gain just the amount of energy required to escape the atomic potential. The absorption of any additional number of photons would correspond to free-free transitions, which should have been forbidden by energy and momentum conservation.

In fact, a bound electron can gain as much energy as it is available, the probability amplitude for the absorption of a given amount of energy depending on the external field parameters. Moreover, it was later reported in [Pau+94] that the peak amplitudes in the photoelectron spectrum obtained in strong field ionization do not depend on the field intensity as I_0^{-n} , with n the number of photons absorbed. Rather, the spectrum presents a region where the peak amplitudes are constant over many harmonics of the fundamental frequency. The presence of a broad “plateau” region, together with the overcoming of the historical treatment of the photoelectric effect, set the basis for the development of a non-perturbative theory, which shifted the “ n -photon” picture paradigm towards a more intuitive description of the time dependent dynamics.

In the same decade, another phenomenon displaying striking similarities with ATI was discovered, namely the generation of high harmonics (HHG) in atoms irradiated with strong laser fields. Nowadays it is widely recognized that the physical process responsible for the ATI and HHG is the same one, an electron being ionized in a strong field and rescattering with the nucleus. A simple semi-classical model splitting the process in a sequence of ionization, acceleration and rescattering is able to capture the underlying physics, and will be discussed in Chapter 2.

It was soon realized that provided that the phases of the harmonics in HHG are coherent, the long sequence of equal amplitude harmonic orders could correspond to a train of pulses with attosecond duration in the time domain. As this was later demonstrated in [Pau+01], it was also understood that for pump-probe spectroscopy spanning over time intervals longer than the temporal spacing between two consecutive pulses, isolated attosecond pulses (IAP) were required. As soon as single IAPs became available [Hen+01], a number of applications concerning the study of subfemtosecond motion were developed, from the imaging of valence electron motion in Krypton atoms [Gou+10] to the measurement of emission delays from different bands of bulk Tungsten [Cav+07].

Recently, the curiosity of the attosecond community is focusing on ultrafast phenomena in solids. The recent demonstration of the optical control of ultrafast electron currents in a dielectric medium [Sch+13], is a confirmation of this interest shift. The work of this thesis follows this direction, its aim being bringing together the attosecond world, comprising of generation mechanism and diagnostic application, with *plasmonics*. Plasmonics is the field that studies optical excitations at metal surfaces, e.g. nanospheres, nanowires, or nanostructured interfaces. The word “nano” is often associated with plasmonics because of its

capability to confine an optical field down to the nanometric scale. Plasmonic excitations are collective oscillations of the surface electrons driven by an external field. These oscillations are typically associated with macroscopic features, most notably the aforementioned field confinement, and field enhancement in proximity of the supporting surface. For these reasons, surface plasmons are studied for a broad number of technological applications, ranging from plasmonic circuitry for plasmonic-based computer chips [Ozb06], to Surface Enhanced Raman Scattering (SERS) for biological molecule sensing [Sha+12].

Surface plasmons were first observed as “anomalies” in the reflectivity spectrum of diffraction gratings by Wood [Woo02], in 1902, while the first theoretical understanding occurred only in 1941, when Fano explained the dips in the spectrum as due to resonant excitations of surface waves [Fan41]. The explanation of the grating anomalies in terms of surface plasmonic resonances was given for the first time in [Rit+68], where the optical properties of metal surfaces were related to the microscopic theory of electronic excitations in solids. This work set the basis for a modern understanding of surface plasmons in terms of solid state physics.

The Thesis is essentially composed of two parts, as its title tries to convey, and follows the typical dual scenario of attosecond physics, i.e. that a process generating attosecond pulses can be time resolved by the generated AS pulses themselves. In this sense, the first part is dedicated to the modelling and numerical analysis of HHG using plasmonic enhancement as an amplifying mechanism for the driver NIR laser. To this purpose, a plasmonic tapered waveguide is used, where an ultrashort linearly polarized NIR laser pulse is coupled to a plasmonic mode, which provides the necessary enhancement to produce high harmonics in the XUV regime. This idea, first proposed in [Par+11], has the advantage of not requiring any complex amplification chain for the driver NIR pulse, allowing to directly use commercially available lasers and keeping the repetition rate unaltered. In the numerical analysis described in Chapter 4 it is shown that with such a technique isolated attosecond pulses displaying outstanding temporal and spatial collimation properties can be produced, and a comparison with standard generation techniques is discussed. It is found that plasmonic generated pulses are weaker than traditionally generated ones, but nevertheless their very good characteristics make them a valuable alternative in terms of simple usage and costs.

Secondly, the application of attosecond pulses as imaging tools for surface plasmons polaritons (SPPs) propagating on nanostructured surfaces is investigated. A new technique called attosecond photocopy [Lup+14] and based on a pump-probe measurement, SPP pump with XUV IAP probe, is proposed, which allows to fully characterize the temporal evolution of the buildup dynamics of the plasmonic resonance, using only already existing tools of attosecond metrology. The technique can be easily extended to any kind of surface plasmonic excitation. Recent developments of the experimental apparatuses indicate the possibility to spatially separate the XUV and NIR pulse while keeping the attosecond-precise synchronization. The validity of the proposed technique is checked by numerical simulations, and it is shown to provide time- *and space*-resolved imaging of virtually any

surface phenomena: by exciting a surface mode with a NIR pulse, one can tailor the dynamics of the excitation along complex nanostructured components by simply pointing the attosecond XUV pulse on the region of interest.

Finally, a discussion on the method for the numerical solution of Maxwell's equations (ME), a relevant part of the simulation work of this Thesis, is given. The most widespread method for solving the time dependent MEs is the so called Finite-Difference Time-Domain (FDTD) method [Taf05], which consists in the discretization of time and space via finite differences. The electric field \mathbf{E} and magnetic field \mathbf{B} are computed on a staggered grid, i.e. on two identical spatial and temporal grids which are shifted with respect to each other by half the discretization step. Although the broad success of the method in the physics and engineering community, few criticalities are present which mostly affect the way outwards propagating solutions are absorbed by boundary conditions set to avoid unwanted reflection in the simulation box. In the discussion in Chapter 6 the standard absorbing condition for time-dependent ME, called Perfectly-Matched-Layer (PML) [Ber94], is analyzed within the mathematical framework of Exterior Complex Scaling (ECS) [Sim79], which is known to be a rigorous and efficient method in the numerical solution of the time dependent Schrödinger equation (TDSE). Elaborating on the recent work of Ref. [SSM14], it is shown how an absorbing condition can be formulated for the case of MEs, setting the basis for a rigorous and efficient solution of the absorption problem.

The Thesis is organized as follows: in the first two chapters the fundamental concepts of attosecond physics (Chapter 2) and ultrafast plasmonics (Chapter 3) are introduced. In Chapter 4 the idea of plasmonic generation of attosecond pulses is analyzed from a numerical point of view, and a thorough discussion of its strengths and limitations is provided. Then, in Chapter 5 the attosecond photocopy technique is introduced and its features illustrated in details. After that, a discussion on the numerical solution of the Maxwell's equations, with particular regard to the mathematical formulation of absorbing boundary conditions, is given in Chapter 6. Finally, conclusions and a concise outlook of future perspectives are presented.

2

Attosecond Physics

In this chapter the key concepts of attosecond science are introduced.

The foundation of attosecond physics can be dated back to 1979, when in [Ago+79] the phenomenon of above threshold ionization (ATI) was discovered. In this work it was shown that an electron ionized from a noble gas atom via a multi-photon process experiences a number of free-free transitions, since the number of photons absorbed is larger than what required to overcome the ionization barrier. These findings were in contradiction with the acknowledged understanding of atomic physics of the time, according to which an electron would absorb only the amount of photons required to overcome the ionization potential. Any extra “free-free transition” would violate energy and momentum conservation. The whole misunderstanding came from the mindset towards atomic physics. Photo-absorption was considered a sequential process of transitions towards higher energy states, which explains the puzzlement about transitions between continuum states. In fact, it is true that a free electron cannot gain energy and momentum in a homogeneous external field, but it is wrong the idea that an electron absorbing an amount of energy larger than the ionization potential is a free electron. Indeed, thinking in classical terms, the stronger the field intensity, the higher the kinetic energy of the ionized electron.

Another feature which emerged with further investigation of the ATI [Pau+94] was the presence of a broad plateau in the photoelectron spectrum, which contradicted the common assumption that transition amplitudes scale as I_l^{-n} . At high laser field intensities, it was observed that the spectral plateau extended from about twice the ponderomotive energy $2 U_p$, up to $10 U_p$. The ponderomotive energy is defined as the average kinetic energy of an electron in quiver motion in an oscillating electric field, and is given by

$$U_p = \frac{e^2}{4m_e} \frac{E_0^2}{\omega^2}, \quad (2.1)$$

where ω is the laser frequency and $I = \epsilon_0 c E_0^2$ the laser intensity.

Closely related to the ATI process was the observation [Fer+88] of high harmonic radiation emitted by noble gas atoms irradiated by a strong field. The non-linearity of the

electron dynamics causes the conversion of the NIR laser field into XUV radiation, whose spectrum consists in odd harmonics of the laser frequency, with an extended plateau of high order harmonics up to a cutoff energy $E_c = I_p + 3.2U_p$, where I_p is the atomic ionization potential. Before recognizing the common process responsible for both the ATI and HHG, numerical solutions of the time dependent Schrödinger equation were able to qualitatively reproduce the spectral features of HHG, confirming that non-relativistic quantum mechanics was the right framework to describe the physics of strong field ionization, but not in the perturbation regime.

2.1 Three step model

The theory capable of explaining the essence of the physical processes described in the previous sections is the so-called three step model, conceived independently in [Cor93; KSK93] in 1993. Most interestingly, it is a completely classical model, which consists in separating the electron dynamics in three steps: the ionization phase, quiver phase and the recollision phase.

The first step occurs in the tunneling ionization regime. According to Keldysh theory [Kel65], this occurs for values of $\gamma_K \ll 1$, where the Keldysh parameter is defined as

$$\gamma_K = \sqrt{\frac{I_p}{2U_p}} = \frac{\omega\sqrt{2m_e I_p}}{eE_0}. \quad (2.2)$$

In the length gauge, within the dipole approximation, the Hamiltonian of the system is given by

$$H = \frac{p^2}{2} - V(r) + \mathbf{E}(t) \cdot \mathbf{r}. \quad (2.3)$$

For intensities above 10^{14} W/cm², the electric field is strong enough to bend the Coulomb potential, as illustrated in Figure 2.1, such that tunneling ionization becomes possible.

Once ionized, the electron is accelerated away and then pulled back to the nucleus, with which it recollides after every half laser period. The condition for recollision is that the electron falls back on the ion. This requirement explains why the plateau regions observed in the experiments are found only for linear polarizations of the driving laser, while suppressed for circularly polarized pulses. The recollision condition can be written as (in atomic units $e = \hbar = m_e = 1$):

$$x(t_1) - x(t_0) = \int_{t_0}^{t_1} v(t)dt = \int_{t_0}^{t_1} \int_{t_0}^t E(t')dt'dt \stackrel{!}{=} 0, \quad (2.4)$$

where t_0 is the time of ionization, and t_1 is the recollision instant. For a cw laser field one

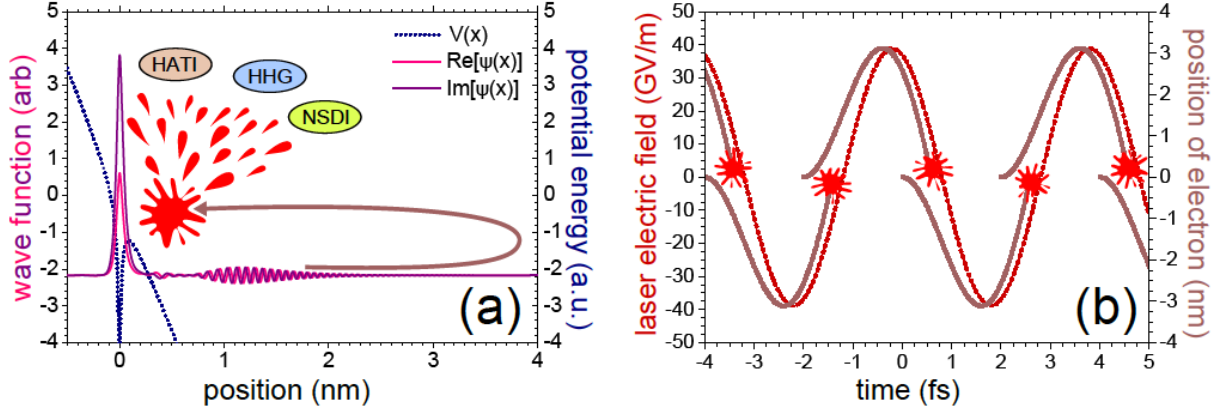


Figure 2.1: Illustration of the three step model. The bending of the Coulomb potential (blue dotted line) by a strong laser field allows an electron to tunnel out of the potential barrier. The electron is then accelerated in the laser field, driven back and rescattered with the ion. The trajectories of the tunneling electrons launched in the laser field are shown in the left panel. The electrons are accelerated away and driven back to the ion after every half cycle of the laser field. Figure reproduced from [Gag11].

has $E(t) = E_0 \cos(\omega t)$, thus $v(t) = \frac{E_0}{\omega} (\sin(\omega t) - \sin(\omega t_0))$. Therefore Eq. (2.4) becomes:

$$0 = \frac{E_0}{\omega^2} (\cos(\omega t) - \cos(\omega t_0)) + \frac{E_0}{\omega} \sin(\omega t_0) (t_1 - t_0), \quad (2.5)$$

which is a transcendental equation and must be solved numerically.

Depending on the outcome of the recollision one can have different scenarios. Let us consider the momentum acquired by the electron in the laser field from t_0 to t_1 , and from t_1 till the end of the pulse:

$$p(t_1, t_0) = - \int_{t_0}^{t_1} E(t) dt = A(t_1) - A(t_0),$$

$$p(\infty, t_1) = - \int_{t_1}^{\infty} E(t) dt = -A(t_0),$$

where the vector potential A in the Coulomb gauge is $E = -\frac{\partial A}{\partial t}$.

In the case of elastic scattering the electron momentum can reverse sign at t_1 , thus the final momentum is given by

$$p_f = p(\infty, t_1) - p(t_1, t_0) = -2A(t_1) + A(t_0). \quad (2.6)$$

Hence the maximum momentum acquired by the electron is

$$p_{max} = \max_{t_0} | -2A(t_1) + A(t_0) | \quad (2.7)$$

with t_1 determined by the constraint of Eq. (2.4). Considering that the ponderomotive energy in term of the vector potential is $U_p = A_0^2/4$, one can infer that the unconstrained maximum kinetic energy is $\frac{p_{max}^2}{2} = (3A_0)^2/2 = 18U_p$. Solving Eq. (2.7) numerically one finds a lower value:

$$\frac{p_{max}^2}{2} = 10U_p, \quad (2.8)$$

which is in very good agreement with the observed position of the ATI spectrum cutoff.

Another possibility is that the electron recollides inelastically with the ion. In this case the final momentum is given by $p(\infty, t_1) + p(t_1, t_0) = -A(t_0)$. Thus the maximum photon energy radiated as a product of inelastic scattering (neglecting other effects like inverse Bremsstrahlung) is the sum of the ionization potential and the square of the vector potential, or in term of the ponderomotive energy: $E_{max} = I_p + 4U_p$. Taking into account the recollision constraint one obtains:

$$E_{max} = I_p + 3.17U_p. \quad (2.9)$$

Thus, also the cutoff energy of the HHG spectrum is accurately predicted.

The three step model also explains the odd periodicity of the harmonics in HHG. Indeed, for each laser cycle, two identical recollision events occur, after every half cycle in which the laser field changes sign. If the recollision events are identical, the rescattering periodicity is half the laser cycle $\delta t = T_l/2$, corresponding to a spectral spacing of $\delta\omega = 2\omega_l$, which summed to the fundamental laser frequency gives its odd harmonics.

2.2 Attosecond pulse generation

It was soon recognized the possibility to generate sub-femtosecond XUV pulse trains from HHG, provided that the relative harmonic phases are coherent. In order to prove such coherence, a characterization technique called RABITT (Reconstruction of Attosecond Beating by Interference of Two-photon Transitions) [Mul02] was developed, which allows to determine the relative phases between subsequent harmonics. The technique consists in letting the attosecond pulse train ionize a second target, together with a highly attenuated NIR pulse (typically the same driver NIR pulse). The role of the NIR pulse is to “dress” the single-photon ionization from the $2m + 1$ -th harmonic in the pulse train with an additional fundamental frequency ω_L , which results in either the absorption or the emission of an $\hbar\omega_L$ photon. Thus, an even harmonic of order $2m$ in the spectrogram can be due to either the absorption of the order $2m + 1$ followed by emission of an $\hbar\omega_L$ quantum, or by absorption of the order $2m - 1$ plus a further quantum. In the absence of any process distinguishing

the two channel relative to each even harmonic order, the resulting channel interference determines the intensity of the $2m$ -th harmonic. By recording the oscillations of the even photoelectron peaks as a function of the XUV-NIR time delay as shown in Figure 2.2, it is possible to extract the relative phase between the neighbor odd harmonics.

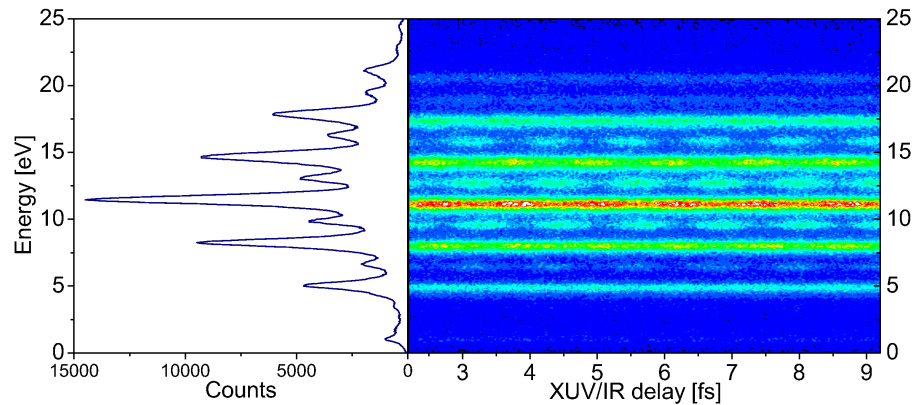


Figure 2.2: In the RABITT measurement a set of discrete peaks between the odd harmonics appears, when the dressing laser field overlaps with the attosecond pulse train. The even peaks result from the interference between two bi-photon processes, which can be destructive or constructive depending on the delay between the XUV and NIR fields. On the left the delay integrated signal is shown, for a comparison of the relative magnitude of even and odd harmonics. Figure reproduced from [Mos14].

However, in order to correctly interpret the spectroscopic data obtained in a pump-probe experiment spanning over more than a laser period, isolated attosecond pulses are required. For the production of an isolated attosecond pulse, the recollision process and the consequent generation of high harmonics has to be limited to a single half-cycle of the driving field.

The generation of an isolated attosecond pulse was first experimentally demonstrated in 2001 by the group of F. Krausz [Hen+01]. The generation mechanism consists in using such a short femtosecond pulse (7 fs FWHM in [Hen+01]), that only one NIR peak contributes to the emission of radiation in the range of interest. In this context, the key experimental factors which allowed the breakthrough were the precise control of the carrier-envelope offset (CEO) phase [Bal+03], i.e. the offset between the optical phase and the maximum of the pulse envelope, and the development of multi-layer mirrors for the filtering of the high HHG spectral component [Szi+94]. The importance of the CEO phase [TGB99] for few cycle pulses is illustrated in Figure 2.3. For a long laser pulse, a shift of the phase with respect to the envelop is irrelevant in term of HHG. But for the generation of single attosecond pulses it is fundamental to limit the harmonic radiation bursts to a single half-cycle. For

the extremal case of $\phi_{\text{ceo}} = 90^\circ$ the obtained HH spectrum corresponds to two attosecond pulses.

2.3 Attosecond Streak Camera

Also the diagnostic tools have to be fixed in order to characterize a single attosecond pulse. While in an attosecond pulse train (APT) the harmonic spectral peaks are well determined, and is therefore possible to use the RABITT technique, in the case of an isolated attosecond pulse (IAP) the spectrum in the cutoff region looks more like a continuum than a series of odd harmonic peaks, and using a weak NIR pulse to mix the odd frequencies would not produce any measurable effect. If indeed one would try to perform RABITT on a single attosecond pulse, the spectrum would remain unaltered for each time delay between the IAP and the weak NIR pulse, making any information retrieval impossible. The solution is to strongly increase the intensity of the NIR laser pulse, so that the whole photoelectron (PE) spectrum starts being shifted and distorted according to the time delay. The result is that the PEs are streaked by the strong NIR field, and it is possible to reconstruct the temporal properties of the pulse by analyzing the final momentum distribution of the PE. This pump-probe experiment is called “attosecond streak camera” (in analogy with the voltage driven picosecond streak camera [BLS71]) and can be thought as an arrangement which maps photoemission time to final PE momentum. From the obtained *spectrogram* (see Figure 2.4a), various informations about the NIR pulse and the attosecond pulse can be extracted. In experiments, photoionization events follow a probability given by the attosecond pulse intensity envelop. The initial kinetic energy of the PE is given by the instantaneous frequency of the pulse, rather than the carrier frequency. This determines the breadth of the streaking trace in both the time delay and the final momentum, respectively. As it is evident from Figure 2.4a, the trace follows the time evolution of the NIR field. In fact, each PE collected by the detector has a final momentum of

$$p_f = p_i(t) - eA(t - \tau), \quad (2.10)$$

where t is the ionization time and τ is the NIR-XUV delay. Thus, the centroids of the photoelectron spectra as a function of the delay τ trace the temporal evolution of the NIR vector potential. Attosecond streaking provides a tool for the complete characterization of the streaking electric field, giving information not only about its intensity, but also about its CEO phase. The theory underlying the streaking field reconstruction will be discussed in section 5.2.

Furthermore, the breadth of the streaking trace, both in the energy and in the delay domain, allows to determine the pulse duration of the attosecond pulse, and a set of other additional informations like its chirp. Since this topic does not concern this thesis, its discussion is omitted. The curious reader can find a comprehensive treatment of the subject in [Cha11].

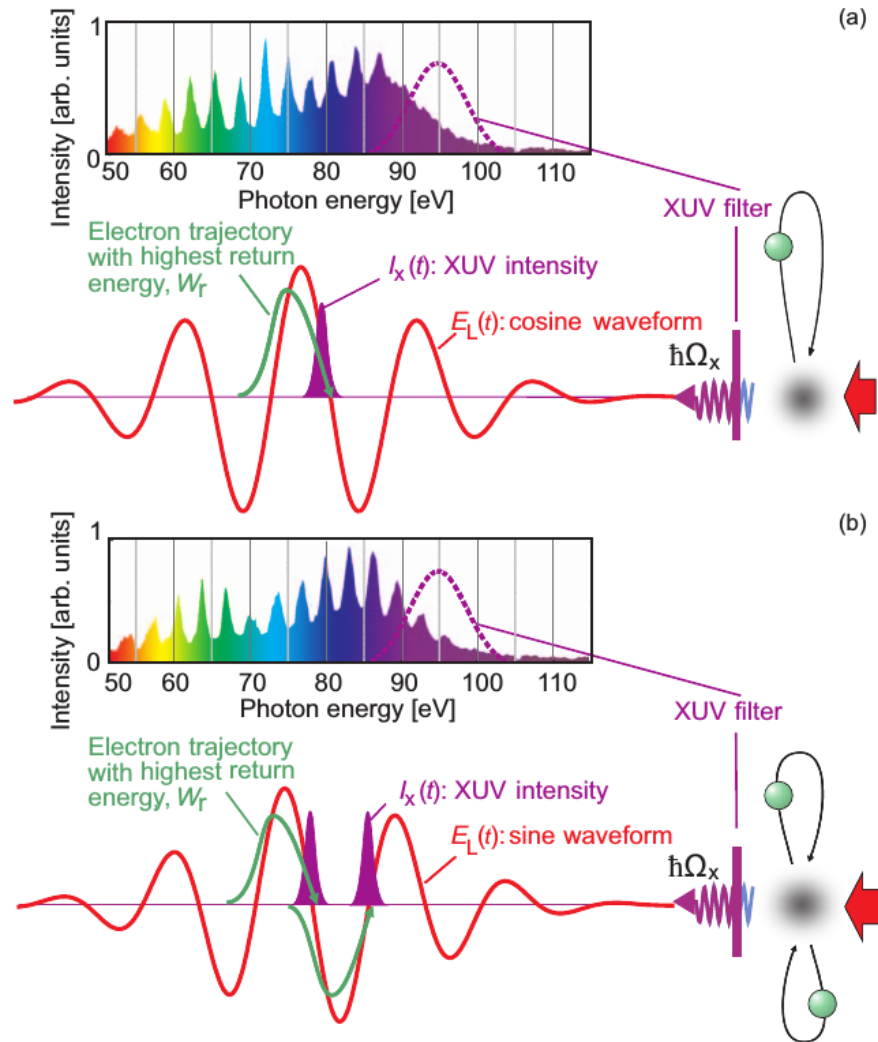


Figure 2.3: The influence of the CEO phase on the generation of isolated attosecond pulses is shown. The highest energy XUV photons, which determine the cutoff region of the HH spectrum, are created from electrons launched at the peak of the electric field and recolliding with the nucleus at the zero-crossings. For a CEO phase of 0, corresponding to a cosine wave, the most energetic electron trajectory is launched only at one field maximum, generating a continuous of radiation in the cutoff region, which results in an isolated attosecond pulse after appropriate spectral filtering. On the other hand, for a CEO phase of 90 degrees, the highest energetic trajectories are launched for two opposite values of the electric field, generating a pair of attosecond pulses. In general, the best CEO phase optimizing the attosecond pulse duration and intensity is somewhat bigger than 0, since this allows to increase the electron trajectory probability. Figure reproduced from [KI09].

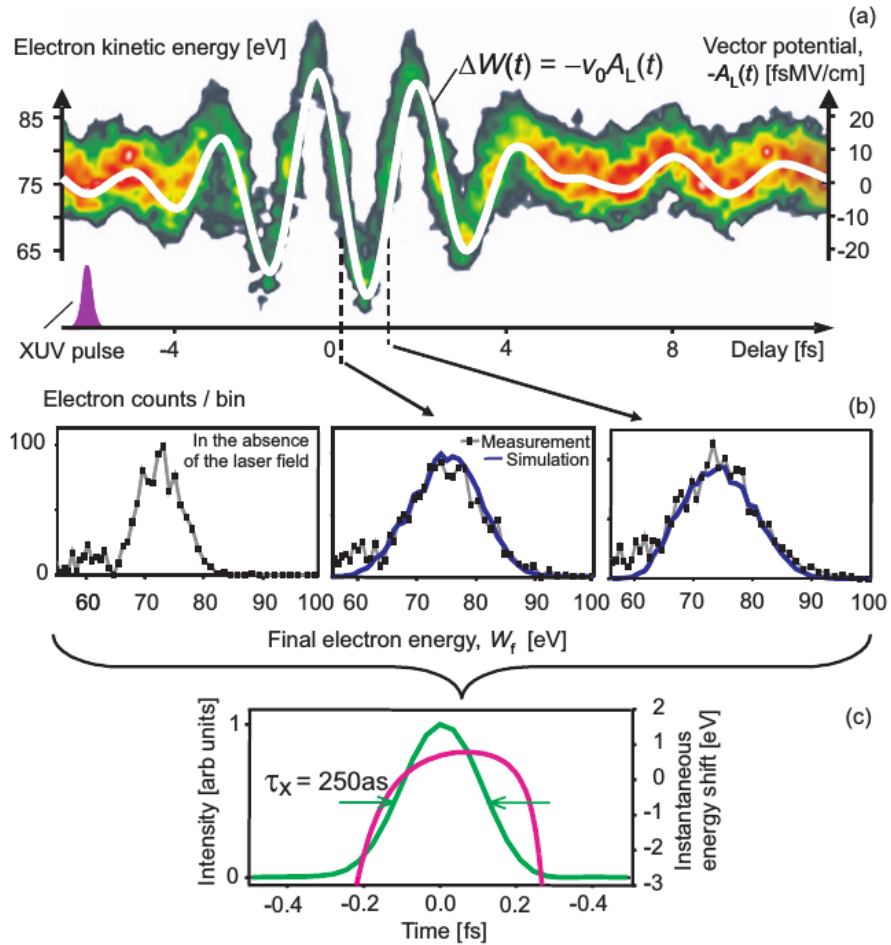


Figure 2.4: The attosecond streaking measurement maps the momentum distribution at the photoemission time due to an isolated attosecond pulse, to a final momentum distribution. The obtained streaking spectrogram (a), composed of a sequence of streaked photoelectron spectra for different NIR-XUV time delays, allows a complete reconstruction of the streaking field (a), and the measurement of the temporal properties of the XUV attosecond pulse (b, c), as its time duration and chirp. Figure reproduced from [KI09].

3

Surface Plasmon Polaritons

This chapter presents an introduction to the field of plasmonics. Plasmonics is the field of study of electron collective oscillations at metal surfaces, which can be either localized or propagating along an interface between two media. For the purposes of this thesis, the main focus will be only on the latter case. Propagating surface plasmons are called Surface Plasmons Polaritons (SPPs). The word “polariton” refers to the coupled nature of the polarization wave of the electron density with the driving field. In general, many kinds of polaritons exist: a field propagating through a crystal can produce mechanical oscillation of the lattice sites, generating a phonon polariton; if the coupling involves electron-hole pairs, for example in a semiconductor, it is called an exciton polariton. Here the focus is on the plasmon polariton, a longitudinal electromagnetic field coupled to mechanical oscillations of the charge density.

The electromagnetic field associated to an SPP is described by a wave propagating along the interface between two media, whose amplitude decays exponentially with the distance from the surface. Close to it, the plasmonic field amplitude can exceed that of the driving field. This means not only that plasmonic excitations own enhancement properties, but also, since the energy must be conserved, confinement properties. In fact, enhancement and confinement are the two key factors that explain the great interest for the field of Plasmonics. The enhancement properties are used in applications involving non-linear effects or, combined to the sensitivity to external source conditions, for developing bio-molecular sensors, while the confinement of the optical field is exploited to squeeze the electromagnetic field beyond the $\lambda/2$ diffraction limit.

From a microscopical point of view, it will be shown in section 3.2 that a plasmon polariton is a particular pole of the susceptibility $\chi(\mathbf{k}, \omega)$ of an interacting electron gas, corresponding to a state composed of the coherent superposition of all the possible electron transitions with the same momentum transfer \mathbf{k} . This microscopic property allows to identify plasmons not only in solid state systems, but also in small clusters and even in molecules [Kra+14]. SPPs are often viewed as resonances, because at the macroscopic level their excitation is typically associated with a peak (dip) in the transmission (reflection) spectrum of the supporting material. Moreover, for the excitation to occur, the

driving source must satisfy a phase matching condition with the SPP wavevector, typically involving frequency and angle of incidence [Mai07].

The plasmonic response of a system to an external perturbation develops on a timescale set by the plasma frequency of the material. Table 3.1 lists the plasmon frequencies of some typical plasmonic materials. For plasma frequencies of the order of 10 eV, a rough estimate

Table 3.1: Plasmon frequencies of typical plasmonic materials. The plasmon frequency sets the timescale of the electric response to an external stimulation. For the metals reported, the electron response occurs on a subfemtosecond timescale. The plasmon frequencies are given in eV.

Metal	Au	Ag	Al	Pt	W	Ni	Cu
ω_{pl}	9.03	9.01	14.98	9.59	13.22	15.92	10.83

based on $\Delta E \Delta t \sim h$ indicates that the electronic response to an external source occurs on a timescale shorter than 1 fs. If instead of metals we consider semiconductor materials, the presence of an energy gap between valence and conduction bands is such that the density of the electron-hole pairs contributing to the plasma oscillations is much smaller than in a metal. Since the plasma frequency depends on the carrier density as $\omega_{\text{pl}} \propto \sqrt{n_c}$, semiconductor plasma frequencies are typically of the order of few meVs, i.e. of the same order of magnitude of the room temperature phonon energy. Thus, with a simple estimate of the plasma frequency, it is possible to predict that while in semiconductors the electron-phonon coupling plays a fundamental role in the electric response, in metals the electron dynamic timescale is well separated from the lattice one.

3.1 Classical theory of SPPs

The electromagnetic field of an SPP propagating along a surface $y = 0$ can be expressed as in Eq. 3.1, where the magnetic field is assumed parallel to the surface: $\mathbf{B} = B(x, y)\mathbf{z}$.

$$B(x, y) = A e^{i(k_{\text{sp}}x - \omega t)} \left[e^{-\kappa_m y} \vartheta(y) + e^{\kappa_d y} \vartheta(-y) \right]. \quad (3.1)$$

Here $\vartheta(y)$ is the Heaviside function, κ_m, κ_d are the decay lengths respectively in the material below and above the surface, and $\text{Im}\{\kappa_i\} = 0$ is assumed for both $i = m, d$. The field must be a solution of Maxwell's equations, thus it is sufficient that it satisfies the wave equation in both media:

$$-\nabla^2 \mathbf{B} - \varepsilon_i \frac{\omega^2}{c^2} \mathbf{B} = 0, \quad \text{with } i = m, d. \quad (3.2)$$

Substitution of expression 3.1 in the above equation gives

$$-k_{\text{spp}}^2 + \kappa_i^2 + \varepsilon_i \frac{\omega^2}{c^2} = 0 \quad \Longrightarrow \quad \begin{cases} \kappa_d = \sqrt{k_{\text{spp}}^2 - \varepsilon_d \frac{\omega^2}{c^2}} & \text{for } y > 0 \\ \kappa_m = \sqrt{k_{\text{spp}}^2 - \varepsilon_m \frac{\omega^2}{c^2}} & \text{for } y < 0 \end{cases} \quad (3.3)$$

The continuity of the electric field parallel to the surface is ensured by imposing the continuity of $\partial_y B(x, y)$ across the surface. This leads to:

$$-\frac{\kappa_m}{\varepsilon_m} = \frac{\kappa_d}{\varepsilon_d}. \quad (3.4)$$

Since both the κ 's are positive, Eq. (3.4) is solvable only if the dielectric constants have opposite signs, i.e. $\varepsilon_m \varepsilon_d < 0$. This is the reason why plasmonic excitations typically occur at interfaces between a metal and a dielectric medium, since for metal dielectric functions $\text{Re}\{\varepsilon_m\} < 0$. The solution of Eq. (3.4) determines the plasmon wavevector

$$k_{\text{spp}}^2 = \frac{\omega^2}{c^2} \frac{\varepsilon_d \varepsilon_m}{\varepsilon_d + \varepsilon_m}. \quad (3.5)$$

In order to obtain a solution of Eq. (3.5) representing a propagating mode, the additional condition $\text{Re}\{\varepsilon_d + \varepsilon_m\} < 0$ must be verified, which is typically satisfied by metals at optical or NIR wavelengths. The plasmon wavevector is complex if losses in the metal are taken into account. By setting $\varepsilon_d = 1$ and $\varepsilon_m = \varepsilon' + i\varepsilon''$ one has, in the limit $\varepsilon'' \ll \varepsilon'$:

$$k_{\text{spp}} \simeq \frac{\omega}{c} \sqrt{\frac{\varepsilon'}{1 + \varepsilon'}} \left(1 + \frac{i}{2} \frac{\varepsilon''}{\varepsilon'(1 + \varepsilon')} \right) \quad (3.6)$$

$$\kappa_d \simeq \frac{\omega}{c} \sqrt{-\frac{1}{1 + \varepsilon'}} \left(1 - \frac{i}{2} \frac{\varepsilon''}{1 + \varepsilon'} \right) \quad (3.7)$$

$$\kappa_m \simeq \frac{\omega}{c} \sqrt{-\frac{|\varepsilon|^2}{1 + \varepsilon'}} \left(1 + \frac{i}{2} \varepsilon'' \frac{|\varepsilon|^2 + 2\varepsilon'}{|\varepsilon|^2(1 + \varepsilon')} \right) \quad (3.8)$$

The real part of the dispersion relation $\omega = \omega(k_{\text{spp}})$ is illustrated in Figure 3.1 for a plasmon propagating at the interface between air and a perfect Drude metal, whose dielectric function is $\varepsilon_m(\omega) = 1 - \frac{\omega_{\text{pl}}^2}{\omega^2}$. The dispersion relation shows a horizontal asymptote for very large wavevectors, where the frequency tends to the limit value of $\omega_{\text{spp}} \equiv \omega_{\text{pl}}/\sqrt{1 + \varepsilon_d}$. Also, two regimes are clearly discernible, a first one for $ck_{\text{spp}} \ll \omega_{\text{spp}}$ called *electromagnetic* or *retarded* one, where the dispersion relation is close to the light cone, and the second one for $ck_{\text{spp}} \gg \omega_{\text{spp}}$ called *electrostatic* or *non-retarded*, where the dispersion relation is flat and the plasmon frequency does not depend on the wavevector anymore.

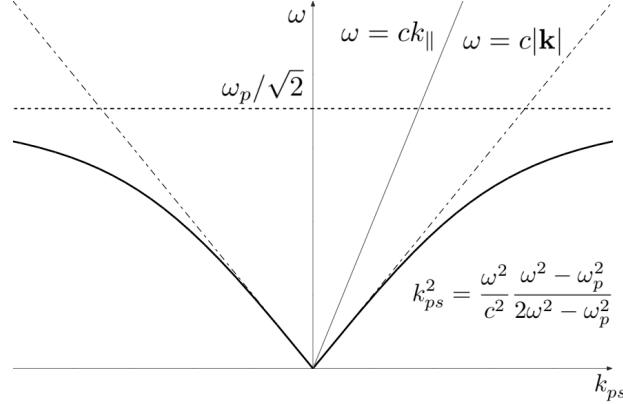


Figure 3.1: Dispersion relation of an SPP on a flat metal surface described by the free electron gas model $\epsilon(\omega) = 1 - \omega_{pl}^2/\omega^2$. The SPP curve lies outside the light cone, hence no matching with a plane wave can occur.

The imaginary part of the plasmon wavevector accounts for its propagation distance $\delta_{\text{spp}} = 1/\text{Im}\{k_{\text{spp}}\}$ along the surface, and strongly depends, through the imaginary part of the dielectric constant, on the excitation frequency ω . On gold excited at 633 nm it amounts to $\sim 10 \mu\text{m}$, while for a wavelength of 1 μm the propagation length is of 92 μm . In a similar way, the quantities $\delta_i = 1/\text{Im}\{\kappa_i\}$ describe the decay of the plasmonic field in the dielectric and its penetration in the metal. In Figure 3.2 are reported the decay length for aluminum and silver.

3.1.1 SPPs as poles of the complex reflection coefficient

Another way to derive the physical properties of SPPs is to look at the Fresnel's reflection and transmission coefficients. Assuming like before a TM polarized plane wave of wavelength k_0 impinging on a flat mirror at incidence angle θ , the Fresnel reflection and transmission coefficients are given by [BW99]:

$$r(\alpha) = \frac{n^2\beta - \gamma}{n^2\beta + \gamma}, \quad t = \frac{2n^2\beta}{n^2\beta + \gamma}, \quad (3.9)$$

where $\alpha = k_{\parallel} = k_0 \sin \theta$ and $\beta = k_{\perp} = \sqrt{k_0^2 - \alpha^2}$ are the wavevector components in the vacuum side, while $\gamma = \sqrt{n^2 k_0^2 - \alpha^2}$ is the component inside the material perpendicular to the interface. Assuming for simplicity that $n^2 = \epsilon$ is real, $n^2 < 0$ and γ becomes purely imaginary. Thus, by analytically continuing the Fresnel coefficients to the complex plane, poles appear in the denominator of Eq. (3.9), which correspond to SPP resonances.

The condition $n^2\beta + \gamma = 0$ is fulfilled by $\alpha_{\text{spp}} = k_0 n / \sqrt{1 + n^2}$, whence the dispersion

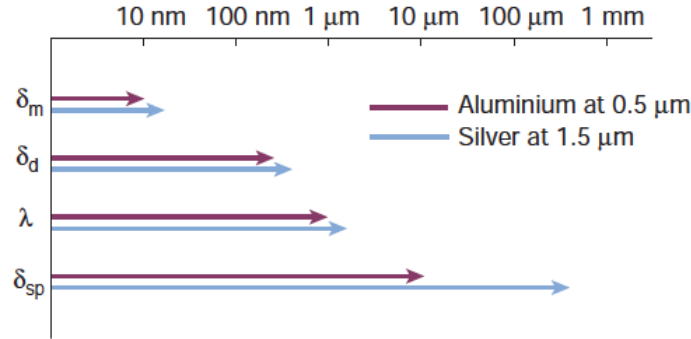


Figure 3.2: The propagation length and penetration depth of an SPP are shown for aluminium and for silver. The propagation length on a flat surface δ_{spp} is given by the losses in the metal. In Al at 500 nm wavelength, strong intrinsic absorption limits the propagation length to 2 μm . On the contrary, Ag at 1,5 μm shows a propagation length up to 1 mm. The penetration depth in the metal is typically of the order of 10-20 nm at optical frequencies. The decay length in the dielectric material is instead of the order of half the wavelength. Figure reproduced from [BDE03].

relation of the mode is obtained:

$$k_{\parallel} = \frac{\omega}{c} \sqrt{\frac{\epsilon(\omega)}{1 + \epsilon(\omega)}} \equiv k_{spp}(\omega). \quad (3.10)$$

Eq. (3.10) also provides the *matching condition* which needs to be satisfied by the driving source. In fact, the right hand side is the plasmonic wavevector supported by the material at the frequency ω of the source. This has to be equal to the source wavevector component parallel to the surface.

Since $\alpha_{spp}/k_0 > 1$, the corresponding β_{spp} and γ_{spp} are purely imaginary, giving rise to a field which is evanescent away from the surface. Because of this, it exists a field gradient perpendicular to the surface $\nabla_{\perp} E_{\perp} \neq 0$, such that the electric field lines close around the surface. In Figure 3.3 an illustration of the SPP field lines is reported.

A crucial point is that, since $k_{spp} > k_0$, an SPP can never be excited by a plane wave incident on a flat surface. This is true for every material displaying plasmonic properties and is well illustrated in Figure 3.1: since the dispersion curve always lies out of the light cone, the coupling with a plane wave can never occur. Thus, the fundamental problem in SPP generation is to satisfy the condition $k_{spp} > k_{\parallel}$.

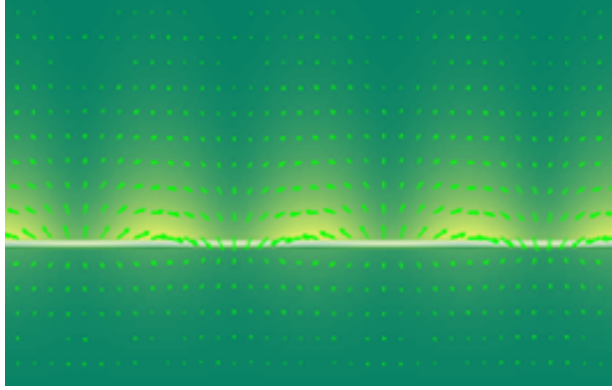


Figure 3.3: Schematic representation of the SPP field lines. The white line shows the surface position. The arrows indicate the field line strength and direction, the false-color map illustrates the field intensity distribution.

3.2 Quantum theory of SPPs

Before discussing the various SPP excitation strategies presented in paragraph 3.3, a quantum description of SPPs is provided, with the aim to illustrate how its fundamental collective character manifests at the macroscopic level.

A plasmon is a collective oscillation of the electron charge density driven by an external source, and can be described in term of the system polarization:

$$\mathbf{P}_{\text{ind}}(\mathbf{r}, t) = (\chi * \mathbf{E}_{\text{ext}})(\mathbf{r}, t) = \int d\mathbf{r}' \int dt' \chi(\mathbf{r}, \mathbf{r}', t, t') \mathbf{E}_{\text{ext}}(\mathbf{r}', t'), \quad (3.11)$$

where χ is the susceptibility of the considered system. On a quantum mechanical level, the charge density induced by an external potential is given by [FW03]:

$$\hat{\rho}_{\text{ind}}(\mathbf{r}, t) = \int d\mathbf{r}' \int dt' \hat{\chi}(\mathbf{r}, \mathbf{r}', t, t') \hat{\phi}_{\text{ext}}(\mathbf{r}', t'), \quad (3.12)$$

where ϕ_{ext} is an external potential. Assuming the potential to be a small perturbation with respect to the ground state Hamiltonian, the system does not depend on absolute times, but rather only on the difference $t - t'$, since the equilibrium steady-state system is not modified in response to the external field. This framework is typically called linear response theory. In the case of a non-interacting electron gas, $\chi \equiv \chi_0$ contains the information about the response of the system to an external field, and thus about its possible excitations, in the linear response limit.

The susceptibility of a non interacting electron gas is defined as (cf. [FW03], Chap. IX):

$$\hat{\chi}_0(\mathbf{r}, t; \mathbf{r}', t') = -i\Theta(t - t') \langle [\hat{\rho}(\mathbf{r}, t), \hat{\rho}(\mathbf{r}', t')] \rangle, \quad (3.13)$$

where $\Theta(t - t')$ ensures the causality of the process. The electron density is defined as :

$$\hat{\rho}(\mathbf{r}) = -e\hat{n}(\mathbf{r}) = -e\hat{\psi}^\dagger(\mathbf{r})\hat{\psi}(\mathbf{r}), \quad (3.14)$$

where \hat{n} is the number density operator, $\hat{\psi}^\dagger$, $\hat{\psi}$ are the creation and annihilation operators of a fermion at the position \mathbf{r} , and the spin indexes were neglected. The operator symbols are from now on dropped.

If the system is homogeneous, i.e. $f(\mathbf{r}, \mathbf{r}') = f(\mathbf{r} - \mathbf{r}')$ for any physical observable f , Eq. (3.12) can be rewritten as

$$\rho_{\text{ind}}(\mathbf{k}, \omega) = \chi_0(\mathbf{q}, \omega)\phi_{\text{ext}}(\mathbf{q}, \omega). \quad (3.15)$$

To compute $\chi_0(\mathbf{q}, \omega)$ let us first calculate the spatial Fourier transform $\chi_0(\mathbf{q}, t, t')$ of Eq. (3.13). By using the definitions

$$\begin{aligned} \rho(\mathbf{r}, t) &= \frac{1}{\mathcal{V}} \sum_{\mathbf{q}_1} \rho(\mathbf{q}_1, t) e^{i\mathbf{q}_1 \cdot \mathbf{r}}, \\ \rho(\mathbf{r}', t') &= \frac{1}{\mathcal{V}} \sum_{\mathbf{q}_2} \rho(\mathbf{q}_2, t') e^{i\mathbf{q}_2 \cdot \mathbf{r}'}, \end{aligned} \quad (3.16)$$

one gets

$$\chi_0(\mathbf{q}, t - t') = -\frac{i\Theta(t - t')}{\mathcal{V}} \sum_{\mathbf{q}_2} \langle [\rho(\mathbf{q}_1, t), \rho(\mathbf{q}_2, t')] \rangle e^{i(\mathbf{q}_1 + \mathbf{q}_2) \cdot \mathbf{r}'}. \quad (3.17)$$

Since the result of Eq. (3.17) cannot depend on \mathbf{r}' , the condition $\mathbf{q}_2 = -\mathbf{q}$ must be verified, reducing Eq. (3.17) to

$$\chi_0(\mathbf{q}, t - t') = -\frac{i\Theta(t - t')}{\mathcal{V}} \langle [\rho(\mathbf{q}, t), \rho(-\mathbf{q}, t')] \rangle. \quad (3.18)$$

The fermion operators in the definition Eq. (3.14) are the sum of all the possible single particle states which can be excited at the position \mathbf{r} :

$$\psi^\dagger(\mathbf{r}) = \sum_{\mathbf{k}} a_{\mathbf{k}}^\dagger \phi_{\mathbf{k}}^*(\mathbf{r}), \quad \psi(\mathbf{r}) = \sum_{\mathbf{k}} a_{\mathbf{k}} \phi_{\mathbf{k}}(\mathbf{r}), \quad (3.19)$$

where $a_{\mathbf{k}}^\dagger$, $a_{\mathbf{k}}$ are the ladder operators relative to the state \mathbf{k} , and $\phi_{\mathbf{k}}(\mathbf{r})$ can be any single particle basis function (f.e. Wannier states, Bloch states, Kohn-Sham orbitals etc.). In the present case, an electron gas can be represented in a basis of plane waves. With such a choice, the density operator can be rewritten as

$$\rho(\mathbf{r}) = -e \sum_{\mathbf{k}\mathbf{k}'} a_{\mathbf{k}}^\dagger a_{\mathbf{k}'} e^{i\mathbf{k} \cdot \mathbf{r}} e^{-i\mathbf{k}' \cdot \mathbf{r}} \longrightarrow \rho(\mathbf{q}) = \mathcal{F}[\rho(\mathbf{r})](\mathbf{q}) = -e \sum_{\mathbf{k}} a_{\mathbf{k}}^\dagger a_{\mathbf{k}+\mathbf{q}}, \quad (3.20)$$

where \mathcal{F} is the Fourier transform operator. The charge density operator can be interpreted as the sum of all the possible electron transitions of a given momentum \mathbf{q} . In a homogeneous system at equilibrium, the expectation value of the charge density operator is non-null only for $\mathbf{q} = 0$. The time dependent version of Eq. (3.20) is given by the Heisenberg equation of motion $i\partial_t\rho = [\rho, H_0]$, with the noninteracting Hamiltonian $H_0 = \sum_{\mathbf{k}} \epsilon_{\mathbf{k}} a_{\mathbf{k}}^\dagger a_{\mathbf{k}}$. This results in ([HK09], Chap. VII)

$$\rho(\mathbf{q}, t) = \sum_{\mathbf{k}} a_{\mathbf{k}}^\dagger a_{\mathbf{k}+\mathbf{q}} e^{-i(\epsilon_{\mathbf{k}+\mathbf{q}} - \epsilon_{\mathbf{k}})t}. \quad (3.21)$$

As a remark, the fact that ρ satisfies the Heisenberg equation of motion for the non-interacting Hamiltonian H_0 is what defines χ_0 as the susceptibility of a non-interacting electron gas. Eq. (3.13) would otherwise be a general definition. Substitution of Eq. (3.21) into the commutator of Eq. (3.18) gives

$$\begin{aligned} \langle [\rho(\mathbf{q}, t), \rho(-\mathbf{q}, t')] \rangle &= \sum_{\mathbf{k}, \mathbf{k}'} \langle [a_{\mathbf{k}}^\dagger a_{\mathbf{k}+\mathbf{q}}, a_{\mathbf{k}'}^\dagger a_{\mathbf{k}'-\mathbf{q}}] \rangle e^{-i(\epsilon_{\mathbf{k}+\mathbf{q}} - \epsilon_{\mathbf{k}})t} e^{i(\epsilon_{\mathbf{k}'} - \epsilon_{\mathbf{k}'-\mathbf{q}})t'} \\ &= \sum_{\mathbf{k}} [f_{\mathbf{k}} - f_{\mathbf{k}+\mathbf{q}}] e^{-i(\epsilon_{\mathbf{k}+\mathbf{q}} - \epsilon_{\mathbf{k}})(t-t')}, \end{aligned} \quad (3.22)$$

where the property $[a_{\mathbf{1}}^\dagger a_{\mathbf{2}}, a_{\mathbf{3}}^\dagger a_{\mathbf{4}}] = \delta_{2,3} a_{\mathbf{1}}^\dagger a_{\mathbf{4}} - \delta_{1,4} a_{\mathbf{3}}^\dagger a_{\mathbf{2}}$ was used and the definition of occupation number $f_{\mathbf{q}} = \langle n_{\mathbf{q}} \rangle = \langle a_{\mathbf{q}}^\dagger a_{\mathbf{q}} \rangle$ was employed. The function f is the Fermi-Dirac distribution, which for zero temperature $T = 0$ is $f_{\mathbf{k}} = \Theta(\mathbf{k}_F - \mathbf{k})$.

Setting $t - t' = \tau$ and calculating the Fourier transform with respect to τ , one obtains the susceptibility of the non-interacting electron gas

$$\begin{aligned} \chi_0(\mathbf{q}, \omega) &= \lim_{\eta \rightarrow 0^+} \int_{-\infty}^{\infty} \chi(\mathbf{q}, \tau) e^{i(\omega + i\eta)\tau} d\tau \\ &= \lim_{\eta \rightarrow 0^+} \frac{1}{\mathcal{V}} \sum_{\mathbf{k}} \frac{[f_{\mathbf{k}+\mathbf{q}} - f_{\mathbf{k}}]}{[\omega - (\epsilon_{\mathbf{k}+\mathbf{q}} - \epsilon_{\mathbf{k}}) + i\eta]}, \end{aligned} \quad (3.23)$$

where η is a convergence factor setting the integration contour in the lower half of the complex plane. The result in Eq. (3.23) is the so-called Lindhard's function ([HK09], Chap. VI). Its imaginary part describes the excitation of electron-hole pairs, where with the term hole is meant a vacancy in the Fermi sea. Using the relation $\lim_{\eta \rightarrow 0} \frac{1}{\omega + i\eta} = \mathcal{P} \left(\frac{1}{\omega} \right) - i\pi\delta(\omega)$, the imaginary part of χ_0 is given by

$$\text{Im} \{ \chi_0(\mathbf{q}, \omega) \} = -\frac{\pi}{\mathcal{V}} \sum_{\mathbf{k}} [f_{\mathbf{k}} - f_{\mathbf{k}+\mathbf{q}}] \delta(\omega + \epsilon_{\mathbf{k}} - \epsilon_{\mathbf{k}+\mathbf{q}}). \quad (3.24)$$

Using $\text{Im} \{ \chi_0(-\mathbf{q}, -\omega) \} = -\text{Im} \{ \chi_0(\mathbf{q}, \omega) \}$, only the positive part of the spectrum needs to be considered. Eq. (3.24) is different from zero for $|\mathbf{k}| < k_F$ and $|\mathbf{k} + \mathbf{q}| > k_F$, which

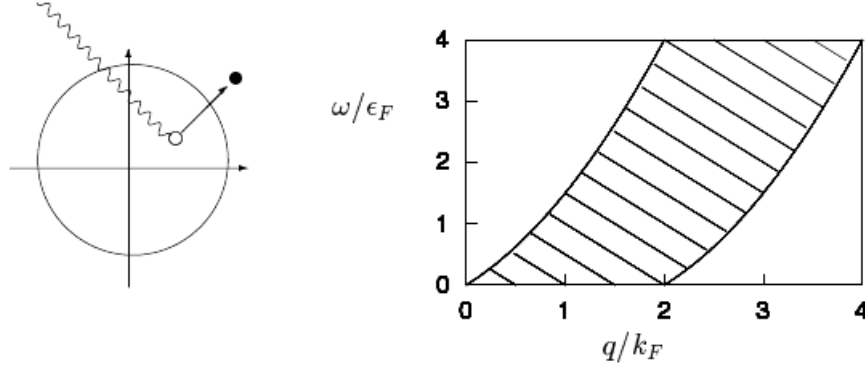


Figure 3.4: An electron can be excited to a higher energetic state if the transition occurs across the Fermi edge (left), leaving an unoccupied state, a hole, in the Fermi sea. The allowed transition corresponds to a region in the $(\omega - \mathbf{q})$ plane (right), where the condition $\text{Im}\{\chi_0(\mathbf{q}, \omega)\} \neq 0$ is met, which for this reason is called the electron-hole pair continuum.

results in two boundary curves in the $(\omega - \mathbf{q})$ plane

$$\omega = \epsilon_{\mathbf{k}+\mathbf{q}} - \epsilon_{\mathbf{k}} = \frac{q^2}{2m} + \frac{\mathbf{k} \cdot \mathbf{q}}{m} \implies \begin{cases} \omega_+ = \frac{q^2}{2m} + v_F q \\ \omega_- = \frac{q^2}{2m} - v_F q, \quad q > 2k_F \end{cases} \quad (3.25)$$

where the extremal values for $|\mathbf{k}| = \pm k_F$ were used. The two parabolas are shown in Figure 3.4 and delimit an area in the $(\omega - \mathbf{q})$ plane where particle-hole excitations are allowed, which for this reason is called electron-hole continuum. If ω and \mathbf{q} fall in the electron-hole continuum, the non-interacting electron system can be excited to states whose excitation frequencies are given by the poles of the Lindhard's function. By recasting Eq. (3.23) in the form

$$\chi_0(\mathbf{q}, \omega) = \sum_{\mathbf{k}} f_{\mathbf{k}} \left[\frac{1}{\epsilon_{\mathbf{k}} - \epsilon_{\mathbf{k}+\mathbf{q}} + \omega + i\eta} - \frac{1}{\epsilon_{\mathbf{k}} - \epsilon_{\mathbf{k}+\mathbf{q}} - \omega - i\eta} \right], \quad (3.26)$$

where the limit $\eta \rightarrow 0^+$ is given implicitly, and considering only the positive part of the frequency spectrum, one obtains a set of discrete poles at

$$\omega(\mathbf{q}) = \epsilon_{\mathbf{k}} - \epsilon_{\mathbf{k}+\mathbf{q}}, \quad (3.27)$$

for any given value of \mathbf{q} .

3.2.1 Random Phase Approximation (RPA)

Knowing the single particle excitations of the non-interacting system, one can proceed with the study of the collective excitations of the interacting electron gas. Using the plane waves basis, the Hamiltonian of the interacting electron gas in the Jellium model can be expressed in the form

$$H = \sum_{\mathbf{k}} \epsilon_{\mathbf{k}} a_{\mathbf{k}}^{\dagger} a_{\mathbf{k}} + \frac{1}{2} \sum_{\mathbf{k}, \mathbf{k}', \mathbf{q} \neq 0} V_{\mathbf{q}} a_{\mathbf{k}+\mathbf{q}}^{\dagger} a_{\mathbf{k}'-\mathbf{q}}^{\dagger} a_{\mathbf{k}} a_{\mathbf{k}'}, \quad (3.28)$$

with $V_{\mathbf{q}}$ the d -dimensional Fourier transform of the Coulomb potential $V(|\mathbf{r}-\mathbf{r}'|) = e^2/|\mathbf{r}-\mathbf{r}'|$. The exclusion of the term $\mathbf{q} = 0$ is due to the neutralizing action of the ion homogeneous background. The Coulomb potential can be rewritten as [HK90]

$$H_C = \frac{1}{2} \sum_{\mathbf{q}} V_{\mathbf{q}} (\rho_{\mathbf{q}} \rho_{-\mathbf{q}} - \hat{N}), \quad (3.29)$$

where the last term is the particle number operator and accounts for the ion background subtraction. Since any collective oscillation driven by an external field is, in the linear response theory, a perturbation of the equilibrium density, the electron density can be expanded as $\rho_{\mathbf{q}} = \langle \rho_{\mathbf{q}} \rangle + \delta \rho_{\mathbf{q}}$, where $\delta \rho_{\mathbf{q}} = \rho_{\mathbf{q}} - \langle \rho_{\mathbf{q}} \rangle$ is supposed to be a small perturbation. With this definitions one can write

$$\begin{aligned} \rho_{\mathbf{q}} \rho_{-\mathbf{q}} &= (\langle \rho_{\mathbf{q}} \rangle + \delta \rho_{\mathbf{q}}) (\langle \rho_{-\mathbf{q}} \rangle + \delta \rho_{-\mathbf{q}}) \\ &= \langle \rho_{\mathbf{q}} \rangle \langle \rho_{-\mathbf{q}} \rangle + \delta \rho_{\mathbf{q}} \langle \rho_{-\mathbf{q}} \rangle + \delta \rho_{-\mathbf{q}} \langle \rho_{\mathbf{q}} \rangle + \delta \rho_{\mathbf{q}} \delta \rho_{-\mathbf{q}} \\ \text{RPA} &\simeq \langle \rho_{\mathbf{q}} \rangle \langle \rho_{-\mathbf{q}} \rangle + \delta \rho_{\mathbf{q}} \langle \rho_{-\mathbf{q}} \rangle + \delta \rho_{-\mathbf{q}} \langle \rho_{\mathbf{q}} \rangle \\ &\simeq \langle \rho_{\mathbf{q}} \rangle \rho_{-\mathbf{q}} + \langle \rho_{-\mathbf{q}} \rangle \rho_{\mathbf{q}} - \langle \rho_{\mathbf{q}} \rangle \langle \rho_{-\mathbf{q}} \rangle. \end{aligned} \quad (3.30)$$

The random phase approximation consists in neglecting the correlations of the electron density oscillations, which is equivalent to assuming a random phase of the density fluctuations, such that they average to zero. In terms of ladder operators the last line in Eq. (3.30) can be written as:

$$a_1^{\dagger} a_2^{\dagger} a_3 a_4 \simeq \langle a_1^{\dagger} a_4 \rangle a_2^{\dagger} a_3 + a_1^{\dagger} a_4 \langle a_2^{\dagger} a_3 \rangle - \langle a_1^{\dagger} a_4 \rangle \langle a_2^{\dagger} a_3 \rangle. \quad (3.31)$$

The susceptibility of an interacting electron gas can be written as in Eq. (3.13)

$$\chi(\mathbf{q}, t-t') = -\frac{i\Theta(t-t')}{\mathcal{V}} \langle [\rho(\mathbf{q}, t), \rho(-\mathbf{q}, t')] \rangle. \quad (3.32)$$

It is useful to define the quantity $\chi(\mathbf{k}, \mathbf{q}, t - t')$, specified as

$$\chi(\mathbf{k}, \mathbf{q}, t - t') = -i\Theta(t - t') \langle [a_{\mathbf{k}}^\dagger a_{\mathbf{k}+\mathbf{q}}, \rho(-\mathbf{q}, t')] \rangle \Leftrightarrow \chi(\mathbf{q}, t - t') = \frac{1}{V} \sum_{\mathbf{k}} \chi(\mathbf{k}, \mathbf{q}, t - t'). \quad (3.33)$$

To derive an expression of the susceptibility in the RPA, one can compute the time derivative of $\chi(\mathbf{k}, \mathbf{q}, t - t')$:

$$i\partial_t \chi(\mathbf{k}, \mathbf{q}, t - t') = \delta(t - t') \langle [a_{\mathbf{k}}^\dagger a_{\mathbf{k}+\mathbf{q}}, \rho(-\mathbf{q}, t')] \rangle + i\Theta(t - t') \langle [[H, a_{\mathbf{k}}^\dagger a_{\mathbf{k}+\mathbf{q}}], \rho(-\mathbf{q}, t')] \rangle, \quad (3.34)$$

where the Heisenberg equation with the full interacting Hamiltonian H was used. The first term in Eq. (3.34) gives

$$[a_{\mathbf{k}}^\dagger a_{\mathbf{k}+\mathbf{q}}, \rho(-\mathbf{q}, t')] = \sum_{\mathbf{k}'} [a_{\mathbf{k}}^\dagger a_{\mathbf{k}+\mathbf{q}}, a_{\mathbf{k}'}^\dagger a_{\mathbf{k}'-\mathbf{q}}] = a_{\mathbf{k}}^\dagger a_{\mathbf{k}} - a_{\mathbf{k}+\mathbf{q}}^\dagger a_{\mathbf{k}+\mathbf{q}}. \quad (3.35)$$

To compute the inner commutator of Eq. (3.34) it is better to proceed separately with the two terms $H = H_0 + H_C$ (see [HK09], Chap. VII for details). The commutator with the kinetic energy term yields:

$$[H_0, a_{\mathbf{k}}^\dagger a_{\mathbf{k}+\mathbf{q}}] = (\epsilon_{\mathbf{k}} - \epsilon_{\mathbf{k}+\mathbf{q}}) a_{\mathbf{k}}^\dagger a_{\mathbf{k}+\mathbf{q}}. \quad (3.36)$$

The commutator with the Coulomb potential yields:

$$[H_C, a_{\mathbf{k}}^\dagger a_{\mathbf{k}+\mathbf{q}}] = \frac{1}{2} \sum_{\mathbf{q}', \mathbf{k}'} V_{\mathbf{q}'} [a_{\mathbf{k}+\mathbf{q}'}^\dagger a_{\mathbf{k}'-\mathbf{q}}^\dagger a_{\mathbf{k}'} a_{\mathbf{k}+\mathbf{q}} + a_{\mathbf{k}'+\mathbf{q}}^\dagger a_{\mathbf{k}'-\mathbf{q}}^\dagger a_{\mathbf{k}+\mathbf{q}} a_{\mathbf{k}'}] \quad (3.37)$$

$$- a_{\mathbf{k}'+\mathbf{q}}^\dagger a_{\mathbf{k}}^\dagger a_{\mathbf{k}+\mathbf{q}+\mathbf{q}'} a_{\mathbf{k}'} - a_{\mathbf{k}}^\dagger a_{\mathbf{k}'-\mathbf{q}}^\dagger a_{\mathbf{k}'} a_{\mathbf{k}+\mathbf{q}-\mathbf{q}'}]. \quad (3.38)$$

Eq. (3.37) shows that the dynamics of an observable which is function of one pair of creation and annihilation operators depends on a term which is in turn function of two pairs of ladder operators. Thus, in order to solve Eq. (3.34), the equation of motion for the 2 operator pair term should be derived, but it would turn out to depend on 3 operator pairs, and so on. The result of this procedure is a hierarchy of equations where the time derivative of an N-pair term depends on a (N+1)-pair term. Such a set of equations is called Bogoliubov–Born–Green–Kirkwood–Yvon (BBGKY) hierarchy, and is a result frequently encountered when dealing with the equations of motion of density matrices. The hierarchy can be truncated by means of the random phase approximation, such that Eq. (3.37) turns

into

$$\begin{aligned}
[H_C, a_{\mathbf{k}}^\dagger a_{\mathbf{k}+\mathbf{q}}] &\simeq \frac{1}{2} \sum_{\mathbf{q}' \neq 0, \mathbf{k}'} V_{\mathbf{q}'} \left[\langle a_{\mathbf{k}+\mathbf{q}'}^\dagger a_{\mathbf{k}+\mathbf{q}} \rangle a_{\mathbf{k}'-\mathbf{q}}^\dagger a_{\mathbf{k}'} + a_{\mathbf{k}+\mathbf{q}}^\dagger a_{\mathbf{k}+\mathbf{q}} \langle a_{\mathbf{k}'-\mathbf{q}}^\dagger a_{\mathbf{k}'} \rangle \right. \\
&\quad + \langle a_{\mathbf{k}'+\mathbf{q}'}^\dagger a_{\mathbf{k}'} \rangle a_{\mathbf{k}-\mathbf{q}}^\dagger a_{\mathbf{k}+\mathbf{q}} + a_{\mathbf{k}'+\mathbf{q}'}^\dagger a_{\mathbf{k}'} \langle a_{\mathbf{k}-\mathbf{q}}^\dagger a_{\mathbf{k}+\mathbf{q}} \rangle \\
&\quad - \langle a_{\mathbf{k}'+\mathbf{q}}^\dagger a_{\mathbf{k}'} \rangle a_{\mathbf{k}}^\dagger a_{\mathbf{k}+\mathbf{q}+\mathbf{q}'} - a_{\mathbf{k}'+\mathbf{q}}^\dagger a_{\mathbf{k}'} \langle a_{\mathbf{k}}^\dagger a_{\mathbf{k}+\mathbf{q}+\mathbf{q}'} \rangle \\
&\quad \left. - \langle a_{\mathbf{k}}^\dagger a_{\mathbf{k}+\mathbf{q}-\mathbf{q}'} \rangle a_{\mathbf{k}'-\mathbf{q}}^\dagger a_{\mathbf{k}'} - a_{\mathbf{k}}^\dagger a_{\mathbf{k}+\mathbf{q}-\mathbf{q}'} \langle a_{\mathbf{k}'-\mathbf{q}}^\dagger a_{\mathbf{k}'} \rangle \right] \quad (3.39)
\end{aligned}$$

and now depends only on single creation-annihilation pairs. Recalling that the average value of the density operator at equilibrium is non null only for zero momentum transfer $\langle a_{\mathbf{k}}^\dagger a_{\mathbf{k}'} \rangle = f_{\mathbf{k}} \delta_{\mathbf{k}, \mathbf{k}'}$ and considering that $\mathbf{q}' \neq 0$, only four of the eight terms in Eq. (3.39) are non zero. Thus

$$\begin{aligned}
[H_C, a_{\mathbf{k}}^\dagger a_{\mathbf{k}+\mathbf{q}}] &\simeq \frac{1}{2} \sum_{\mathbf{q}' \neq 0, \mathbf{k}'} V_{\mathbf{q}'} \left[f_{\mathbf{k}+\mathbf{q}} \delta_{\mathbf{q}', \mathbf{q}} a_{\mathbf{k}'-\mathbf{q}}^\dagger a_{\mathbf{k}'} + f_{\mathbf{k}+\mathbf{q}} \delta_{\mathbf{q}', -\mathbf{q}} a_{\mathbf{k}'+\mathbf{q}}^\dagger a_{\mathbf{k}'} \right. \\
&\quad \left. - f_{\mathbf{k}} \delta_{\mathbf{q}', -\mathbf{q}} a_{\mathbf{k}'+\mathbf{q}}^\dagger a_{\mathbf{k}'} - f_{\mathbf{k}} \delta_{\mathbf{q}', \mathbf{q}} a_{\mathbf{k}'-\mathbf{q}}^\dagger a_{\mathbf{k}'} \right] \\
&\simeq \frac{1}{2} (f_{\mathbf{k}+\mathbf{q}} - f_{\mathbf{k}}) \left[V_{\mathbf{q}} \sum_{\mathbf{k}'} a_{\mathbf{k}'-\mathbf{q}}^\dagger a_{\mathbf{k}'} + V_{-\mathbf{q}} \sum_{\mathbf{k}'} a_{\mathbf{k}'+\mathbf{q}}^\dagger a_{\mathbf{k}'} \right] \\
&\simeq \frac{1}{2\mathcal{V}} (f_{\mathbf{k}+\mathbf{q}} - f_{\mathbf{k}}) V_{\mathbf{q}} \rho(\mathbf{q}), \quad (3.40)
\end{aligned}$$

where in the last passage the properties $V_{\mathbf{q}} = V_{-\mathbf{q}}$ and $\rho(\mathbf{q}) = \rho(-\mathbf{q})$ were used. Plugging everything back into Eq. (3.33) one obtains

$$\begin{aligned}
i\partial_t \chi^{\text{RPA}}(\mathbf{k}, \mathbf{q}, t - t') &= \delta(t - t') (f_{\mathbf{k}} - f_{\mathbf{k}+\mathbf{q}}) \\
&\quad + (\epsilon_{\mathbf{k}} - \epsilon_{\mathbf{k}+\mathbf{q}}) \times \underbrace{i\Theta(t - t') \langle [a_{\mathbf{k}}^\dagger a_{\mathbf{k}+\mathbf{q}}(t), \rho(-\mathbf{q}, t')] \rangle}_{=\chi^{\text{RPA}}(\mathbf{k}, \mathbf{q}, t-t')} \\
&\quad - (f_{\mathbf{k}} - f_{\mathbf{k}+\mathbf{q}}) V(\mathbf{q}) \times \underbrace{\frac{i\Theta(t - t')}{\mathcal{V}} \langle [\rho(\mathbf{q}, t), \rho(-\mathbf{q}, t')] \rangle}_{=\chi^{\text{RPA}}(\mathbf{q}, t-t')}, \quad (3.41)
\end{aligned}$$

which reduces to

$$(i\partial_t + \epsilon_{\mathbf{k}} - \epsilon_{\mathbf{k}+\mathbf{q}}) \chi^{\text{RPA}}(\mathbf{k}, \mathbf{q}, t - t') = (f_{\mathbf{k}} - f_{\mathbf{k}+\mathbf{q}}) [\delta(t - t') + V_{\mathbf{q}} \chi^{\text{RPA}}(\mathbf{q}, t - t')]. \quad (3.42)$$

Fourier transforming Eq. (3.42) in time yields

$$\chi^{\text{RPA}}(\mathbf{k}, \mathbf{q}, \omega) = \frac{f_{\mathbf{k}} - f_{\mathbf{k}+\mathbf{q}}}{\omega + \epsilon_{\mathbf{k}} - \epsilon_{\mathbf{k}+\mathbf{q}} + i\eta} [1 + V_{\mathbf{q}} \chi^{\text{RPA}}(\mathbf{q}, \omega)] \quad (3.43)$$

$$\chi^{\text{RPA}}(\mathbf{q}, \omega) = \frac{1}{\mathcal{V}} \sum_{\mathbf{k}} \chi^{\text{RPA}}(\mathbf{k}, \mathbf{q}, \omega) = \frac{1}{\mathcal{V}} \underbrace{\sum_{\mathbf{k}} \frac{f_{\mathbf{k}} - f_{\mathbf{k}+\mathbf{q}}}{\omega + \epsilon_{\mathbf{k}} - \epsilon_{\mathbf{k}+\mathbf{q}} + i\eta}}_{=\chi_0(\mathbf{q}, \omega)} [1 + V_{\mathbf{q}} \chi^{\text{RPA}}(\mathbf{q}, \omega)]. \quad (3.44)$$

Recognizing the susceptibility of the non-interacting electron gas in Eq. (3.43) one obtains a Dyson's like equation for the susceptibility of the interacting electron gas in RPA:

$$\chi^{\text{RPA}}(\mathbf{q}, \omega) = \chi_0(\mathbf{q}, \omega) + \chi_0(\mathbf{q}, \omega) V_{\mathbf{q}} \chi^{\text{RPA}}(\mathbf{q}, \omega), \quad (3.45)$$

which has as solution

$$\chi^{\text{RPA}}(\mathbf{q}, \omega) = \frac{\chi_0(\mathbf{q}, \omega)}{1 - V_{\mathbf{q}} \chi_0(\mathbf{q}, \omega)}. \quad (3.46)$$

From Eq. (3.46) it is clear that the poles of χ^{RPA} are given not only by the poles of χ_0 , but also from the zeros of

$$1 - V_{\mathbf{q}} \chi_0(\mathbf{q}, \omega) = 0. \quad (3.47)$$

This means that on top of single particle excitations, which are the soles possible in a non-interacting gas, there are extra excitations arising from the Coulomb interaction. In Figure 3.5 the solutions of Eq. (3.47) are graphically shown. While the single particle excitation energies are slightly shifted by the interaction term, a new excitation frequency appears at higher energy, corresponding to a collective mode of the interacting electron gas, which is absent in the non-interacting case. The meaning of the term ‘‘collective’’ will be clarified in the next section. Before turning to that, it is interesting to analyze the eigenfrequency of the most energetic pole, in the limit of long wavelength. Let us consider again the imaginary part of the susceptibility:

$$\text{Im} \left\{ \chi^{\text{RPA}}(\mathbf{q}, \omega) \right\} = \frac{\text{Im} \{ \chi_0(\mathbf{q}, \omega) \}}{(1 - V_{\mathbf{q}} \text{Re} \{ \chi_0(\mathbf{q}, \omega) \})^2 + (V_{\mathbf{q}} \text{Im} \{ \chi_0(\mathbf{q}, \omega) \})^2}. \quad (3.48)$$

The term $\text{Im} \{ \chi_0(\mathbf{q}, \omega) \} \neq 0$ gives back the electron-hole continuum. In the case of $1 - V_{\mathbf{q}} \text{Re} \{ \chi_0(\mathbf{q}, \omega) \} = 0$, taking the real part of χ_0 by simply letting $\eta \rightarrow 0$ in Eq. (3.24), one

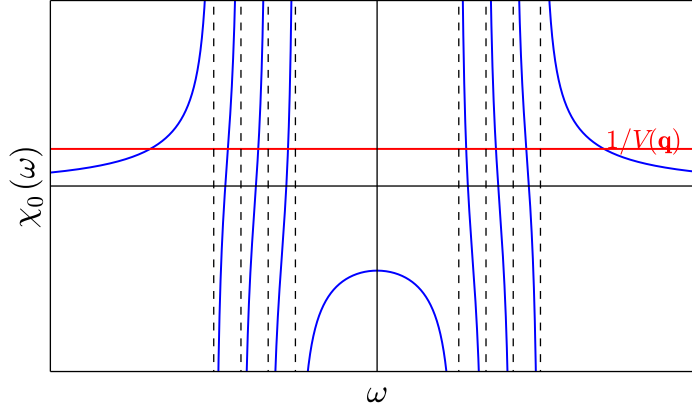


Figure 3.5: Plot of the Lindhard's function (blue thick line) as in Eq. (3.24) as a function of ω for a given value of \mathbf{q} , when only a set of four single particle excitations at energies $\{\epsilon_{\mathbf{a}}, \epsilon_{\mathbf{b}}, \epsilon_{\mathbf{c}}, \epsilon_{\mathbf{d}}\}$ are allowed (dashed vertical lines). The solutions of $\chi_0(\mathbf{q}, \omega) = 1/V_{\mathbf{q}}$ are the intersections with the horizontal line $1/V(\mathbf{q})$ (thick red line). The vertical dashed lines are the poles of the Lindhard's function, representing the only possible excitations in a non-interacting electron gas. For the interacting case, the single particle excitation energies are renormalized by the Coulomb interaction, but are qualitatively the same as in the non-interacting case. A new pole at higher energy appears, which represents the eigenfrequency of a collective oscillation mode of the interacting electron gas.

finds

$$\begin{aligned}
\frac{1}{V_{\mathbf{q}}} &= \frac{1}{\mathcal{V}} \sum_{\mathbf{k}} \frac{f_{\mathbf{k}+\mathbf{q}} - f_{\mathbf{k}}}{\omega - (\epsilon_{\mathbf{k}+\mathbf{q}} - \epsilon_{\mathbf{k}})} \simeq \frac{1}{\mathcal{V}} \sum_{\mathbf{k}} \frac{f_{\mathbf{k}} + \mathbf{q} \cdot \nabla_{\mathbf{k}} f_{\mathbf{k}} - f_{\mathbf{k}}}{\omega - \left(\frac{k^2}{2m} + \frac{\mathbf{k} \cdot \mathbf{q}}{m} - \frac{k^2}{2m}\right)} \\
&\simeq \frac{1}{\mathcal{V}\omega} \sum_{\mathbf{k}} \mathbf{q} \cdot \nabla_{\mathbf{k}} f_{\mathbf{k}} \left(1 + \frac{kq \cos \theta}{m\omega}\right) \simeq \frac{q^2}{m\omega^2 \mathcal{V}} \frac{2}{(2\pi)^2} \int_0^\infty dk k^2 k \frac{\partial f(k)}{\partial k} \\
&\simeq -\frac{q^2}{m\omega^2 \mathcal{V}} \sum_{\mathbf{k}} f_{\mathbf{k}} \simeq \frac{N}{\mathcal{V}} \frac{q^2}{m\omega^2} = \frac{nq^2}{m\omega^2},
\end{aligned} \tag{3.49}$$

to first order in q . Thus, the eigenfrequency of the most energetic pole, up to order q^2 , is

$$\omega^2 = \frac{nq^2 V(q)}{m}. \tag{3.50}$$

Substituting the Fourier transform of the Coulomb potential in 3D and 2D in Eq. (3.50), one retrieves the plasma frequency, which is independent of the momentum transfer q in

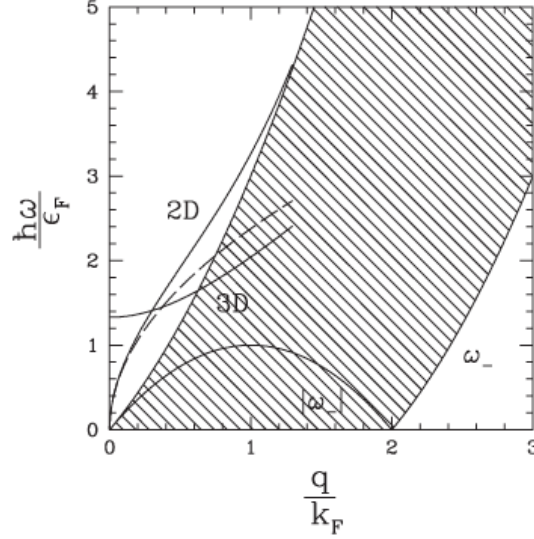


Figure 3.6: Plasmon dispersion relation for 3D and 2D interacting electron gases. For small q the plasmon curves lie outside the electron-hole pair continuum. When the respective critical q is reached, the plasmon mode decays into electron-hole pairs. Figure reproduced from [GV08].

3D, but depends linearly on q in 2D:

$$\left\{ \begin{array}{l} 3\text{D} : \quad V(q) = \frac{4\pi e^2}{q^2} \quad \longrightarrow \quad \omega_{\text{pl}}^2 = \frac{4\pi e^2 n}{m} \\ 2\text{D} : \quad V(q) = \frac{2\pi e^2}{q} \quad \longrightarrow \quad \omega_{\text{pl}}^2 = \frac{2\pi e^2 n}{m} q \end{array} \right. \quad (3.51)$$

The dispersion relation of the plasmon mode for 3D and 2D is reported in Figure 3.6.

Note that there is no contradiction with the plasma frequency of a metal surface derived in the classical treatment and the 2D value of the plasma frequency, simply because a metal surface is a 3D semi-infinite system, not a 2D system. In the former case, the Fourier transform of the Coulomb potential yields

$$V_{\mathbf{q}}^{\text{ss}} = \int_{z<0} d^3r \frac{e^2}{r} e^{i\mathbf{q}\cdot\mathbf{r}} = \frac{1}{2} \int d^3r \frac{e^2}{r} e^{i\mathbf{q}\cdot\mathbf{r}} = \frac{2\pi e^2}{q^2}.$$

Thus, the plasma frequency of the semi-infinite electron gas is $\omega_{\text{pl, ss}}^2 = \frac{2\pi e^2 n}{m} = \frac{\omega_{\text{pl}}^2}{2}$, which is the asymptotic value of the surface plasmon dispersion relation (in the limit $q \ll k_F$) that was derived in section 3.1.

3.2.2 Wave function of the plasmon state

The poles of Eq. (3.46) give the excitation frequencies of the interacting electron gas. It is interesting to find an expression for the corresponding excited states, with particular interest in the wavefunction of the plasmon state.

In order to find the states corresponding to the poles of the susceptibility χ^{RPA} , one can start from the eigenvalue problem of Eq. (3.47), where the quantities are now operators acting on states of the system. In principle, the ground state of the interacting electron gas should be taken as a starting point. In the RPA framework, the interacting ground state is replaced by the ground state of the non-interacting electron system. This corresponds to choosing a non-interacting Hartree-Fock state constructed from a Slater determinant of single particle wavefunctions, satisfying the Schrödinger equation with the exchange correlation functional set to zero [Pit+07]. This is equivalent to neglecting the density correlations described in the previous section.

It has already been shown that the only possible excitations of the non-interacting electron gas are the electronic transitions of momentum transfer \mathbf{q} , which in the second quantization formalism correspond to any possible creation or annihilation of an electron-hole pair. Thus, any excited state of the non-interacting electron gas can be written as a superposition of creation and annihilation of an electron-hole pair

$$|\Psi(\mathbf{q})\rangle = \hat{O}_{\mathbf{q}} |HF\rangle = \sum_{\mathbf{k}} (x_{\mathbf{k}} a_{\mathbf{k}}^{\dagger} a_{\mathbf{k}+\mathbf{q}} - y_{\mathbf{k}} a_{\mathbf{k}+\mathbf{q}}^{\dagger} a_{\mathbf{k}}) |HF\rangle = \sum_{\mathbf{k}} |\Phi_{\mathbf{q}}(\mathbf{k})\rangle, \quad (3.52)$$

were the electron-hole pair basis set $\Phi_{\mathbf{q}}(\mathbf{k}) = (x_{\mathbf{k}} a_{\mathbf{k}}^{\dagger} a_{\mathbf{k}+\mathbf{q}} - y_{\mathbf{k}} a_{\mathbf{k}+\mathbf{q}}^{\dagger} a_{\mathbf{k}}) |HF\rangle$ was defined. The normalization condition is $\sum_{\mathbf{k}} (|x_{\mathbf{k}}|^2 - |y_{\mathbf{k}}|^2) = 1$. The eigenvalue equation to solve in this basis is thus:

$$\left[1 - \hat{\chi}_0(\mathbf{q}, \omega) \hat{V}_{\mathbf{q}}\right] |\Psi(\mathbf{q})\rangle = 0, \quad (3.53)$$

which can be stated as:

$$|\Phi(p)\rangle - \frac{1}{\mathcal{V}} \sum_{p'} \frac{f_p}{\omega - \epsilon_p} V_{p,p'} |\Phi(p')\rangle = 0, \quad (3.54)$$

where Φ is a function in the particle-hole basis set, the index p indicates any possible particle-hole pair transition and $V_{p,p'} = V(\mathbf{q}) 1_{p,p'}$ is a constant uniform matrix for a given \mathbf{q} . The substitution $f_p = f_a - f_b$ and $\epsilon_p = \epsilon_a - \epsilon_b$ were made, where a, b indicate the possible initial and final states. Separating the creation and annihilation components in $|\Phi(p)\rangle$, one obtains two coupled equations for the x_p and y_p contained in $|\Phi(p)\rangle$. Noting that $f_x = 1$ and $f_y = -1$, where the subscripts x, y refer now to the creation or annihilation part of $|\Phi(p)\rangle$, Eq. (3.54) can be cast into the coupled set of RPA equations (cf. [FW03], §50, p.

565):

$$\begin{aligned} (\omega - \epsilon_x)x - \frac{1}{\mathcal{V}} \sum_{x'} V_{x,x'} x' - \frac{1}{\mathcal{V}} \sum_{y'} V_{x,y'} y' &= 0, \\ (\omega - \epsilon_y)y + \frac{1}{\mathcal{V}} \sum_{x'} V_{y,x'} x' + \frac{1}{\mathcal{V}} \sum_{y'} V_{y,y'} y' &= 0. \end{aligned} \quad (3.55)$$

Defining X and Y as the vectors of all the possible pair creation and annihilation components respectively, the system (3.55) can be rewritten in matrix form:

$$\begin{pmatrix} A & B \\ -B & -A \end{pmatrix} \begin{pmatrix} X \\ Y \end{pmatrix} = \omega \begin{pmatrix} X \\ Y \end{pmatrix}, \quad (3.56)$$

where $A_{ij} = \epsilon_X \delta_{ij} + v 1_{ij} = v 1_{ij} - \epsilon_Y \delta_{ij}$, $B_{ij} = v 1_{ij}$, v is the potential density V/\mathcal{V} and 1 is the all-ones matrix.

Before proceeding with the eigenvectors determination, it is relevant to re-calculate the highest eigenvalue from Eq. (3.53) using Eq. (3.23) for the susceptibility of a non-interacting electron gas. The further approximation employed is that the electron gas is fully degenerate, so that $\epsilon_{\mathbf{k}} - \epsilon_{\mathbf{k}+\mathbf{q}} = \Delta\epsilon$, for any value of \mathbf{k} . This would correspond in Figure 3.5 to a collapse of the vertical lines relative to the single electron-hole excitation frequencies to a unique vertical asymptote. In this approximation it is straightforward to show that the eigenfrequencies are given by

$$\omega = \Delta\epsilon \sqrt{1 + \frac{2v}{\Delta\epsilon} \sum_p f_p}, \quad (3.57)$$

where only the positive part of the spectrum was considered. Thus, the maximum eigenvalue, corresponding to the rightmost pole in Figure 3.5 is obtained in the case where all the p 's refer to electron-hole pair creation, such that $f_p = 1 \forall p$. In this case the maximum frequency is

$$\omega_{\max} = \Delta\epsilon \sqrt{1 + \frac{2\mathcal{N}v}{\Delta\epsilon}}, \quad (3.58)$$

where \mathcal{N} are all the possible excitations of electron-hole pairs for a given momentum transfer \mathbf{q} , and are thus the number of available \mathbf{k} states of the system. For a large number of states, Eq. (3.58) is approximated as

$$\omega \simeq \sqrt{2\mathcal{N}v\Delta\epsilon} = \sqrt{2nV\Delta\epsilon} = \sqrt{\frac{nVq^2}{m}}, \quad (3.59)$$

where the particle density $n = \mathcal{N}/\mathcal{V}$ and $\Delta\epsilon = q^2/2m$ were used. Thus, one recovers the plasmon frequency of Eq. (3.50) as the eigenvalue corresponding to the most energetic

pole of χ^{RPA} . Rewriting of the system (3.55) in index notation yields

$$\begin{aligned}(\omega - \Delta\epsilon)x_i - v \sum_j (x_j + y_j) &= 0, \\(\omega + \Delta\epsilon)y_i + v \sum_j (y_j + x_j) &= 0.\end{aligned}\tag{3.60}$$

At first, a relation between the pair creation and annihilation eigenvector elements can be found by summing the equations in (3.60), which gives

$$y_i = -\frac{\omega - \Delta\epsilon}{\omega + \Delta\epsilon}x_i, \quad \forall i.\tag{3.61}$$

Substituting Eq. (3.61) into the first equation of (3.60) one gets

$$(\omega - \Delta\epsilon)x_i - V \left(1 - \frac{\omega - \Delta\epsilon}{\omega + \Delta\epsilon}\right) \sum_j x_j = 0 \longrightarrow (\omega^2 - \Delta\epsilon^2)x_i + 2V\Delta\epsilon \sum_j x_j = 0.\tag{3.62}$$

Eq. (3.62) can be satisfied in two cases: the first is for $\omega = \Delta\epsilon$ (where again the negative part of the eigenvalue spectrum was discarded), which can occur only if the sum $\sum_j x_j = 0$. An orthonormalization gives eigenvectors of the form:

$$X_i = \begin{pmatrix} 1 \\ -1 \\ 0 \\ \vdots \\ 0 \end{pmatrix}, \quad Y_i = -\frac{\omega - \Delta\epsilon}{\omega + \Delta\epsilon} \begin{pmatrix} 1 \\ -1 \\ 0 \\ \vdots \\ 0 \end{pmatrix},\tag{3.63}$$

which correspond to $2p - 2h$ states and are responsible for charge density oscillations [All96]. For $\omega \neq \Delta\epsilon$, Eq. (3.62) can be satisfied for $\omega = \omega_{\text{max}}$ only by $\sum_j x_j = \mathcal{N}$, which corresponds to assuming that all the possible electron-hole states sum up *coherently*, giving as resulting eigenvectors

$$X_{\text{pl}} = \begin{pmatrix} 1 \\ 1 \\ 1 \\ \vdots \\ 1 \end{pmatrix}, \quad Y_{\text{pl}} = -\frac{\omega - \Delta\epsilon}{\omega + \Delta\epsilon} \begin{pmatrix} 1 \\ 1 \\ 1 \\ \vdots \\ 1 \end{pmatrix},\tag{3.64}$$

which can now be identified as the plasmon eigenvectors. The remarkable property of the plasmon eigenfunction is thus, that it is constituted by a coherent superposition of all the possible electron transitions for a given momentum \mathbf{q} , typically set by the external perturbation potential. For this very reason, the plasmon mode is called a collective mode

and its spectral amplitude is much larger than that of any single particle excitations, such that it is manifest at macroscopic level.

Although the physical insights provided by the random phase approximation are simple and fascinating, the main criticality of this approach is that for long wavelength it doesn't prescribe any decaying mechanism for the plasmon mode, which is known to be very lossy.

3.3 Excitation of SPPs

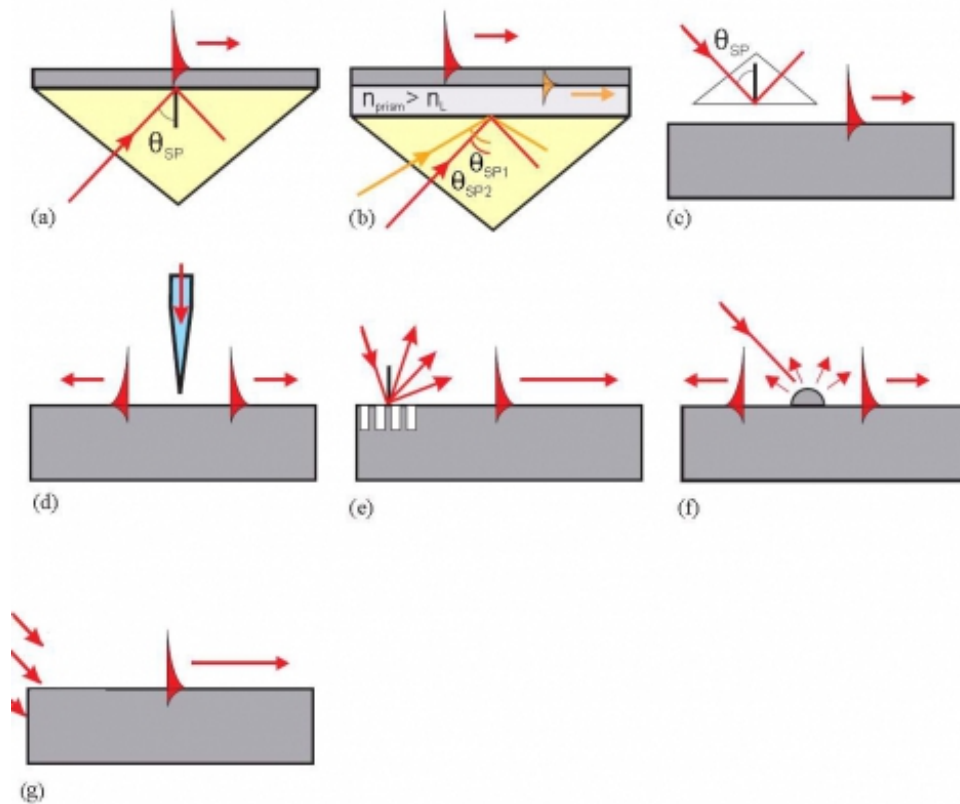


Figure 3.7: Excitation mechanisms of SPPs: in the Otto configuration (a) the plasmonic field at the metal-air surface is excited by frustrated total internal reflection (TIR) at the dielectric-metal surface. Variants of this scheme are the Kretschmann configurations (b-c) where the metallic material is not directly in contact with the TIR dielectric. In the grating coupling (e) the plasmonic field is generated at the grooves of the diffraction grating by the evanescent field produced according to Eq. (3.66). In (d-f-g) typical examples of near-field coupling are shown. An SPP can be launched by the near field around a metal tip (d), by scattering of a light wave with a surface dot or defect (f), or with an edge of the metallic material (g). Figure reproduced from [ZMC11].

The strategy to excite an SPP is to augment the parallel k-vector of the excitation source, in order to achieve matching with the surface plasmon wave vector, see Figure 3.7 for an illustration. One way of “coupling” a source to an SPP is to overlay a dielectric material on the metallic surface. Often used are the Otto [Ott68] and Kretschmann [Kre71] configurations, which differ in the dielectric position in contact or closely above the surface. The additional k-vector needed to satisfy the matching condition is provided by passage through the dielectric, which enhances the parallel component by $k_{\parallel} \rightarrow n_{\text{diel}}k_{\parallel}$, assuming that $n_{\text{diel}} \sin \theta > 1$ (see Figure 3.8).

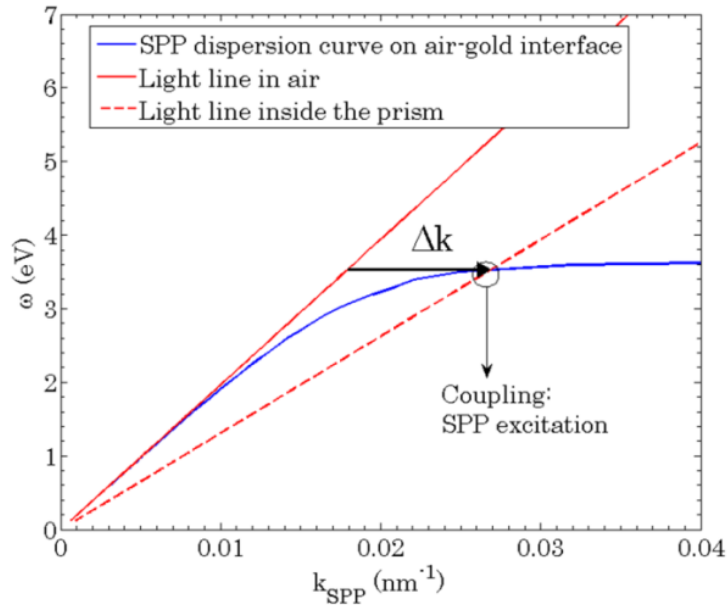


Figure 3.8: Diagram of SPP excitation in the prism coupling configuration. The passage of the incident light through the glass “increases” the light wavevector, providing the additional momentum Δk necessary for the phase matching. Figure reproduced from [RZR12].

Another way is the grating coupling: the source is shone on a diffraction grating with lattice constant a . The additional k-vector is provided by the periodicity of the grating. In fact, the discrete translational invariance along the grating grooves “folds” the SPP dispersion relation back into the first Brillouin zone (FBZ), making the matching possible. The matching condition in this setup is $k_{\text{spp}} = k_{\parallel} + nq$, where n is the diffraction order and q is the wave number associated to the grating periodicity. Figure 3.9 shows the effect of the discrete periodicity on the SPP dispersion relation. Apart from the formation of Brillouin zones, it is interesting to notice the appearance of plasmonic band gaps, originating from the resolution of the degeneracies of the modes $(n, -n)$ at the center of the FBZ, and $(n, n \pm 1)$ at the borders.

Yet another way is to exploit the near field localized at tips, dots or surface defects.

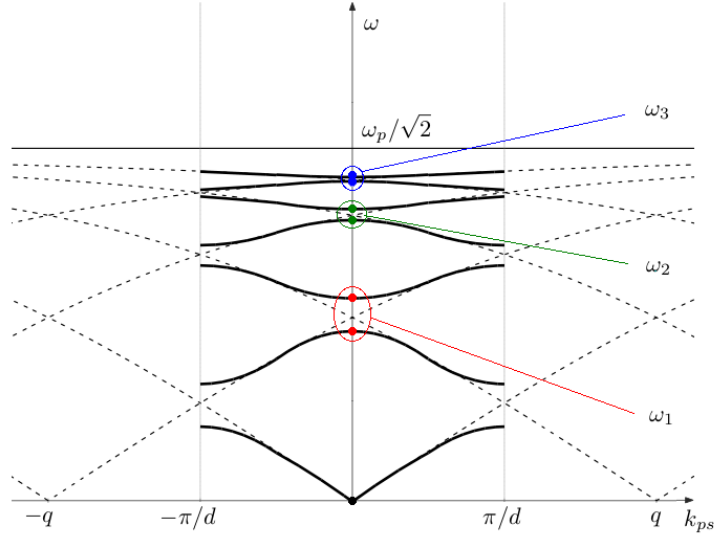


Figure 3.9: Plasmonic band structure produced in the grating coupling mechanism. The excitation of SPPs is possible also for normal incidence. The non-zero amplitude of the grating grooves lifts the degeneracy in the crossing of the bands $(n, -n)$ at the center of the FBZ, and of bands $(n, n \pm 1)$ at the borders. Note that the origin of the gap opening is the same as in the band structure theory: the grating groove amplitude plays the role of the solid periodic potential.

The intuitive reason behind this kind of coupling is that the sub-wavelength dimensions $r \ll \lambda$ of the considered object provide a large additional momentum $\Delta k \sim 1/r$ compared with the source momentum k_0 . A more rigorous explanation can be given by means of the Weyl expansion [Wey19]. The spherical radiation field of a point-like source can be expanded as:

$$\frac{\exp(ikr)}{r} = 2i\pi \int_{-\infty}^{\infty} \frac{d\alpha}{2\pi} \int_{-\infty}^{\infty} \frac{d\beta}{2\pi} \frac{1}{\gamma} \exp[i(\alpha x + \beta y + \gamma|z|)], \quad (3.65)$$

where $\alpha^2 + \beta^2 + \gamma^2 = k^2$ and $\text{Im}\{\gamma\} > 0$. Thus, the field of a point-like source contains evanescent waves that decay away from the source with $|z|$. Hence, a point-like source above an interface illuminates it with evanescent waves that can easily couple into SPP modes.

So far the need to “augment” the source parallel k -vector was motivated with the argument that at a given frequency, the plasmonic wave vector is always larger than the one of the source. From a physical point of view, this can be better understood by considering that the electron charge density perturbation δn is driven, via the Poisson’s law, by the

divergence of the electric field $\delta n \propto \nabla \cdot \mathbf{E}$. Since a plane wave is transversal, it cannot give rise to a charge density perturbation on the surface and therefore one needs a tool, or a configuration, to break the transversality of the source. In the prism coupling this is provided by the total internal reflection (TIR) of the source at the dielectric interface, which generates an evanescent wave extending to the other side of the surface. As discussed above, an evanescent wave has a field gradient in the propagation direction satisfying $\nabla \cdot \mathbf{E} \neq 0$. The condition is also satisfied in the grating coupling: the grating equation in fact reads

$$\sin \theta_n = \sin \theta_0 + n\lambda/a, \quad (3.66)$$

where θ_n is the direction of the n -th diffracted order, θ_0 the incidence angle, and a the grating periodicity. Next to a finite set of real diffraction orders $|\sin \theta_n| < 1$, there is also an infinite set of complex waves, actually evanescent waves, for $|\sin \theta_n| > 1$, having non null divergence. Eventually, the excitation of SPP via near field coupling automatically satisfies the non-null divergence condition, since this is the main property of a near field!

3.4 Ultrafast plasmon dynamics

So far the properties of plasmonic fields have been discussed without addressing any time domain property. In general, the physics of surface plasmon is well captured by studies performed in the frequency domain, since the electronic properties of metals are well described in the linear response theory. However, a precise description of the temporal behavior in the transient excitation phase can not be given in term of spectral theory. This is even more important in materials like semiconductors or showing strong electronic correlations, where the metal approximation fails, and the electronic response must be treated in term of non-equilibrium theories [Ram91]. Thus, given the importance of ultrafast plasmonics for the potential applications in the field of all-optical based computer (see for reference [Ozb06]), it is interesting to frame the basic properties of plasmonic temporal response, and select some experimental tools able to access its transient dynamics. As already mentioned, some temporal features can be deduced by spectral analysis of the plasmon resonance.

The first remark concerns the generation of pulsed SPP fields. The reflectivity spectrum of a gold grating illuminated at normal incidence is shown in Figure 3.10. The linewidth of the plasmonic resonance is narrow with respect to the broad band of a few cycle near infrared (NIR) laser pulse. The grating structure acts as a bandpass, such that only a restricted amount of frequencies are coupled into SPPs. As a consequence, excitation with a source as short as 4 fs (cf. Figure 3.10) is expected to give rise to an SPP pulse longer than the driver one. The generation of *broadband* SPP pulses is of fundamental importance for instance for ultrafast on-chip communications, but poses major technological difficulties. While the excitation of a monochromatic SPP can be done with very high efficiency (cf. Figure 3.10), the generation efficiency of a broadband SPP pulse is only of few percents, and typically the coupling mechanism has to be specifically designed for the desired SPP

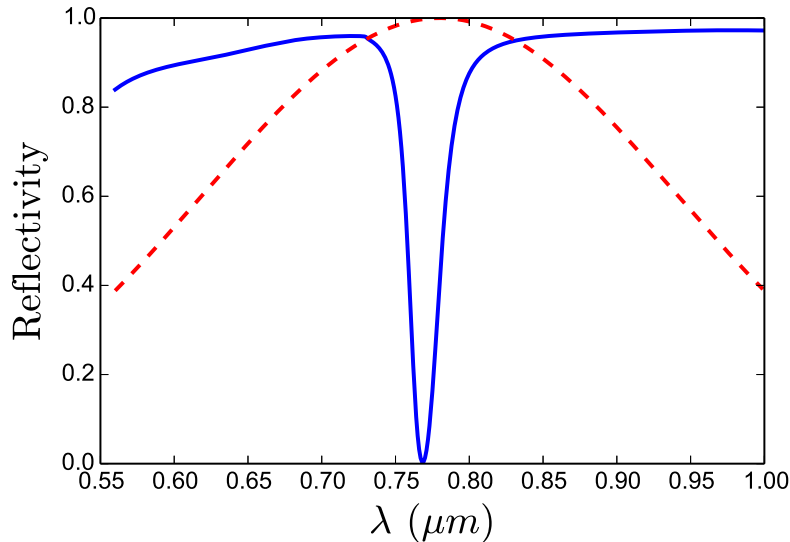


Figure 3.10: Simulation of the reflection spectrum of a gold square grating structure with the Rigorous Coupled Wave Analysis (RCWA) method, implemented in the software package RODIS [DD95]. The incident field is a short Ti:Sapphire laser pulse of $\lambda = 780$ nm and pulse duration 4 fs FWHM in intensity, the grating periodicity is $a = 730$ nm, the width of the grooves is $d = 400$ nm and the groove depth is $h = 40$ nm. The solid (red) curve is the reflectivity spectrum of the grating, the dashed line (blue) is the band of the laser pulse.

mode. Moreover, the SPP propagation is affected by a strong group velocity dispersion (GVD), given the strong dependence of the plasmon dispersion relation on the surface dielectric function. Thus, a broadband SPP propagating on a flat interface suffers from strong spatial and temporal dispersion as well chirping, requiring the engineering of a 2D photonic crystal-like structured surface. An interesting example can be found in [Ash+13].

Another time dependent feature which can be deduced from the line shape of the plasmonic resonance is the phase difference between the source and the excited SPP pulse. In the limit of $|\varepsilon'| \gg 1$ and $\varepsilon'' \ll |\varepsilon'|$ the resonance shape function $R(\omega)$ can be approximated by a Lorentzian curve:

$$R = 1 - \frac{\gamma_i^2}{(\omega - \omega_{\text{spp}})^2 + \gamma_i^2}, \quad (3.67)$$

where ω_{spp} is given by inverting Formula (3.10), γ_i is the Ohmic loss factor and γ_{rad} is the radiative loss factor. This is valid for flat surfaces. For propagation along a diffraction grating a radiation loss term γ_{rad} due to the back scattering of the SPP into far field has to be taken into account. In such cases γ_{rad} is the dominant loss term for grating with large

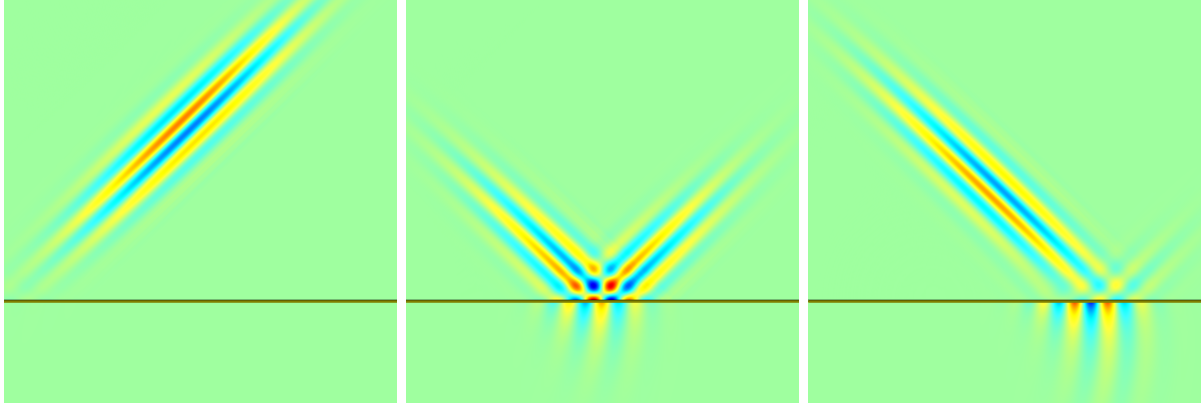


Figure 3.11: Finite-Difference Time-Domain [Taf05] simulation of SPP excitation in the Otto configuration by means of a three cycle short pulse with CEO phase of 90° on a gold slab: the pulse is incident on the surface at $\theta = 41.5^\circ$ (left) with respect to the normal to the gold surface. The angle is chosen to phase match the plasmon wave vector $k_{spp} = n_{diel}k_0 \sin\theta$, with $n_{diel} = 1.5$. The TIR evanescent field generated during reflection (center) excites an SPP with CEO phase equal to zero. Note that the SPP maximum intensity (right) is reached after the reflection turning point (center).

groove depths. The subtracted quantity in Eq. (3.67) is the absolute value of

$$s = \frac{\gamma_i}{\omega - \omega_{spp} + i\gamma_i}. \quad (3.68)$$

The phase change with respect to the driving source is given by:

$$\phi = \arctan\left(\frac{\text{Re}\{s\}}{\text{Im}\{s\}}\right) = \arctan\left(\frac{\gamma_i}{\omega - \omega_{spp}}\right) \rightarrow \phi(\omega = \omega_{spp}) = \frac{\pi}{2}. \quad (3.69)$$

The phase shift for SPP excited by a short pulse is illustrated in Figure 3.11 in the Otto configuration. The $\pi/2$ -shift is clearly observable. Also surface plasmons on metal nanoparticles show the same dephasing effect when resonantly excited. In Figure 3.12 a comparison between resonant and off-resonance response is illustrated.

3.5 Standard SPP imaging techniques

Despite the difficulty posed by the non-radiative nature of SPPs, there are a number of well developed methods for the imaging of surface plasmonic fields. Most of them concern the characterization of the spatial distribution of the plasmonic field, with one exception based on autocorrelation measurement of the temporal plasmonic signal, which will be presented at the end of the section.

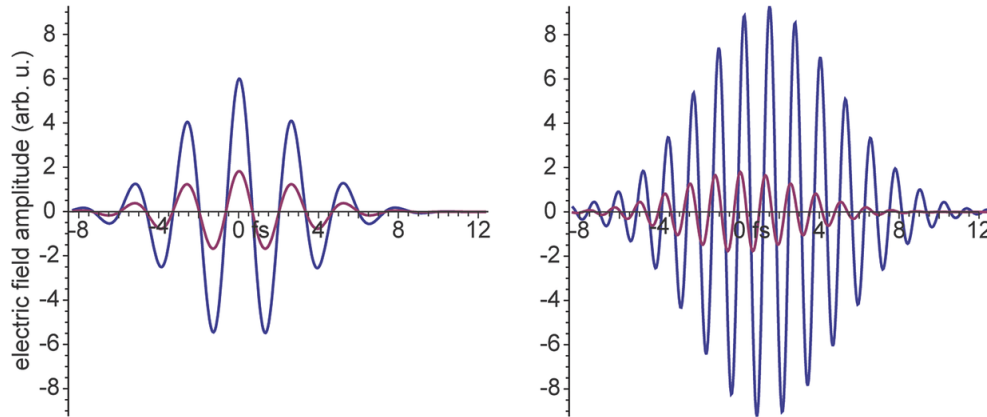


Figure 3.12: Comparison of the field generated in response to a short NIR pulse excitation of a silver nanoparticle with diameter of 80 nm. Out of resonance (left) the nanoparticle response is synchronous with the driver field. At resonance (right), the plasmonic field is dephased by 90° w.r.t. the driver pulse. Also observable is the increased time duration of the plasmonic field and the field enhancement. Figure reproduced from [Pre+13].

For the experimental characterization of the electromagnetic field of the surface plasmon, the most ubiquitous technique is Scanning Near-Field Optical Microscopy (SNOM), a scanning probe technique which allows the direct measurement of electromagnetic field intensity near surfaces. The technique consists in placing a microscopic tip (probe) in the vicinity of the surface field via a positive feedback technique. The probe tip, a tapered optical fiber, couples the evanescent plasmonic field into a propagating waveguide mode, consenting the measurement of the relative photo-current. For its similarity with the electron scanning tunneling microscope, SNOM in this configuration is often called photon scanning tunneling microscopy (PSTM).

Another way of imaging SPPs is using fluorescence emitters as markers of the plasmonic fields, as in Ref. [Dit+02]. Since the fluorescence signal is directly proportional to the plasmon intensity at the place of the emitter, by covering the propagation range of the plasmon with markers one can retrieve informations on its localization. Alternatively, one can directly tailor the radiation losses of the plasmon into a dielectric substrate, by exploiting the prism coupling mechanism [Dit+03]. This “leakage radiation” allows to measure the spatial intensity profile of a plasmon, or, in different arrangements, to directly observe the plasmon dispersion relation.

Yet another technique is called Scattered Light Imaging [DL04], where by analogy with the grating coupling, the plasmonic field properties can be inferred by studying the plasmon scattering from surface defects or random roughness, which convert the plasmon back into photon.

Apart for the SNOM, the techniques mentioned above only allow for indirect measurements of the SPP. In any case, the measurement of the SPP field by means of a dielectric tip

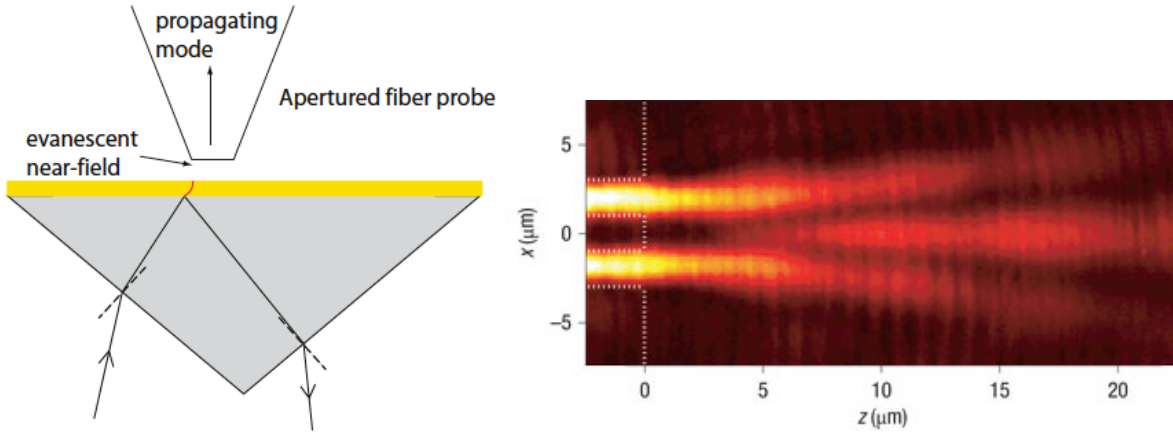


Figure 3.13: Left side: schematics of SNOM in a typical setup for the measurement of plasmonic fields. Figure reproduced from [Mai07]. With this technique it is possible to image the spatial distribution of the plasmon intensity. Right side: example of imaging of the SPP field intensity in a double slit experiment. SPPs are let propagate on gold stripes of $2 \mu\text{m}$ section, at $2 \mu\text{m}$ distance. After emerging from the waveguide ends, they produce the typical Young's diffraction pattern. Figure reproduced from [ZB07].

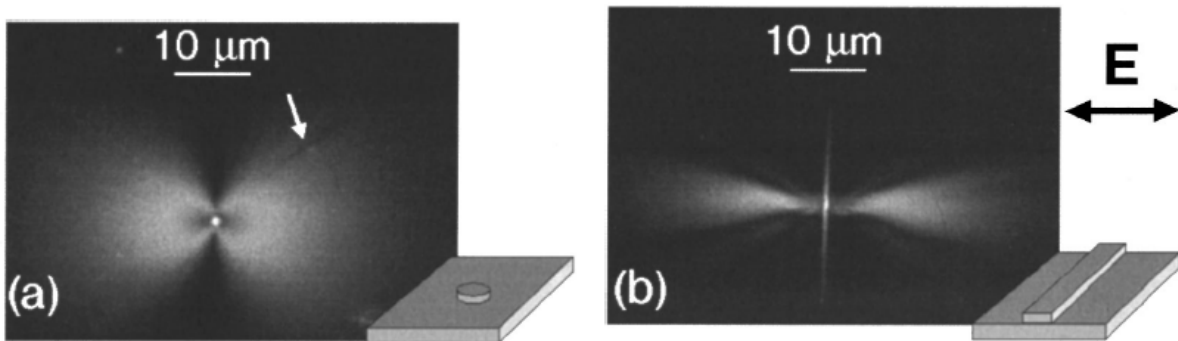


Figure 3.14: Fluorescence imaging of SPP intensity excited on (a) a silver nano-dot (diameter 200 nm , height 60 nm), and (b) a silver nano-wire (width 200 nm , height 60 nm , length $20 \mu\text{m}$). Figure reproduced from [Dit+02].

results in a modification of the field itself, constituting a major drawback for an otherwise powerful technique.

It has been recently demonstrated [Cin+05; Kub+05] that a non-invasive plasmon diagnostic tool is provided by employing the photo-electron emission microscope (PEEM) for the plasmonic near field.

A PEEM is based on the photoemission of electrons from the metal surface. A voltage difference system collects the emitted electrons, which form an image of the surface based on their spatial distribution. Since photoelectron emission is increased because of the plas-

monic field enhancement, it is possible to map the spatial distribution of the plasmonic field intensity without perturbing the system. In experiments, the multiphoton photoemission processes, typically two-photon photoemission (2PPE) [Sch+02], are employed, since they are extremely sensitive to local field intensity.

In Ref. [Kub+05] it was presented an experiment combining the nanometric spatial resolution of PEEM with an interferometric time resolved (ITR) 2PPE technique [Oga+97]. By analyzing the intensities of the field enhancement spots on a silver grating surface as a function of the pump-probe delay time, it was possible to determine the time evolution of the “hot spot” via the instantaneous photoemission intensity with femtosecond temporal resolutions. The ITR-2PPE PEEM technique is one of the first experiments combining space- and time-resolution on the nanometer and femtosecond scale, respectively. An example of the ITR-2PPE PEEM measurement is reported in Figure 3.15

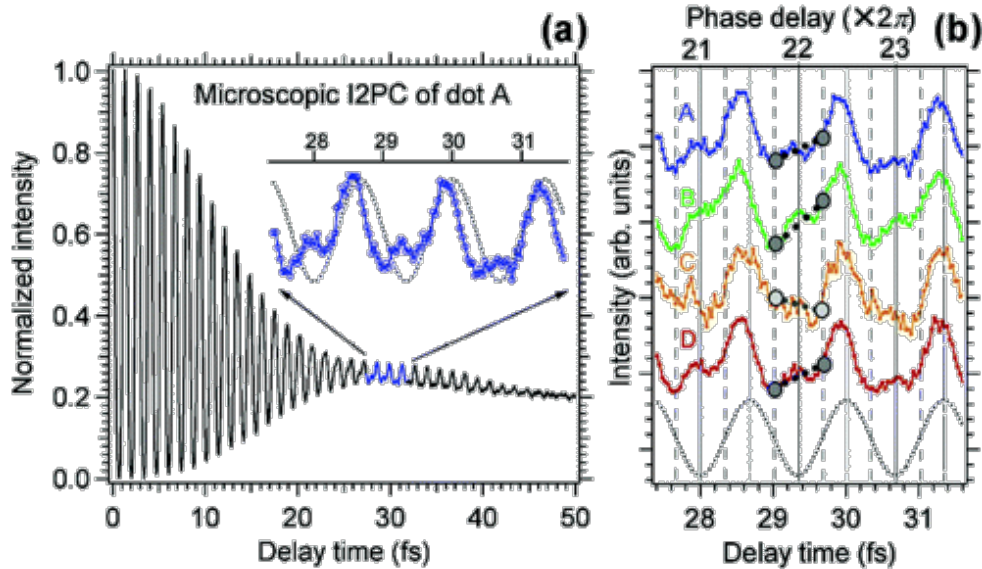


Figure 3.15: (a) Interferometric two-photon correlation of the photoemission intensity from a distinct hot spot (A in inset). A comparison (b) of the temporal signals measured from separate hot spots reveals different individual dynamics. Figure reproduced from [Kub+05].

Since the importance of the CEO phase has been mentioned in Chapter 2, it is interesting to report the method proposed in Ref. [Irv+06] to analyze the photoemission spectrum of a gold surface when an SPP is excited onto it. It was shown that for short enough plasmon pulses, the photoelectron spectrum is strongly dependent on the CEO phase (see Section 2.3) of the SPP wave-packet, which is in turn dependent, although phase shifted according to the resonance line shape, on the CEO phase of the driver pulse. However, since the coupling mechanism in general acts as a band pass filter on the spectrum of the excitation source, CEO phase effects on SPP tend to be weaker than in optical pulses.

3.6 Plasmonics in attosecond physics

The attempt to apply attosecond metrology to the imaging of surface plasmons has been carried out as an extension of the aforementioned time resolved photoemission microscopy, with a pump-probe experiment performed as in the attosecond streak camera (ASC) setup, where an XUV attosecond pulse releases photoelectrons in the probe field of the plasmon near field. So far conceptual setups have been investigated, where localized plasmon resonances act as photoelectron sources in stead of gas atoms.

The biggest physical difference with the ASC is in the streaking regime. In ASC, the electric field streaking a photoelectron released from an atom can be considered spatially homogeneous, since it extends over a region far bigger than the typical atomic scale. Therefore, the photoelectron experiences the electric field for the entire pulse duration, and its final momentum is given by Eq. (2.10), which is reported here for the reader's convenience:

$$p_f = p_i(t) - A(t - \tau).$$

Here t is the photoionization time. On the contrary, the near-field of an LSPR is highly inhomogeneous, with strong field gradients extending over a nanometric region. In this regime the interaction can be “instantaneous”, in the sense that photoelectrons experience a sudden “kick” in the plasmonic field and leave immediately the high field region. In this case the final photoelectron momentum is given by:

$$p_f = p_i(t) - E(t - \tau). \quad (3.70)$$

The discriminating parameters determining the streaking regime are the pulse cycle T_L and the pulse duration τ_L , which have to be compared with the time a photoelectron interacts with the streaking field. Equivalently, one can compare the typical displacement of the photoelectron with the spatial extension of the LSPR field. If the interaction time τ_{int} is larger than the pulse duration, the photoelectron experiences the entire streaking field, and the regime is called “ponderomotive”. If on the other hand τ_{int} is much smaller than the laser cycle, the regime is said “instantaneous”. The streaking regimes are reported in Figure 3.16. Thus, when using plasmonic fields created by sharp nanoscale structures the streaking can be instantaneous, because of the strongly localized field. An example of this streaking regime is reported in [Sto+07]. There, an attosecond pump-probe measurement is combined with a PEEM, in order to create a nanometer-scale attosecond-time resolution imaging technique. The technique proposed in [Sto+07] requires a very complex experimental setup, and its demonstration is, to the author knowledge, not yet been performed.

Nevertheless, the imaging of LSPR on metal nanoparticles via the standard attosecond streaking setup was proposed and numerically simulated in Ref. [SK11]. Since in the setup a time-of-flight (TOF) detector is employed, it is not possible to spatially resolve the streaked photoelectrons. Therefore, differently from streaking in atoms, the recorded

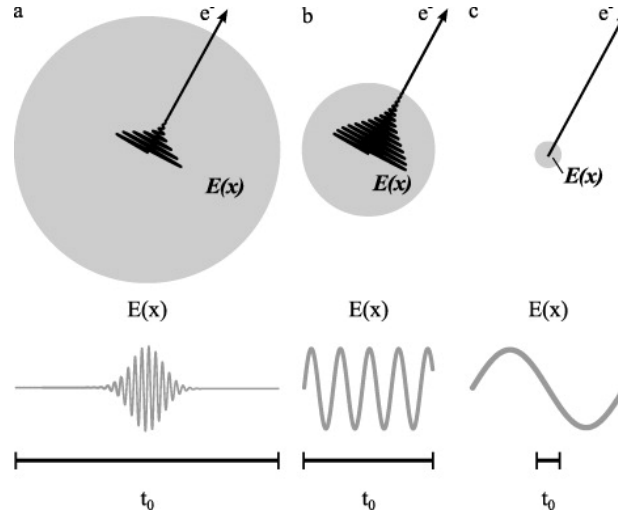


Figure 3.16: The streaking regime is determined by the interaction time of a photoelectron in the streaking field. If τ_{int} is longer than the laser pulse duration τ_L (a), the streaking is said to be ponderomotive, while in the opposite regime, for τ_{int} much shorter than the laser cycle T_L it is instantaneous (c). An intermediate regime can also be identified (b), for interaction times longer than the laser cycle, but shorter than the laser pulse duration: $T_L < \tau_{int} < \tau_L$. Figure reproduced from [KKV12].

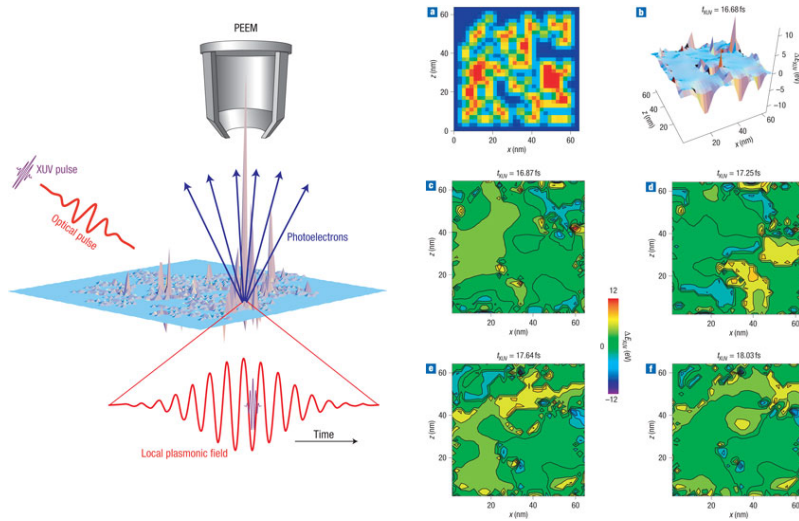


Figure 3.17: Schematics of the attosecond nanoplasmonic-field microscope (left). The NIR pulse excites the plasmonic field on a surface with random defects (a), which acts as the streaking field in instantaneous regime. The PEEM is able to collect electrons with nanometer resolution, allowing for the spatio-temporal imaging of the surface plasmonic response (c-f). Figures reproduced from [Sto+07].

spectra contains contributions from different photoelectron initial positions, and thus of different surface field intensities. As a result, the streaking spectrogram is smeared out by the superposition of photoelectrons accelerated in different regions of the spatially dependent plasmonic field. As shown in Figure 3.18, the smearing effect increases proportionally to the nanoparticle radius.

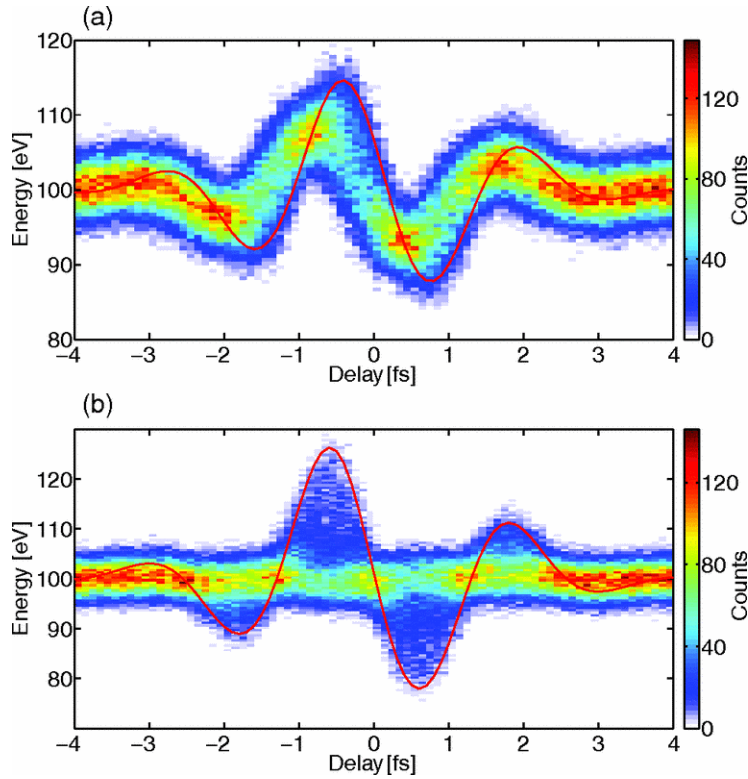


Figure 3.18: Attosecond streaking in the plasmonic field on a gold nanoparticle of diameter 10 nm (above) and 100 nm (below). The red lines show the contribution of the photoelectron trajectories launched at the poles of the nanosphere. It is observable a severe distortion of the streaking spectrogram already for very small radii. For larger nanoparticles, the streaking trace is smeared out. Figures reproduced from [SK11].

A final example of attosecond physics with plasmonic fields regards the streaking of photoelectrons emitted from metal nanotips. In this case, both the photoemission process and the streaking process have shown striking similarities with those observed in the standard setup involving gas atoms.

It was shown in [KSH11; Wac+12] that photoelectrons emitted in the plasmonic field undergo similar acceleration and recollision with the surface as in the gas case (cf. Figure 3.19), in such a way that the semiclassical three step model can be used to describe the underlying physical process. One of the reasons of this similarity is that the near field induced at the tip by the driving NIR pulse is not at resonance, and therefore the excursion

of the photoelectron is smaller than the near field decay length. Thus, the photoelectron acceleration occurs in the ponderomotive regime (cf. Figure 3.16), as in the case of photoemission from atoms. It has also been predicted that photoelectron rescattering at nanotip

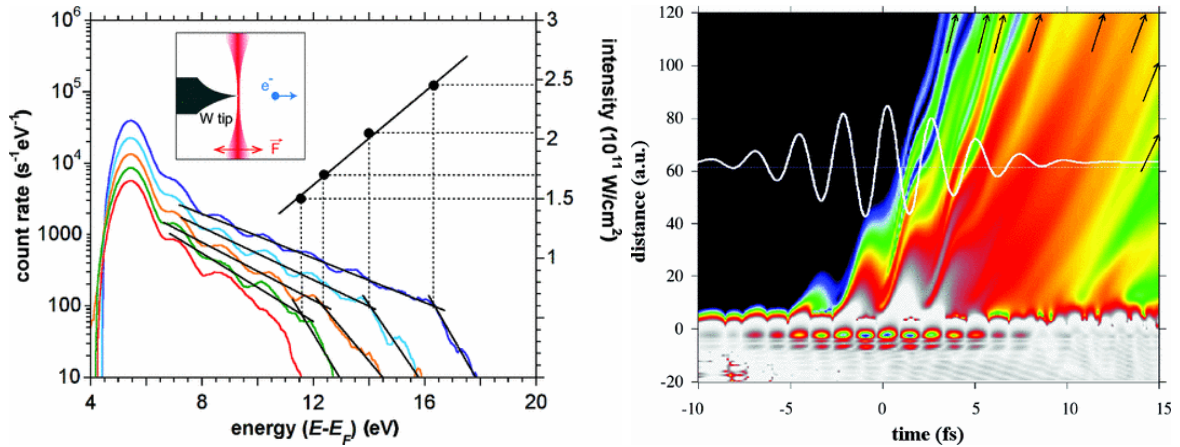


Figure 3.19: Left side: Above Threshold Photoemission (ATP) spectra from a metal nanotip at different field intensities. Right side: the photoelectron density map shows the trajectories of the rescattering electrons. Figures reproduced from [Wac+12].

would produce high harmonic radiation [Cia+14]. A fundamental difference with HHG from gas atoms is that even harmonics can be produced in this configuration, since the semi-infinite 1D geometry of the tip allows only one rescattering process per laser cycle.

The above threshold photoemission (ATP) from metal tips can also be used to perform streaking experiments. In Ref. [Wim+14] a spectrogram of a single-cycle terahertz fields produced in a light-induced air plasma was obtained by streaking the photoelectrons emitted from the nanotip under illumination of a NIR pulse. In Figure 3.20 the resulting streaking spectrogram is reported. It is interesting to observe how the imaging of the THz field was obtained by using exactly the same principle of the attosecond streaking technique, this time with the NIR as a pump field for the photoelectrons, and the generated THz field as a probe.

In Chapter 5 a new technique called Attosecond Photoscopy [Lup+14] is presented, which allows to perform the attosecond streaking of SPPs. The idea is to use a NIR pulse as a pump for the excitation of SPPs on a nanostructured surface, and attosecond pulses for ultrashort photoemission. With this technique it is possible to resolve sub-cycle features and the transient excitation phase of the SPP, which has not yet been demonstrated with the techniques discussed so far.

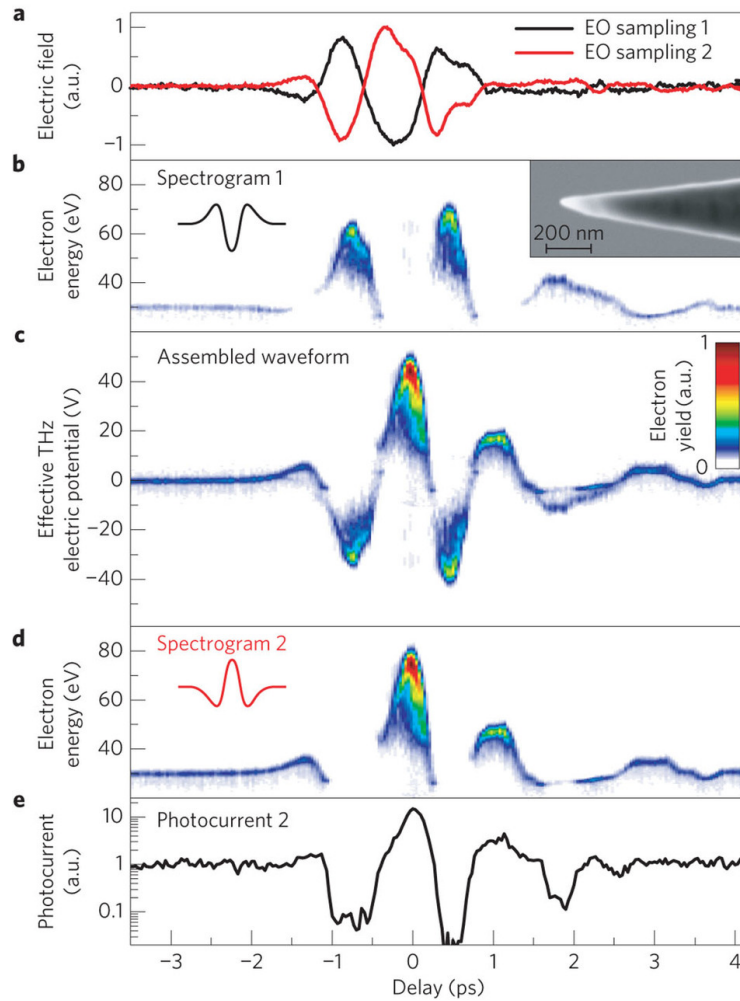


Figure 3.20: Streaking spectrogram of tip-emitted photoelectrons in a THz field produced in a light-induced air plasma. Figures reproduced from [Wim+14].

4

A Plasmon Enhanced Attosecond Extreme Ultraviolet Source

This Chapter is largely based on the work published in [LKS13]. Attosecond (AS) pulse sources are employed in the observation of electron dynamics at the time scales of atomic valence electrons. Such sources are mostly based on high harmonic emission from gases and are employed, for example, in attosecond streaking experiments of photoelectrons ionized in atoms [Dre+02; Rem+06], and solid surfaces [Cav+07].

AS pulse generation is an extremely non-linear frequency up-conversion process of the fundamental NIR driver pulse, which imprints its time-structure onto the harmonic radiation. The physical features of the process are described in Chapter 2. The classical three-step model [Cor93; KSK93] describes the physics of high harmonic emissions in terms of three sequential phases: ionization, quiver motion and recollision. The model predicts that in case of a recollision process resulting in the recombination of the electron with the ion, high harmonic radiation is emitted up to a maximal photon energy of $\hbar\omega_c = I_p + 3.2U_p$, where I_p is the ionization potential of the gas and $U_p = \frac{e^2}{4m_e} \frac{E_0^2}{\omega^2}$ is the driver ponderomotive potential of a laser of amplitude E_0 and frequency ω .

The non-linearity of the process is such that the highest part of the harmonic spectrum is produced only around the maxima of the NIR pulse, such that bursts of high frequency radiation as short as 67 attoseconds can be produced [Zha+12]. It also sets strict requirements on the pump intensity needed to obtain photons of the desired energy. For XUV photon energies $\gtrsim 40$ eV with Ti:sapphire NIR pulses at 800 nm wavelength, intensities \gtrsim W/cm² are needed.

The time-locking of the AS pulse to the NIR pulse allows to perform pump-probe experiments by controlling the relative time delay with a precision of ten attoseconds. In attosecond pump-probe experiments with delays beyond the laser half-period, one needs to use isolated single AS pulses, which are typically generated by using optical pulses which are so short, that only one field maximum effectively contributes to the generation of the desired photon energies [Bal+03]. Alternative techniques like polarization gating [Sol+06], where the laser polarization is manipulated in order to suppress high harmonic generation

for all but one field peak, are rather complex to use in spectroscopic experiments. In any case, while few femtosecond lasers at 80 MHz repetition rate are commercially available [Rau+08], the amplification required to reach the intensity of $\gtrsim 10^{14}$ W/cm² reduces the repetition rate to few kHz.

In this chapter a technique based on plasmonic enhancement for the generation of XUV attosecond pulses is proposed. Its main advantage is that the amplification mechanism is provided by the plasmonic field enhancement, which allows to directly use a commercial laser system as driving source, thus keeping the original high repetition rate.

4.1 Bow-tie structures for plasmonic enhanced HHG

A first generation mechanism based on plasmonic enhancement was proposed in [Kim+08]. A NIR laser pulse excites a localized surface plasmon resonance (LSPR) on a bow-tie shaped plasmonic structure exposed to a jet of Argon gas. In the middle of the structure (cf. Figure 4.1 for the illustration of the geometry) the intensity enhancement of 10^3 is such that the threshold intensity value for HHG can be reached with commercially available laser pulses of intensity $I_0 = 10^{11}$ W/cm². With this HHG setup, the authors of [Kim+08] claimed

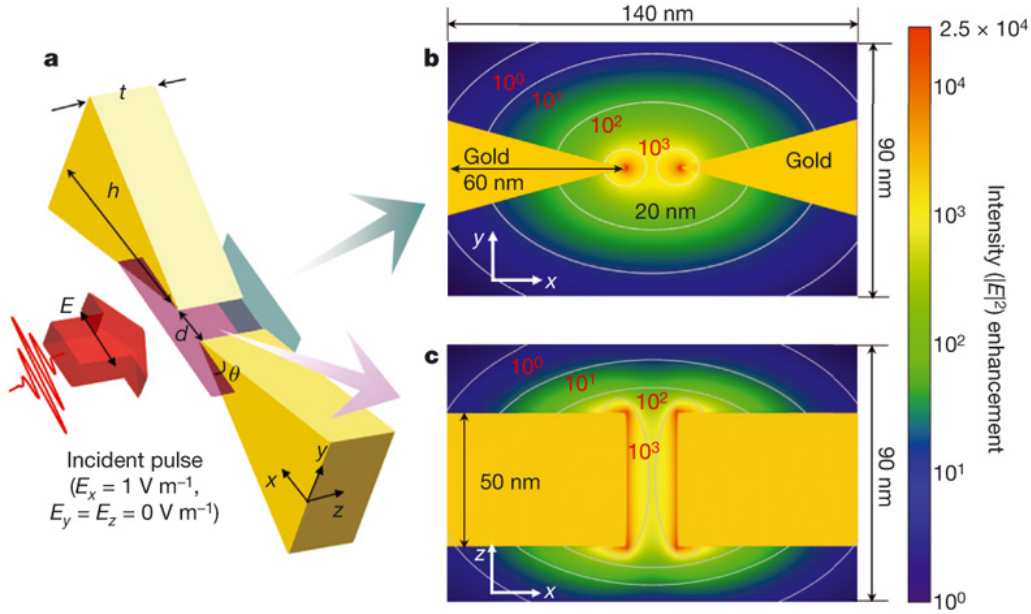


Figure 4.1: Experimental setup for XUV harmonic generation using the plasmonic enhancement of LSPR on bow-tie gold structures. The polarization of the laser field is set parallel to the horizontal symmetry axis of the structure. The intensity enhancement factor is $> 10^4$ at the apex of each triangle, while in the gap region between the triangles is 10^2 . The achieved intensity is enough to trigger HHG from Argon atoms. Figure reproduced from [Kim+08].

to observe harmonics up to the 17th order, a finding which was later debated (see Section 4.9). By illuminating a matrix of bow-tie nanostructures, the intensity of the produced harmonics can be boosted by constructive interference of radiation from multiple emitters. Nevertheless, the low coupling efficiency of the NIR laser with the LSPR of the plasmonic structure make the harmonic yield rather low.

4.2 Tapered plasmonic waveguides for HHG

To improve the low coupling efficiency of the laser field with the plasmonic resonance, in [Par+11] a new geometry was proposed, capable of bringing the coupling efficiency to nearly 100 %. The “amplification” scheme consists in the excitation of a cylinder Surface Plasmon Polariton (cySPP) by focusing a laser pulse into a tapered waveguide. As the plasmonic field propagates towards the narrow end of the waveguide, its wavelength decreases, while the field intensity increases. The experimental setup is shown in Figure 4.2. With this enhancement mechanism, in [Par+11] it was reported the detection of extreme ultraviolet (XUV) radiation up to the 43rd harmonic order in Xenon gas (see section 4.9). In a following theoretical study [Cho+12], attosecond time structure was found in the response of an isolated atom to the plasmon field.

In this Chapter, an analysis of the macroscopic XUV harmonic propagation is presented, in order to determine whether the high harmonics emitted from the gas atoms add up to form a usable beam with time structure of an isolated AS pulse. It was indeed found that the time structure of the generated XUV radiation is that of an isolated AS pulse. Furthermore, being generated by a single plasmonic mode, the pulse shows a very clean spherical wavefront and a good collimation degree, besides being stable under variation of the driver pulse duration and incidence angle.

On the other hand, the emission through the narrow end of the tapered waveguide is severely diffracted, while a well collimated attosecond beam propagates in the reverse direction. Moreover, the beam intensity of the generated AS pulse is several orders of magnitude smaller than what found in the original experiment in [Par+11], in agreement with what predicted theoretically in [Ras13].

We compare the “plasmon enhanced attosecond XUV source” (PEAX) to standard AS pulses produced from gas harmonic sources. Despite the significantly lower yield of the PEAX, the extremely clean spatial profile and the high repetition rate make it an attractive alternative source to standard gas harmonics for high resolution imaging.

The strategy to perform the numerical analysis of the described experimental setup is the following: (i) at first Maxwell’s equations are solved numerically for the plasmonic response of the tapered waveguide to the driver NIR pulse, (ii) then the atomic response to the so generated plasmonic field is calculated by solving the time-dependent Schrödinger equation (TDSE) for a set of atoms covering the highest enhancement region of the plasmonic field and eventually (iii) the waveguiding effect on the harmonic propagation is studied by solving the Maxwell equations for the collection of radiating dipole sources.

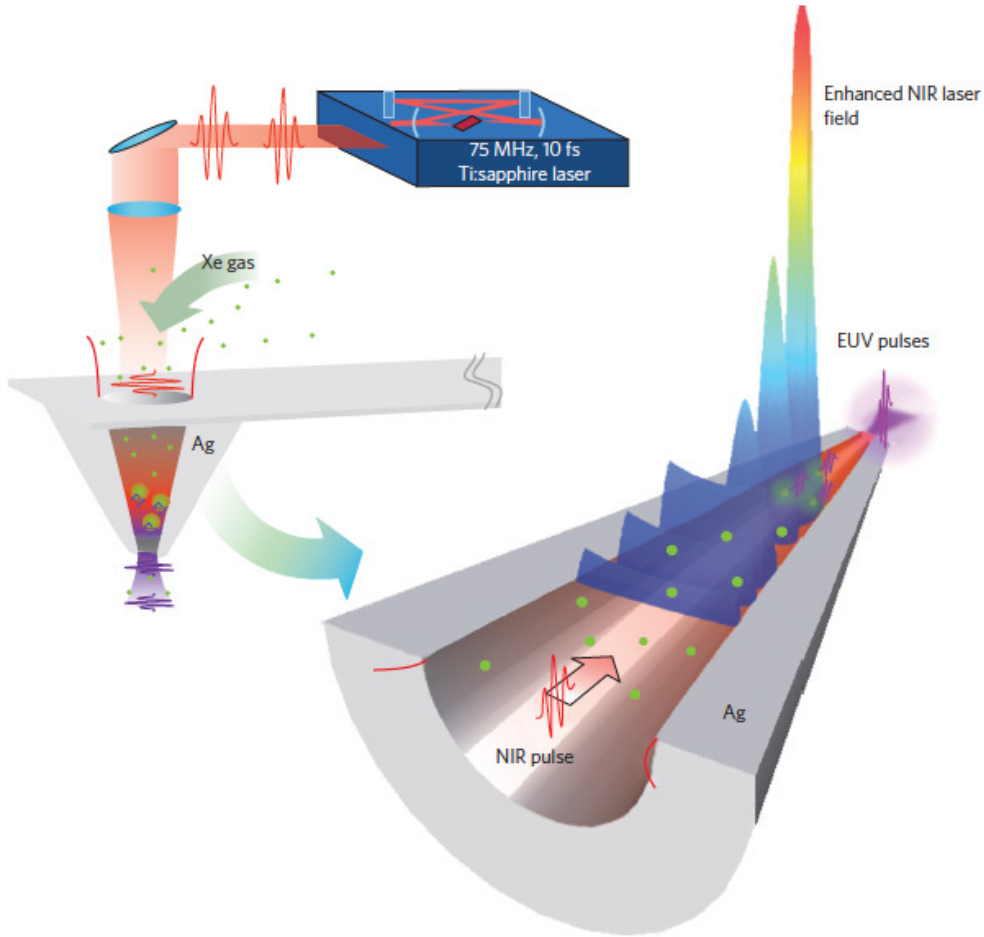


Figure 4.2: Experimental setup for XUV attosecond pulse generation using plasmonic enhancement. A cylindrical plasmon polariton (cySPP) is excited at the opening of a tapered waveguide, whose decreasing radius in the propagation direction squeezes the cySPP, causing a strong enhancement of its field intensity. The “amplified” field is sufficient to trigger high harmonic generation (HHG) in the gas atoms filling the waveguide. The emitted XUV radiation combines to form an isolated attosecond pulse which propagates through the narrow end of the waveguide, while the rest of the NIR radiation is filtered or diffracted. Figure reproduced from [Par+11].

4.3 Analysis of cylinder plasmon polaritons

Let us start with the boundary value problem of a metal cylinder embedded in a dielectric material and assume a fixed wavelength of 800 nm, at which the silver dielectric constant is $\epsilon_{\text{Ag}} = -24.9 + 1.86i$. At first, the imaginary part of the metal dielectric constant is neglected.

The dispersion relation of the propagating cySPP is obtained by setting to zero the determinant of the matrix of the electromagnetic field amplitudes obtained from applying the continuity boundary conditions at the cylinder radius R ([Str41], Chap. XI):

$$\left[\frac{1}{u} \frac{I'_m(u)}{I_m(u)} - \frac{1}{v} \frac{K'_m(v)}{K_m(v)} \right] \left[\frac{\epsilon_m}{u} \frac{I'_m(u)}{I_m(u)} - \frac{\epsilon_d}{v} \frac{K'_m(v)}{K_m(v)} \right] = -m^2 n_{\text{eff}}^2 \left(\frac{1}{u^2} - \frac{1}{v^2} \right)^2. \quad (4.1)$$

Here $u = \kappa_1 R = k_0 R \sqrt{n_{\text{eff}}^2 - \epsilon_m}$, $v = \kappa_2 R = k_0 R \sqrt{n_{\text{eff}}^2 - \epsilon_d}$, with $n_{\text{eff}} = h/k_0$. Propagating solutions correspond to $n_{\text{eff}} > \sqrt{\epsilon_d}$.

Differently from the planar case, for a mode of order m it is in general not possible to isolate a transverse electric or magnetic mode, except in the case $m = 0$, where the TE (left brackets content) and TM mode (right brackets content) are decoupled. In the limit of very large cylinder radius $k_0 R \gg 1$ the effective refractive index n_{eff} tends to the flat surface case for any value of m :

$$n_{\text{eff},m} = \frac{\epsilon_d \epsilon_m}{\epsilon_d + \epsilon_m}, \quad \forall m. \quad (4.2)$$

In the case of $m = 0$ the dispersion relation (4.1) simplifies for the TM case to

$$\frac{\epsilon_m}{u} \frac{I'_0(u)}{I_0(u)} = \frac{\epsilon_d}{v} \frac{K'_0(v)}{K_0(v)}, \quad (4.3)$$

In the limit of very small cylinder radius $k_0 R \ll 1$, assuming that the metal dielectric constant is large but of finite value, both $v, u \ll 1$. This approximation is valid at optical wavelengths, but fails for instance at micro waves. In the limit of small arguments Eq. (4.3) reduces to

$$\frac{\epsilon_m}{2} - \frac{\epsilon_d}{v} \frac{1}{v(\log \frac{v}{2} + \gamma)}, \quad (4.4)$$

where $\gamma = 0.57721$ is the Euler-Mascheroni constant and the relations $I'_0(v) = I_1(v)$, $K'_0(u) = -K_1(u)$ were used. After redefinition of $\tilde{\gamma} = e^\gamma = 1.781$, Eq. (4.4) can be cast into the form

$$\xi \log \xi = \eta, \quad \xi = \left(\frac{\tilde{\gamma} v}{2} \right)^2, \quad \eta = \frac{\tilde{\gamma}^2 \epsilon_d}{\epsilon_m}. \quad (4.5)$$

A first inspection of Eq. (4.5) shows that since $\eta < 0$, the solution must be in the interval $0 < \xi < 1$. Moreover, the function $\xi \log \xi$ has an absolute minimum of $-1/e$, and is zero for $\xi = 0$ and $\xi = 1$. Thus, the solutions of Eq. (4.5) can be two, provided that the condition (4.6) is verified:

$$\eta > -\frac{1}{e} \quad \longrightarrow \quad \frac{\epsilon_d}{|\epsilon_m|} < e^{-(2\gamma+1)} = 0.116. \quad (4.6)$$

For a silver waveguide at a wavelength of 800 nm, the condition is well satisfied. The solution of Eq. (4.5) can be expressed in term of continuous fractions, which can be

approximated for $|\eta| \ll 1$ as follows:

$$\xi = \frac{\eta}{\log \frac{\eta}{\log \frac{\eta}{\log \dots}}} \simeq \frac{\eta}{\log |\eta|}. \quad (4.7)$$

Thus, up to logarithmic accuracy, the propagation constant of the plasmonic mode $m = 0$ is given by:

$$n_{\text{eff}} = \sqrt{\epsilon_d - \frac{1}{k_0^2 R^2} \frac{2\epsilon_d}{\epsilon_m (\log \sqrt{-\epsilon_m/\epsilon_d} - \gamma)}}, \quad (4.8)$$

which is similar to what obtained in [Sto04], but is accurate up to values $k_0 R = 1$, as shown in Figure 4.3. It is interesting to notice that this mode exists for any radius R of

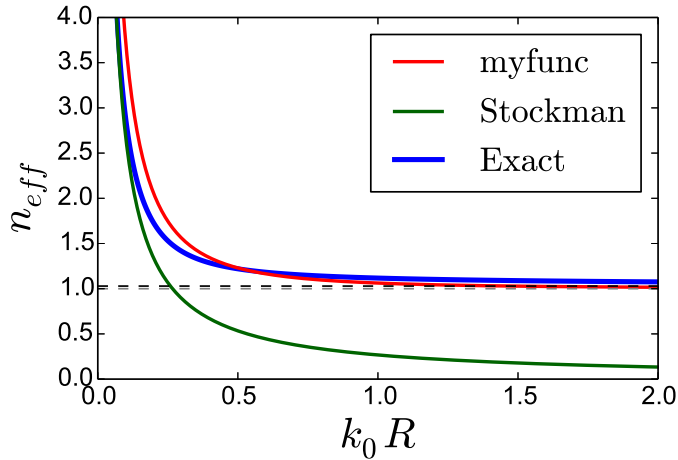


Figure 4.3: Comparison of the exact expression of the effective propagation index $n_{\text{eff}} = h/k_0$ for the mode $m = 0$ (blue thick line), with expression (4.8) (red) and the expression derived in [Sto04] (green). The agreement for small cylinder radii is confirmed. Although expression (4.8) seems to accurately approximate the exact propagation index for any values of R , at large radius Eq. (4.8) tends to $\sqrt{\epsilon_d}$ (dashed line) instead than to the flat surface index value of (4.2).

the cylinder and its propagation wavelength is proportional to the cylinder radius. It is called the *nanowire mode*, since it is the only one that does not experience any cut-off for $R \rightarrow 0$. The behavior of higher order modes is reported in Figure 4.4. As observable in Figure 4.4, there is finite value of the cylinder radius where the modes $m > 0$ have a cutoff in the propagation constant, which corresponds to the turning point at which the mode is reflected along the waveguide axis. Therefore, high order mode cannot be focused to arbitrary small scales.

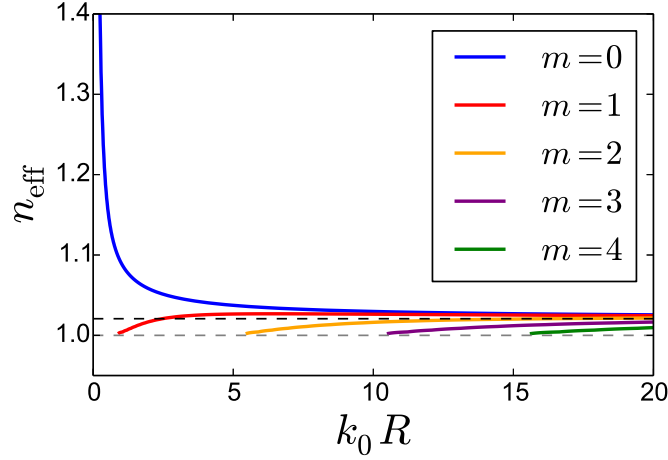


Figure 4.4: Dispersion relations of cySPP modes propagating on a metal cylinder. While the axially symmetric $m = 0$ mode propagates for arbitrary values of R , all the higher modes experience an increasingly greater cutoff radius. For large values of R all the modes approach the value $\sqrt{\epsilon_d \epsilon_m / (\epsilon_d + \epsilon_m)}$ (black dashed line), while at the cutoff radius the propagation index is $\sqrt{\epsilon_d}$ (grey dashed line).

4.3.1 Propagation in hollow waveguides

The propagation constants of the cySPP propagating in a hollow metallic waveguide is obtained by exchanging the values of the dielectric constants in Expression (4.1). For the mode $m = 0$ the same approximation proposed in the previous subsection can be performed, which gives as result:

$$\xi \log \xi = \eta, \quad \eta = \frac{\tilde{\gamma}^2 \epsilon_m}{\epsilon_d}. \quad (4.9)$$

In this case $\eta < -1$ and the propagation condition (4.6) is not satisfied. Thus, the mode $m = 0$ has no propagating solution for arbitrarily small cylinder radii. This fact is valid also for higher order modes, as reported in Figure 4.5. As it can be observed, it exists a manifold of solutions for each plasmonic mode repeating with a characteristic periodicity approaching a common value for increasing R . The reason is that since all the solutions lay in the region $n_{\text{eff}} < \epsilon_d$, the variable v is imaginary and therefore the modified Bessel function of the first kind turns into an ordinary Bessel function, whose oscillatory behavior gives rise to a multiplicity of solutions.

Although Figure 4.5 indicates that no cySPP can be focused at arbitrary low waveguide radius, the situation changes when considering the imaginary part of the metal dielectric function. In this case the propagation index n_{eff} becomes a complex number, thus a clear distinction between propagating and evanescent modes is no longer possible. In

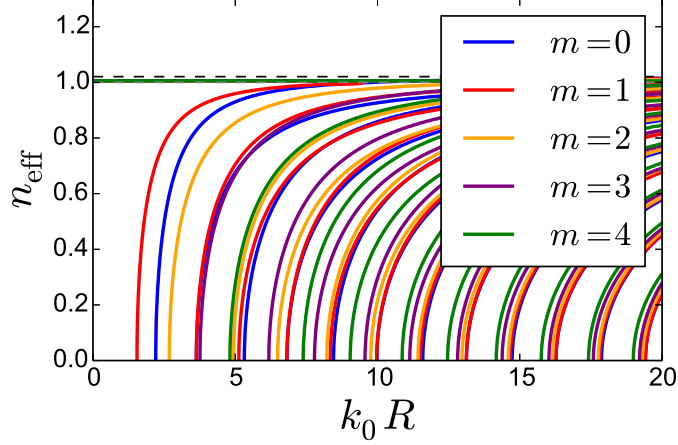


Figure 4.5: Dispersion relation of cySPP propagating in a hollow metal cylinder. All the modes experience a cutoff radius $R_{\text{cutoff},mn}$. For large values of R all the modes approach the value $\sqrt{\epsilon_d \epsilon_m / (\epsilon_d + \epsilon_m)}$ (black dashed line). For $n_{\text{eff}} < \sqrt{\epsilon_d}$, each mode m shows a manifold of solutions, arising from the oscillatory behavior of the Bessel function $I_m(iv) = J_m(v)$.

Ref. [NH94] was observed that the cutoff region in the ideal case is resolved by a return to propagation for cylinder radii of nanometric size. In any case, from Figure 4.5 it can be inferred that the cutoff radius for the $m = 1$ mode is $R_{\text{cutoff},1} \simeq 200$ nm.

In the present case of study, the linear polarization of the source pulse required for HHG breaks the otherwise axial symmetry of the cylinder waveguide. Thus, the cySPP excited by a linearly polarized NIR pulse must show an opposite charge distribution at its maxima, a condition which is fulfilled only by the $m = 1$ mode.

It is interesting to comment on the matching condition of the NIR pulse with the $m = 1$ mode. In Figure 4.6 an equivalent of the dispersion relation diagram for a flat surface (see Figure 3.1) obtained for an aluminum hollow waveguide is reported. Differently from the flat surface case, the dispersion relation of a cySPP in a hollow waveguide crosses the light line for all the waveguide radii reported. This ensures the plasmon wavevector phase matching with the source NIR pulse wavevector without particular requirements on the coupling setup.

4.4 Geometry of the tapered waveguide

Numerical optimization of the tapered waveguide was performed by comparing the field enhancement obtained in different geometries and NIR pulse durations. The plasmonic field generated by the driver NIR pulse was computed with MEEP [Osk+10], an open source C++ library implementing the finite-difference time-domain (FDTD) method [Taf05].

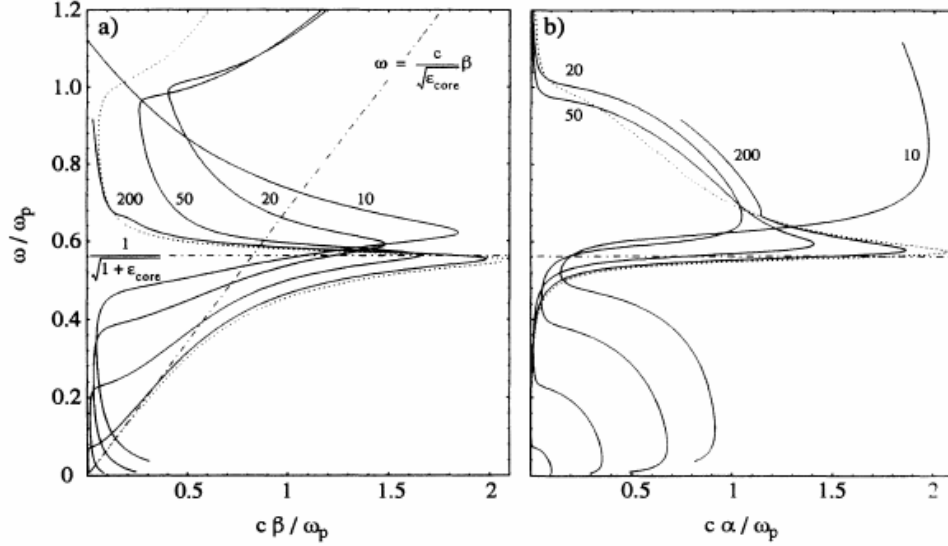


Figure 4.6: Dispersion relation for cySPP of order $m = 1$ propagating in a hollow cylinder of dielectric constant given by $\epsilon(\omega) = 1 - \frac{\omega_p^2}{\omega(\omega + i\gamma)}$. The plasmon frequency is plotted versus $\beta = \text{Re}\{n_{\text{eff}}\} k_0$ (a) and $\alpha = \text{Im}\{n_{\text{eff}}\} k_0$ (b). The values of the parameters are $\omega_p = 15.5$ eV, $\gamma = 0.6$ eV and $\epsilon_d = 2.16$. Also shown are the light line (dot-dashed) and the flat surface plasmon line (dotted). The values assumed for the waveguide radius are given in figure. Figure reproduced from [NH94].

It was found that an elliptic cross section at fixed axis ratio provides a higher field enhancement at the waveguide tip, which is related to the deeper penetration of the plasmonic field toward the tip of the waveguide. The geometry is shown in figure 4.7. The ratio between the minor axis b and major axis a of the ellipse is $b/a = 0.25$. Similar to reference [Par+11], we chose for our simulations a 9 μm long silver cone and opening angles of 14 and 3.5 degrees along the major (x) and minor (y) axis of the ellipse, respectively. These parameters uniquely define the waveguide geometry. We assume a 5 fs FWHM Gaussian driver pulse at wavelength $\lambda_0 = 800$ nm, beam waist $w_0 = 2.5$ μm , and focused intensity $I_0 \approx 4 \times 10^{11}$ W/cm². The focus is at the large opening of the tapered waveguide (see Fig. 4.8). One finds that the coupling is rather robust with respect to variations of the focus position by ± 1 μm , causing intensity changes of less than 5% in peak plasmon intensity. An enhancement factor of ~ 500 in peak intensity is found for an eccentricity value of $\epsilon = 0.25$. For $\epsilon = 0.5$, as used in Ref. [Par+11], the enhancement is reduced by about a factor 3. A similar dependence on ellipticity was reported in [Cho+12], where pulse durations between 4 and 10 fs were investigated.

Since the peak field is reached at the surface, any surface roughness could introduce modifications of the exact maxima. This however does not invalidate the analysis, since harmonics produced in proximity of the waveguide surface will be absorbed in the metal,

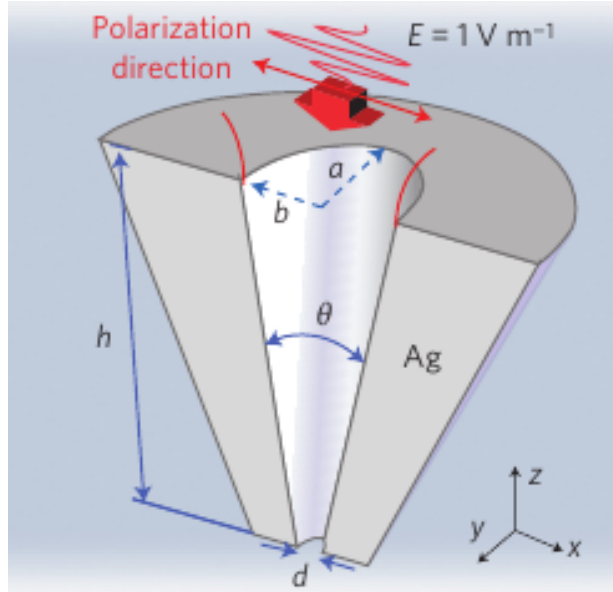


Figure 4.7: Geometry of the tapered nanoplasmonic waveguide. The laser polarization is along the minor axis of the waveguide cross-section. The length of the waveguide is $9 \mu\text{m}$, the major axis at the larger opening is $a = 2.2 \mu\text{m}$, the size of the opening at the waveguide apex along the minor axis is $d = 25 \text{ nm}$. The eccentricity of the cross-section is $b/a = 0.25$. Figure reproduced from [Par+11].

while the dominant contribution coming from the central region is less subject to sub-wavelength structures of the waveguide.

Further optimization of the cone geometry allows for even weaker driver pulses, keeping in mind that ultimately the field inside the waveguide is limited by electric breakdown. Ref. [Par+11] claims that silver can sustain much higher fields than expected, most likely because of the few femtosecond duration of the employed pulse [Ple+05]. In our work we neglect the incoherent radiation emitted by photo-ionized silver atoms.

4.5 Waveguiding of XUV pulses by the waveguide

In MEEP [Osk+10], the dielectric function must be of the form

$$\epsilon(\omega) = \epsilon_{\infty} - \frac{\omega_p^2}{\omega(\omega - i\gamma_0)} + \sum_n \frac{f_n \omega_n^2}{\omega_n^2 - \omega^2 + i\omega\gamma_n} \quad (4.10)$$

for algorithmic reasons. In the visible region, the parameters which best fit the dielectric constant of silver are taken from Ref. [Rak+98a]. As for the XUV range, which is relevant for the HHG process, the Drude-Lorentzian modeling reproduces the frequency dependency of the dielectric function poorly. It was given preference to an accurate fit of the imaginary

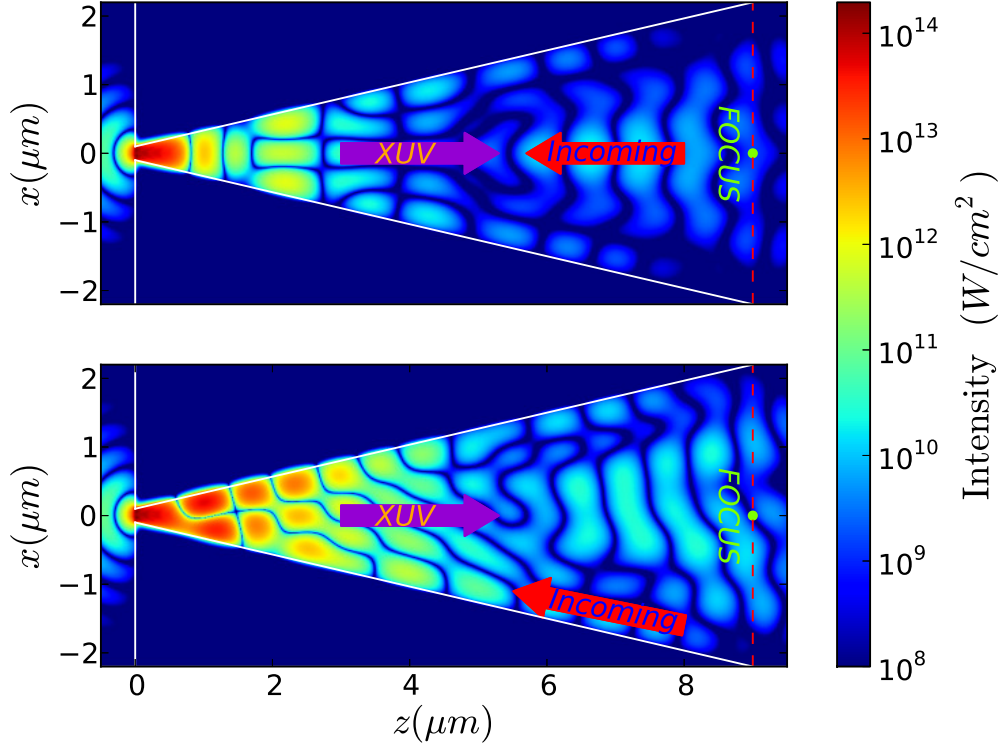


Figure 4.8: Plasmonic field distribution in the xz -plane at peak plasmon field of $2 \times 10^{14} \text{W/cm}^2$. The calculation is performed with the Finite-Difference Time-Domain (FDTD) method. The upper panel shows the normal incidence case, the lower the oblique case. Polarization is in y -direction perpendicular to the plane and independent of the incidence angle, which in the lower panel is of 7 degrees in the zx -plane parallel to the inner cone surface. A remarkable property of PEAX is that the XUV harmonic beam is emitted in the direction of the cone axis for any incidence angle. This is due to the symmetry of the $m = 1$ mode, which is excited irrespective of the angle of incidence. Figure reproduced from Ref. [LKS13].

part of the dielectric response against the data taken from [HGD93], since it was found that the real part of the dielectric response has little influence on the propagation of the harmonic radiation inside the waveguide. By changing the real part of the fitted dielectric function by a factor of 4 (cf. Fig. 4.9), a change in the signal intensity by less than 15% is observed, while the time-structure remains unaffected, as shown in Figure 4.10.

The high harmonics were let propagate in the same FDTD code used for the plasmonic response, but with a sampling spacing of 2.5 nm, well below the characteristic wavelength of 800 nm of the driver plasmon in the waveguide and below the relevant harmonic wavelength

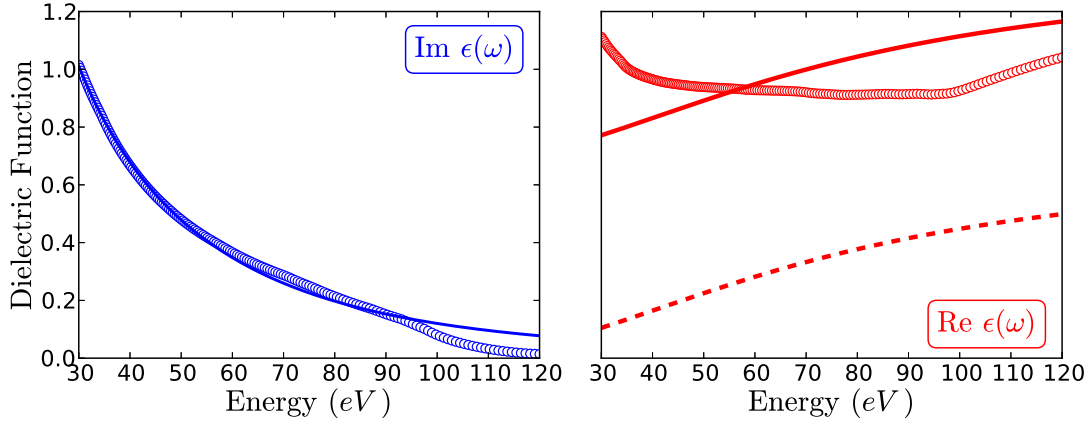


Figure 4.9: Dielectric functions used for the simulation of high harmonic propagation. The imaginary part (left, blue circles) is well approximated by a Lorentzian shape (blue line). The fit (right, red line) of the real values (circles) is comparatively poor. The deliberately bad fit (dashed red line) was used for checking the robustness of the simulation. Experimental data from [HGD93].

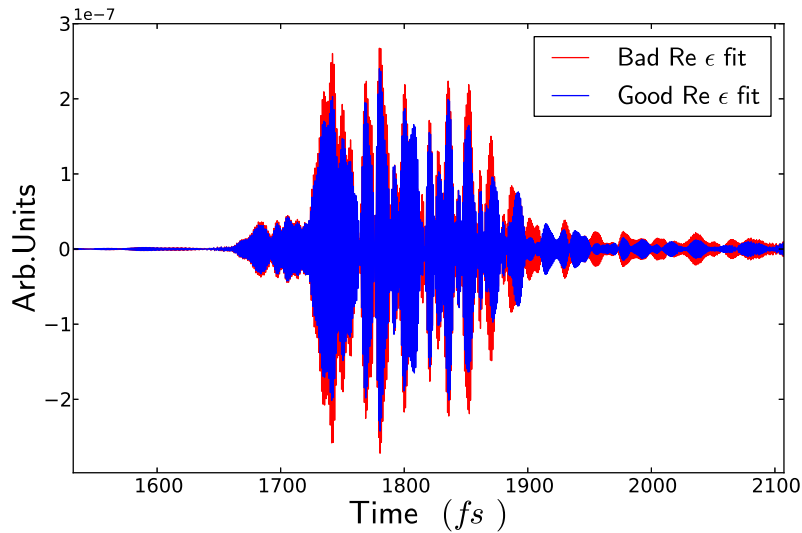


Figure 4.10: Comparison of the electric field amplitudes measured far from the waveguide, in the backwards direction, simulated using different fit of the real part of the dielectric function for the XUV range. In both cases the same Zr filter for the removal of the low harmonics was employed.

of ~ 27 nm. The dipole responses of the gas atoms were calculated by solving the time-dependent Schrödinger equation with the irECS method [Scr10] using a single-electron

model with the ionization potential of Argon. In these calculations fluorescence is not included, which would contribute incoherently to XUV radiation. The harmonic generation process is strongly dependent on the driver pulse intensity: from 2×10^{14} W/cm² to 1×10^{14} W/cm² the harmonic yield near the cutoff photon energy of ~ 60 eV drops by ~ 3 orders of magnitude. For this reason the region of calculation of the atomic dipole responses was limited to the volume where the total field intensity exceeds 10^{14} W/cm², corresponding to an active volume $V_a = \Delta x \times \Delta y \times \Delta z \approx 240 \times 60 \times 500$ nm³

The harmonic emission occurs also for coupling of the driver NIR pulse over a range of incidence angles. For $\theta = 7^\circ$ with respect to the polarization (y) axis, the plasmonic enhancement is reduced by a factor 4, which can be compensated by an increase of the input field intensity.

The far field distribution of the harmonic radiation was computed by means of the Kirchhoff integral using the plasmonic field at the surface $z = 2.5$ μ m from the smaller waveguide aperture as source. The Kirchhoff formula for monochromatic waves is

$$E(\xi, k) = \int_S dS \left[E(S) \frac{\partial}{\partial n} \left(\frac{e^{i\mathbf{k}\cdot\mathbf{s}}}{|\mathbf{s}|} \right) - \frac{e^{i\mathbf{k}\cdot\mathbf{s}}}{|\mathbf{s}|} \frac{\partial E}{\partial n} \right], \quad (4.11)$$

where $S(x, y)$ is the 2D source surface taken from the FDTD simulation, ξ is the observation point and $\mathbf{s} = \xi - \mathbf{x}$, with $x \in S$. The validity of this procedure was verified by comparing the guiding effect of a wedge-shaped waveguide on the harmonic propagation, where the translational symmetry reduces the problem to 2 dimensions. It was found that beyond the cutting distance of 2.5 μ m further guiding of the XUV radiation is very small. On the other hand, a comparison with the “free” propagation, where the waveguide has been artificially removed, shows that the XUV intensity is enhanced by a factor 4, as shown in Figure 4.11. A Zirconium-like filter was used to remove only the fundamental and lower harmonics from the generated harmonic spectrum. Figure 4.12 shows the angular distribution of harmonic emission out of the wide side of the cone for a range of harmonic frequencies at oblique driver incidence.

The incident intensity was adjusted to obtain a maximum plasmonic field near the waveguide tip of 2×10^{14} W/cm². As can be clearly observed in Figure 4.12, the spatial divergence decreases with increasing photon energy, where the divergence is defined as the full-width half maximum (FWHM) in the XUV intensity. The normal incidence case with equally adjusted peak intensity gives results similar to oblique incidence. The reason is to be found in the single mode nature of the plasmonic field, whose topology in its maximal value region is insensitive to the angle of incidence.

An analysis of the attosecond beam propagation through the waveguide smaller aperture shows that in this case the funnel causes diffraction rather than collimation. The last point could be tested in the full three dimensional case by using the electric field at the waveguide smaller aperture as source surface for the Kirchhoff diffraction integral. The spatial profile of the harmonics is shown in Figure 4.13.

Although the XUV power is comparable in forward and backward emission, the beam

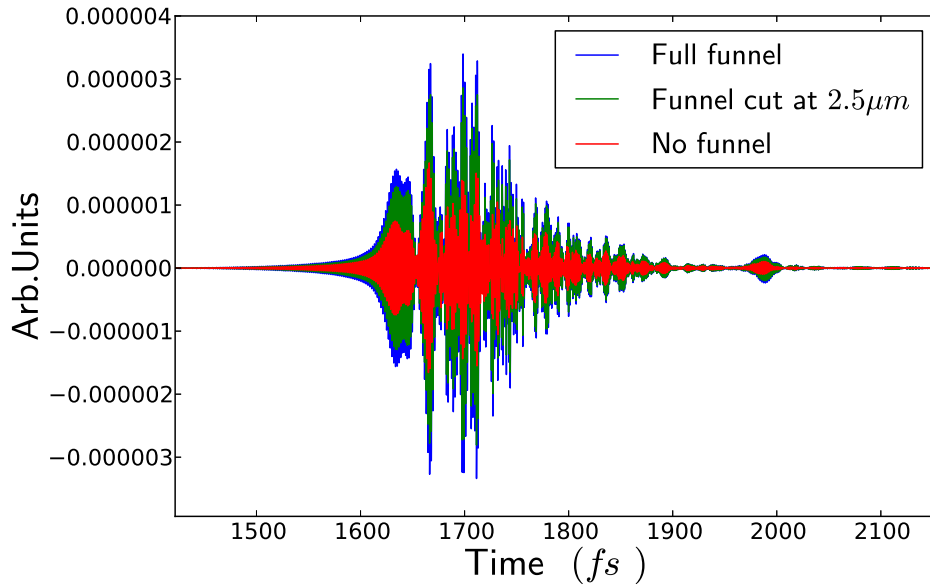


Figure 4.11: Comparison of the electric field amplitudes measured far from the waveguide larger aperture in the backwards direction, for different wave-guiding conditions. In all cases the same Zr filter was employed.

divergence is 35° in y -direction, such that the resulting harmonic beam is hard to focus for experimental use. In a simulation of the XUV harmonic propagation without the waveguide, forward and backward beams are nearly identical, demonstrating that diffraction and collimation is due to the waveguide presence, and not to the plasmonic field topology induced by the waveguide shape.

4.6 PEAX temporal characterization

Since the active volume V_a of HHG is smaller than the driving laser wavelength, the phase matching of the harmonics is not an issue. Geometrically induced phase shifts are naturally included in the simulation. With negligible dephasing between driver and harmonics across V_a , harmonic intensities grow quadratically with the gas density. The atomic dispersion is also expected to remain small, and, if needed, may be controlled by choosing a target gas suitable for a given harmonic wavelength.

In Table 4.1 the parameters of the XUV-AS pulses are obtained at gas pressure of 0.3 bar (density $7.8 \cdot 10^{18} \text{ cm}^{-3}$), a value typically used in standard HHG. To check the influence of the atomic species on the spectrum of the HH radiation produced by the plasmonic field, Argon, Neon and Xenon were considered.

Details of the spectral structures for the different atomic species are reported in Figure 4.14. Despite the peculiarity of the exciting inhomogeneous plasmonic field, the spectra in

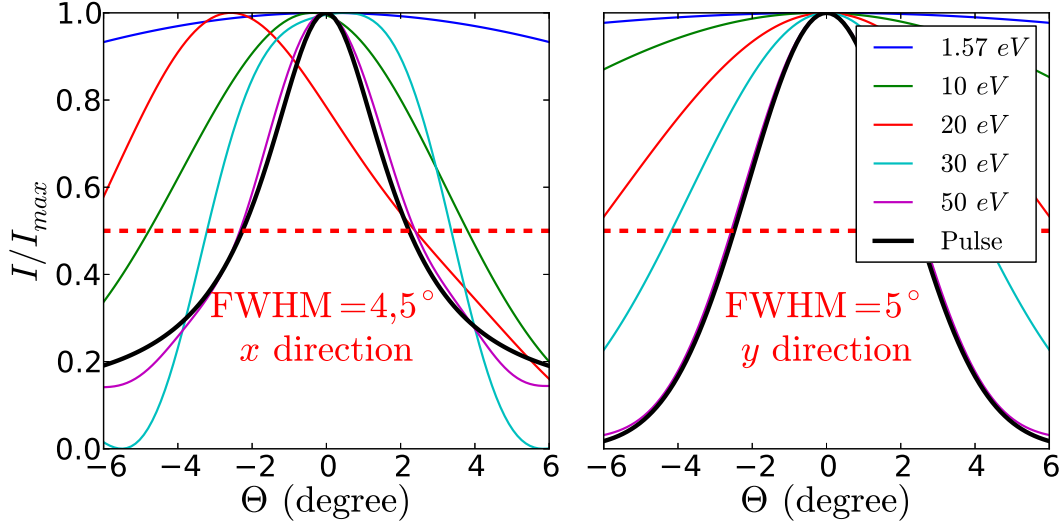


Figure 4.12: Angular distribution of harmonic radiation for the photon energies reported in the inset legend. At oblique incidence with driver polarization along y , the x -distribution of the harmonics is asymmetric (left panel), while it remains symmetric in the y -direction (right panel). The spatial profiles of the harmonics are taken in the far field, at 1 mm distance from the waveguide large opening in the backward plasmon propagation direction. The black line is the sum of all the harmonics above 45 eV, and therefore gives a measure of the AS pulse collimation angle. Taking as reference the FWHM of the XUV pulse intensity, the beam divergence is about 5° in both x - and y -directions. Thus, the projection of the AS pulse on the plane orthogonal to the waveguide axis is a circle centered on the axis, despite the elliptic cross-section of the waveguide and the oblique incidence of the driver NIR pulse. Figure reproduced from [LKS13].

Table 4.1: Harmonic beam characteristics for oblique incidence PEAX and a standard harmonic source using a Gaussian beam (see text for parameters). Yields and photon fluxes are integrated over the beam divergence angles.

Gas	PEAX			Gauss
	Ne	Ar	Xe	Ar
ω_γ (eV)	53	45	45	45
Δt (as)	250	300	250	300
Rep. Rate		80 MHz		3 kHz
γ/pulse	$0.94 \cdot 10^{-3}$	$6.7 \cdot 10^{-3}$	$0.94 \cdot 10^{-3}$	$3 \cdot 10^4$
γ/s	$7.6 \cdot 10^4$	$5.4 \cdot 10^5$	$6.5 \cdot 10^4$	$9 \cdot 10^7$
Divergence		5°		1°
V_a (μm^3)		$\sim 4 \times 10^{-3}$		~ 16

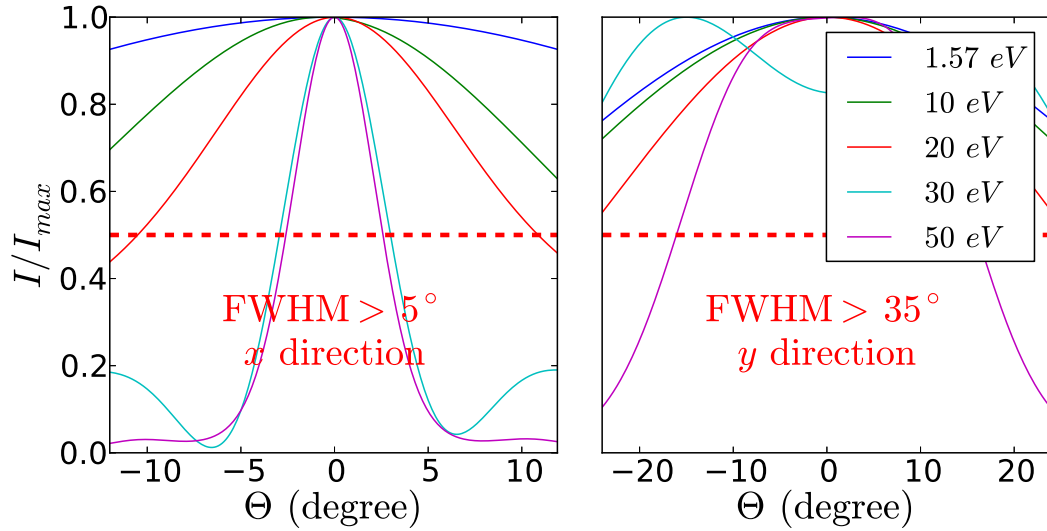


Figure 4.13: Angular distribution of different energy harmonic radiation propagating through the waveguide tip. While the spatial profile in the x -direction resembles the case of backward propagation, the harmonic profile in the y -direction is the result of severe diffraction by the minor axis of the waveguide cross-section, resulting in a beam divergence larger than 35° .

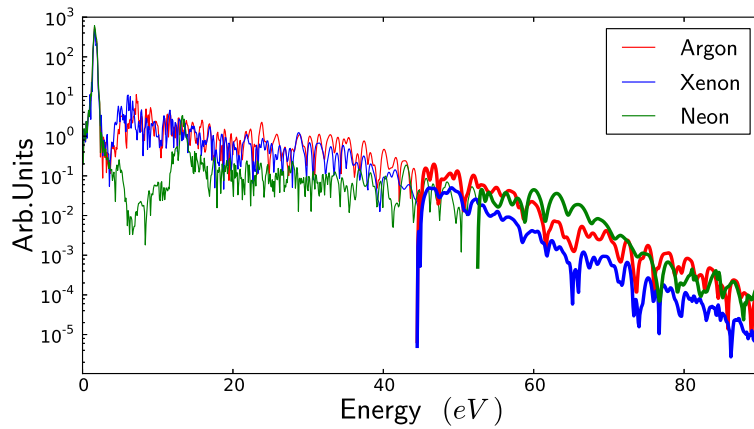


Figure 4.14: Spectrum of the harmonic radiation produced by different atomic species. The thicker lines show the part of the spectrum which must be kept to produce an isolated AS pulse with maximum photon yield.

Figure 4.14 closely resemble the single-atom responses. For the driver intensity of 2×10^{14} W/cm², Argon shows a cutoff similar to Neon, but an order of magnitude larger spectral intensity, while Neon has a higher cutoff and lower spectral intensity. These characteristics reduce the achievable high harmonic yield for both Neon and Xenon, a feature which affects

in the same way the PEAX and the standard gas harmonic source.

The PEAX harmonics above 45 eV form an isolated AS pulse. Because of the rapid decay of the spectral intensity with harmonic energy, the AS pulse central frequency nearly coincides with the lower cutoff frequency of the harmonics. The pulse contrast, defined as the energy ratio between the main pulse and any satellite pulses, is satisfactory with 85% of the energy in the main pulse.

4.7 PEAX spatial properties

The AS pulse emerging from the backwards propagation direction has a perfectly spherical wavefront (cf. Fig. 4.15). The deviation from the spherical shape remains below the central XUV wavelength over the whole front. This can be ascribed to the very small and well-defined generation volume, which is a consequence of the excitation of the single plasmonic mode $m = 1$.

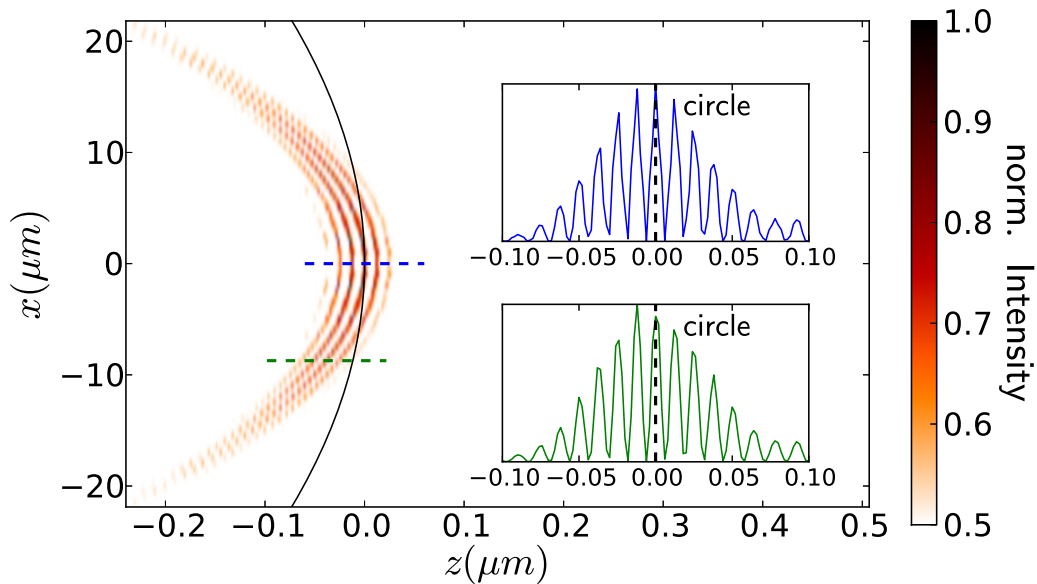


Figure 4.15: Spatial shape of the XUV AS pulse wavefront. The color map shows the part exceeding half the peak intensity. The black line indicates the position of a circle having as center the waveguide tip, and radius the distance of observation. The inset figures show sections of the wavefront taken for two different radii. The dashed lines show the position of the cuts and the spherical front, in the color map and in the insets, respectively. Figure reproduced from [LKS13].

Differently from standard gas harmonics, this attosecond source distinguishes itself for the clean wavefront, which allows to focus the pulse without compromising its time

structure. Moreover, the AS pulse is emitted on the cone axis, while the reflected driver and lower harmonics are emitted into wider angles with a modulated intensity profile (cf. Fig. 4.12). This is particularly useful because it permits a simple geometric separation of the incident driver pulse from the harmonic pulse. The remaining on-axis reflected driver pulse and low harmonics can be filtered out by standard multilayer mirrors. Furthermore, a shorter driver pulse of 4 fs and equal intensity brings no extra advantage: the AS pulse duration and divergence remain the same, while the pulse intensity is $\sim 20\%$ less. Similarly, the pulse parameters are not improved by exciting the cylinder plasmon at normal incidence, because the higher field enhancement is compensated by a reduction of the active volume V_a , as it can be observed in Figure 4.8.

4.8 Comparison with standard gas harmonics

In Table 4.1, the rightmost column contains the pulse parameters for a standard harmonic source, simulated with our numerical techniques for benchmarking the PEAX. A Gaussian beam of 4 fs FWHM pulse duration and tight focus of $w_0 = 1 \mu\text{m}$ in a gas jet with peak intensity equal to the peak plasmonic intensity of $2 \times 10^{14} \text{ W/cm}^2$ was used. The HHG active volume, given by the prolate ellipsoid with w_0 as minor axis and the Rayleigh length $z_r = 3.9 \mu\text{m}$ as major axis, is three orders of magnitude bigger than in the PEAX. In the present configuration, the PEAX source produces slightly longer pulses with larger beam divergence. For photon energies of $\sim 45 \text{ eV}$ and at the given gas pressure, the photon yield per shot is almost 7 orders of magnitude larger compared to PEAX. This corresponds to a difference of a bit more than 3 orders of magnitude in field strength, which is consistent with the ratio of the active volumes of the two sources.

Since no amplification chain is required for a PEAX source, the repetition rate remains that of the oscillator, near 100 MHz, reducing the difference in the photon fluxes with the standard source to less than 500. With an active volume of sub-wavelength dimension, the gas density can be increased by many orders of magnitude before phase matching and coherence problems arise. Assuming tenfold pressure for the PEAX, photon flux could be boosted by 2 orders of magnitude, basically equaling the standard harmonic source performances. Moreover, a further increase of the XUV pulse power could be achieved by using a rasterized arrangement of many PEAX sources as in Ref. [Par+13], which is possible thanks to the high quality of the attosecond pulse spatial profile. In such an arrangement, interference between the emission from different tapered waveguides could be utilized for phase-matching.

On the other hand, the volumes for coherent gas harmonic generation in the standard configuration, and consequently the power of the AS pulse, can be significantly larger than what assumed in the previous comparisons. It is demonstrated (see Ref. [Gou+08]) that phase matching can be maintained over about 1 mm propagation length at a beam cross section of few hundred μm^2 , giving an active volume, and thus an output power of about 3-5 orders of magnitude larger than in the PEAX. In table 4.2 the experimental parameters

given in Ref. [Gou+08] are compared with the simulated values of the PEAX.

Table 4.2: Attosecond beam parameters for state-of-the-art standard harmonic generation [Gou+08], compared to the parameters used for benchmarking the PEAX source..

	Experimental	Theoretical
Atom	Neon	Argon
I_0 (W/cm ²)	5×10^{14}	2×10^{14}
ω_γ (eV)	80	45
Δt (as)	100	250
Rep- Rate	3 kHz	3 kHz
γ/s	10^{11}	9×10^7
Power P_{XUV}	$\sim 1 \mu\text{W}$	0.65 nW
V_a	$\sim 10^{-1} \text{ mm}^3$	$16 \mu\text{m}^3$

This last consideration can be generalized to all the proposed high harmonic generation schemes based on plasmonic enhancement: since the required intensity is achieved in an active volume of sub-wavelength scale, the amount of obtainable photon fluxes is limited compared to the much larger diameter and phase matching length which can be realized in a standard generation scheme.

4.9 Discussion and experimental issues

We illustrated the advantages of PEAX sources in term of beam collimation, pulse front quality, and high repetition rate, which can be used for spatio-time-resolved surface spectroscopy [Sto+07].

From an experimental point of view, PEAX sources should be quite feasible, since no pulse amplification chain is needed. Moreover, the intrinsic geometrical separation of higher from lower harmonics can be exploited to simplify the experimental setup. The main difficulty is the rather low yield to be expected from a PEAX source. Also, the high harmonic generation for the bow-tie shaped nano-devices reported in Ref. [Kim+08], has not so far seen independent verification.

A first severe criticism was formulated in 2012, when in Ref. [Siv+12] it was shown that the observed XUV emission was not a coherent process, but rather a multi-photon atomic line emission (ALE) process. The main criticism was related to the conversion efficiency of the laser power into harmonics: in [Kim+08] it is reported to be of the same order of magnitude as in standard harmonic generation, where however the conversion volume is 8 orders of magnitude bigger. It was argued that the ratio between the conversion efficiency of nano-HHG and gas HHG should scale as:

$$\frac{C_{\text{nano}}}{C_{\text{conv}}} = \frac{R_{\text{nano}}}{R_{\text{conv}}} \left(\frac{V_{\text{nano}}}{V_{\text{conv}}} \right)^2 \left(\frac{F_{\text{nano}}}{F_{\text{conv}}} \right)^2 \sim 10^{-8}. \quad (4.12)$$

where $R_{\text{nano}}/R_{\text{conv}} = 10^5$ is the repetition rate ratio, $V_{\text{nano}}/V_{\text{conv}} = 10^{-8}$ is the volume ratio, and the phase matching factor $F_{\text{conv}}^2 = 10^{-3}$ is used, which in the plasmonic case is set to $F_{\text{nano}}^2 = 1$.

In the response in Ref. [Kim+12], it was agreed that bow-ties HHG is not a viable technique, and the focus should be shifted to the tapered waveguide technique discussed in this Chapter, where the enhancement volume is 2 orders of magnitude bigger than in the bow-ties case.

Following a reasoning similar to what leads to Eq. (4.12), in Ref. [Ras13] it was further shown that by comparing the conversion efficiencies in Refs. [Kim+08]-[Par+11] with those achievable in the cavity-enhancement HHG framework [Cin+12], it is possible to extrapolate the absolute power of the high harmonic radiation.

In table 4.1 the PEAX characterization obtained with Xenon, which is used in Ref. [Ras13], and Argon, which is used in our work [LKS13], are compared. The comparison of the PEAX characterization performed with Xenon to what obtained in Ref. [Ras13] shows that the values are correct within one order of magnitude. The difference is probably due to the small guiding effect provided by the waveguide in the backward direction. What is puzzling is that the theoretical prediction contained in this Chapter and the one in Ref. [Ras13] are 5 orders of magnitude smaller than what extrapolated for the experimental results reported in Ref. [Par+11]. As a final remark, during the review of Ref. [LKS13], in Ref. [Siv+13] it was established that in the bow-ties case the HHG signal is a factor 10^{-3} weaker than the signal from multi-photon ALE.

Since the bow-ties plasmonic device and the nanoplasmonic tapered waveguides investigated in this work are closely related, the perspectives of this last technique are not very encouraging at the moment. However, the higher enhancement volume with respect to bow-ties structures and the guiding effect in the backward direction may narrow the gap in terms of power with standard harmonic generation. If we add to this the excellent spatial properties, the weak dependence on the incidence angle in the funnel, and the absence of any amplification chain, the PEAX sources can compete with the standard ones in term of practicality and affordability.

5

Attosecond Photocopy of Surface Excitations

This Chapter is largely based on Ref. [Lup+14]. From using SPPs for AS pulse generation the attention is now shifted to a scheme for probing the SPP dynamics by mean of AS pulses. Surface plasmons are widely used in many cross-disciplinary fields for their properties of light confinement in the vicinity of metallic supports. In this context, the nanoplasmonic branch is a promising candidate for the development of plasmonic based all-optical processors, since the field confinement property can combine the high operational speed of photonics (PHz scale) with the miniaturization provided by electronics (nm scale) [Ozb06]. In this sense, it is interesting to investigate the temporal transient properties of the surface electron excitation. Although the plasmon lifetime can be deduced from the plasmonic resonance width observable in the reflection or transmission spectrum, the formation process of the resonant oscillation cannot be studied in the framework of frequency analysis.

In this Chapter an experimental proposal based on the attosecond streak camera (ASC) [Kie+04] is presented, which aims to image the transient dynamics of a plasmonic mode. The ASC technique was already successfully applied to solid surfaces in [Cav+07] for the measurement of electron transport times in tungsten. The attosecond streak camera is a two-color pump-probe scheme, where a weak XUV-AS pulse ionizes electrons from the solid, and a collinear, few-cycle ($\sim 5 fs$ FWHM) NIR pulse serves as the probe, which accelerates the XUV photo-electrons after their escape from the solid.

The excitation of two counter-propagating SPPs on a grating structure is considered. A time-delay controlled arrangement of NIR and XUV beams is used to excite the SPPs and to emit photoelectrons which move in the plasmonic field. The temporal structure of the plasmonic field is reflected in the photoelectron spectrum. In principle it is possible to spatially separate the pump and the probe beams, allowing the imaging of plasmonic modes in different surface regions, thus providing spatio-temporal information. To distinguish this arrangement from standard attosecond streaking experiments, this setup was named “Attosecond Photocopy”.

5.1 Experimental setup

Isolated AS pulses are produced from high harmonic radiation emitted by noble gases irradiated with few-cycle carrier envelope phase (CEP) stabilized NIR laser pulses [Hen+01; Cav+07; Cor93; AD04]. The generated high harmonic radiation co-propagates with the NIR pulse. The pulses are focused onto the grating structure with a two part mirror composed of a XUV multilayer mirror in the inner part, designed to reflect only the highest part of the harmonic spectrum, and a broadband NIR mirror in the outer part. This arrangement allows to produce an isolated AS pulse, timed with a precision of $\lesssim 10$ as to the NIR pulse.

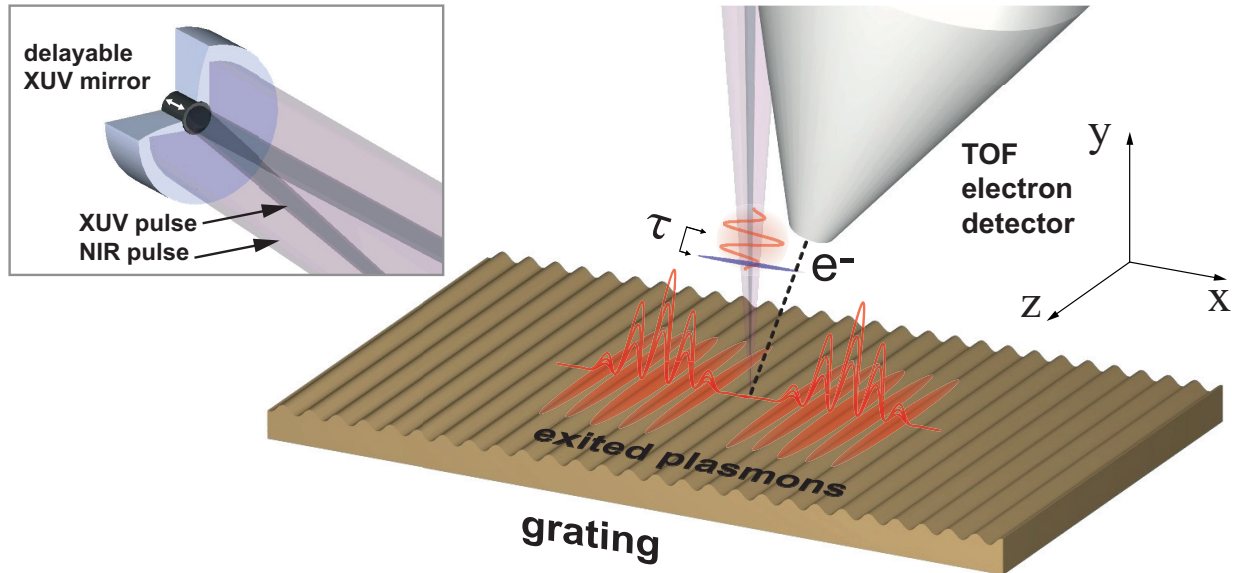


Figure 5.1: Proposed experimental arrangement for performing attosecond photocopy of surface plasmon excitations. A cloud of photoelectrons ionized by the XUV AS pulse is accelerated in the SPP fields, which are in turn excited by a short NIR pulse. Attosecond precise control of the time delay between the NIR and XUV pulses enables the determination of the SPP transient properties. Figure reproduced from [Lup+14].

The experimental setup is illustrated in Figure 5.1. The NIR and XUV beams propagate along the direction orthogonal to the grating plane, which is referred to as y -direction, with polarizations along the grating grooves, in the x -direction. In the NIR focus two SPPs are excited, counter-propagating along x with polarizations along y . Although at normal incidence only one of the two plasmonic branches, the bright mode [Bar+96], is visible with plane waves, the tight focusing of the NIR pulse allows the coupling with the second branch, the “dark” mode (cf. Figure 5.8).

The photoelectrons emitted by the XUV-AS pulse are then collected by a detector in the y -direction. Following [Cav+07], the resulting *spectrogram* of final momenta recorded

as a function of the time delay between NIR and XUV pulses, is a convolution of the photoemission process with electron acceleration by the surface fields. Depending on the time delay between the driving NIR pulse and the XUV-AS pulse, the plasmonic field recorded by the emitted photoelectrons differs in amplitude and phase, leading to a modulation of the kinetic energy distribution in the photoscopic spectrogram. It will be shown in Sec. 5.2 that the plasmonic field contribution is given only at the time and position of the photoelectron emission.

With this technique, it is possible to resolve in the time domain the energy gap between dark and bright plasmonic modes, which appears in the spectrogram as a “transition” from the bright ω_b to the dark ω_d mode frequencies. This feature is measurable in the proposed setup thanks to the attosecond resolution.

In the following the properties of the photoscopic spectrogram are studied using a classical analytical model and its predictions are compared with numerical solutions of the electron dynamics in the plasmonic field together with a Monte Carlo simulation of the photoemission process. In the end, it is shown how the plasmonic field at the surface can be recovered from the spectrogram analysis.

5.2 Theory of attosecond photocopy

Typical streaking setups in attosecond metrology use atoms or molecules, which can be considered point-like electron sources with respect to the laser wavelength. Hence it is possible to use the dipole approximation: $\mathbf{A}(\mathbf{r}, t) \simeq \mathbf{A}(t)$. The canonical momentum along the pulse polarization is conserved, $\mathbf{P}(t) = \mathbf{P}_i$, which can be rewritten as $\mathbf{p}(t) + \frac{e}{c}\mathbf{A}(t) = \mathbf{p}_i + \frac{e}{c}\mathbf{A}(t_i)$, where $|\mathbf{p}_i| = \sqrt{2m(E_{xuv} - W_f)}$ is the initial momentum of the electron released at time t_i .

As $A(t \rightarrow \infty) = 0$, the measured final momentum is

$$\mathbf{p}_f = \mathbf{p}_i + \mathbf{a}(t_i), \quad (5.1)$$

where the constants were absorbed into the new quantity $\mathbf{a} = \frac{e}{c}\mathbf{A}$.

The spectral width of the XUV-AS pulse is reflected in the initial electron distribution $n_e = n_e(\mathbf{p}_i, t_i)$. For simplicity Gaussian distributions in time and momentum are assumed, centered around time t_0 and momentum \mathbf{p}_0 , respectively, with t_0 the time of XUV peak intensity on the target. The time-integrated final momentum distribution is

$$\sigma(\mathbf{p}_f) = \int_{-\infty}^{\infty} dt_i n_e(\mathbf{p}_i, t_i) = \int_{-\infty}^{\infty} dt_i n_e(\mathbf{p}_f - \mathbf{a}(t_i), t_i), \quad (5.2)$$

where Eq. (5.1) was inserted into the initial electron distribution dependence over \mathbf{p}_i . The

spectrogram at varying time delay τ becomes

$$\sigma(\mathbf{p}_f, \tau) = \int_{-\infty}^{\infty} dt_i n_e(\mathbf{p}_f - \mathbf{a}(t_i), t_i - \tau). \quad (5.3)$$

From this, the NIR pulse can be reconstructed via a Center-Of-Energy (COE) analysis of the average momentum of the streaking spectrogram:

$$\langle \mathbf{p} \rangle(\tau) = \frac{\int_{-\infty}^{\infty} d\mathbf{p}_f \mathbf{p}_f \sigma(\mathbf{p}_f, \tau)}{\int_{-\infty}^{\infty} d\mathbf{p}_f \sigma(\mathbf{p}_f, \tau)}. \quad (5.4)$$

If the detector collects only the photoelectrons emitted along the laser polarization, the vector quantities in Eq. (5.4) become scalar. Taking $n_e(p_i, t_i) = N(p_0, dp) \times N(t_0, dt)$ as initial distribution, where $N(a, b)$ is a Gaussian distribution of mean value a and variance b , the integral gives

$$\begin{aligned} \langle \mathbf{p} \rangle(\tau) &= \int_{-\infty}^{\infty} dt_i e^{-\frac{(t_i - t_0 + \tau)^2}{2\Delta t_{\text{xuv}}^2}} \int_{-\infty}^{\infty} dp p e^{-\frac{(p - p_0 - \mathbf{a}_{\parallel}(t_i))^2}{2\sigma_p^2}} \\ &= \int_{-\infty}^{\infty} dt_i (p_0 - \mathbf{a}_{\parallel}(t_i)) e^{-\frac{(t_i - t_0 + \tau)^2}{2\Delta t_{\text{xuv}}^2}} \underset{\Delta t_{\text{xuv}} \ll 2\pi/\omega_L}{\simeq} p_0 - \mathbf{a}_{\parallel}(t_0 - \tau), \end{aligned} \quad (5.5)$$

where it was defined $p = \mathbf{p}_{f,\parallel}$. From Eq. (5.5) is clear that averaging the streaking spectrogram yields the vector potential of the NIR pulse. The vector potential reconstruction is possible only if Δt_{xuv} is much smaller than the optical period of the NIR, which is guaranteed by the ultrashort duration of the AS pulse. Thus, the attosecond streaking technique works as a mapping of time into momentum distribution, which consents to follow the time evolution of the probe field (see Figure 5.2). On top of that, the photoemitted electrons bear the imprint of the temporal structure of the XUV AS pulse. Thus, an analysis of the spread of the streaked photoelectron distribution allows to characterize the features of the AS pulse itself, for example its bandwidth and chirp.

The streaking technique can be generalized to inhomogeneous systems. Previous work on attosecond streaking on metal nanoparticles [SK11] showed that for increasing radius, the photoelectron spectrogram is smeared out by the overlap of photoelectron trajectories ionized by the XUV in different regions of the plasmonic field. As a consequence, the field retrieved with Eq. (5.5) is distorted by the local plasmonic field acting on the photoelectrons. Thus if one wants to apply this method to plasmonic excitations on extended objects, it must be considered that the surface plasmon acting as the streaking field not only is spatially inhomogeneous but also propagates along the surface. Therefore, one needs to include the position dependence into the initial electron distribution: $n_e(\mathbf{p}_i, t_i) \rightarrow n_e(\mathbf{r}_i, \mathbf{p}_i, t_i)$. According to the Liouville theorem, the evolution of the distri-

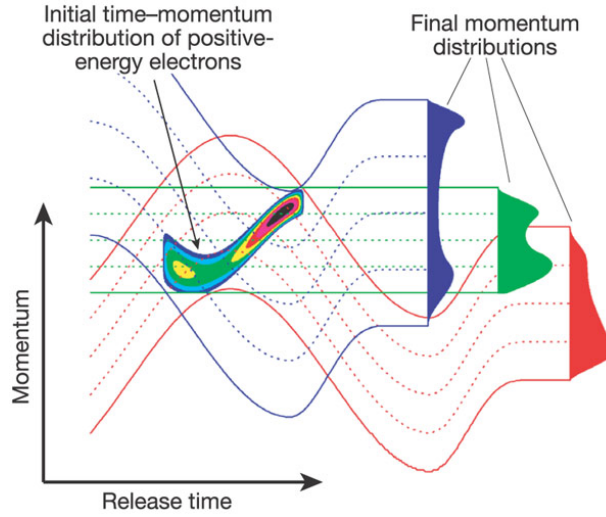


Figure 5.2: The attosecond streak camera (ASC) is an experimental technique mapping the time of photoionization into final momentum of the streaked photoelectron. If the streaking field is zero (green horizontal lines) the final momentum distribution recorded by the detector is the time integral of the unperturbed initial distribution. In case of non null electric field, the photoelectron distribution is shifted and distorted by the streaking field. The sequence of time-delayed final momentum distributions form the streaking spectrogram, which permits the characterization of both the streaking field, and the XUV-AS pulse. Figure reproduced from [Kie+04].

bution function is governed by

$$\frac{D}{Dt} n_e(\mathbf{r}_i, \mathbf{p}_i, t_i) = 0, \quad (5.6)$$

where D/Dt is the convective derivative, i.e. the derivative along the particle trajectories $D_t = \partial_t + \frac{\mathbf{p}_i}{m_i} \cdot \nabla_i$. Eq. (5.6) is formally solved by $n_e(\mathbf{r}_i(t), \mathbf{p}_i(t), t) = n_e(\mathbf{r}_i, \mathbf{p}_i, t_i)$, i.e. the photoelectron distribution function is constant along the photoelectron trajectories. Thus, the problem reduces to solving each single photoelectron trajectory in the plasmonic field. In order to find the trajectory, the momentum of the electrons accelerated in the plasmon field is needed, which is given by

$$\mathbf{p}(t) = \mathbf{p}_i - e \int_{-\infty}^t \mathbf{E}(\mathbf{r}(t'), t') dt'. \quad (5.7)$$

5.3 Low-speed approximation

Let us derive an approximation to solve Eq. (5.7). The carrier photon energy of the XUV-AS pulses considered here is 80 eV, thus the average initial speed of a photoelectron can

be estimated to be $v_i \sim 5$ nm/fs. For a driving NIR laser pulse of 4 fs duration and $5 \mu\text{m}$ focal spot, the excited plasmonic field duration can be assumed to not exceed a few tens of femtoseconds. In this time interval, the photoelectrons move in the plasmonic field by less than 100 nm. Since the additional velocity change due to the acceleration in the plasmonic field is small compared to the initial velocity, and the plasmonic evanescent field extension is of the order of the NIR wavelength (800 nm), the photoelectron position can be approximated by $\mathbf{r}(t') \simeq \mathbf{r}_i$ in Eq. (5.7). Thus, $\mathbf{E}(\mathbf{r}(t'), t') \simeq \mathbf{E}(\mathbf{r}_i, t')$, where $\mathbf{r}_i = \mathbf{r}(t = t_i)$. This is the zero order approximation of the Taylor series:

$$\mathbf{E}(\mathbf{r}(t), t) \simeq \mathbf{E}(\mathbf{r}_i, t) + \left. \frac{\partial \mathbf{E}}{\partial \mathbf{r}(t)} \right|_{\mathbf{r}(t)=\mathbf{r}_i} (\mathbf{r}(t) - \mathbf{r}_i) + \dots,$$

which is equivalent to neglecting the transport effects in the vector potential time derivative:

$$\frac{d}{dt} \mathbf{A}(\mathbf{r}(t), t) = (\partial_t + \mathbf{v} \cdot \nabla_{\mathbf{r}}) \mathbf{A}(\mathbf{r}(t), t) \simeq \partial_t \mathbf{A}. \quad (5.8)$$

The integral equation (5.7) now reads:

$$\mathbf{p}(t) = \mathbf{p}_i + \frac{e}{c} [\mathbf{A}(\mathbf{r}_i, t) - \mathbf{A}(\mathbf{r}_i, t_i)]. \quad (5.9)$$

Assuming $\mathbf{A}(\mathbf{r}_i, t \rightarrow \infty) \rightarrow 0$, the position corrected version of Eq.(5.1) is obtained:

$$\mathbf{p}_f = \mathbf{p}_i + \frac{e}{c} \mathbf{A}(\mathbf{r}_i, t_i). \quad (5.10)$$

Since the photoelectron detector does not provide any spatial resolution, the photoscopic spectrogram is the integral over time *and space* covered by the XUV focal spot on the grating surface:

$$\sigma(\mathbf{p}_f, \tau) = \int_{\mathbb{R}^3} d^3 r_i \int_{-\infty}^{\infty} dt_i n_e(\mathbf{r}_i, \mathbf{p}_f - \mathbf{a}(\mathbf{r}_i, t_i), t_i - \tau). \quad (5.11)$$

Since the spatial or temporal integral of a propagating pulse is negligible (exactly zero in free space, valid as long as the polarization is orthogonal to the propagation direction), the average momentum is independent of the time-delay. In order to extract the time information from the photoscopic spectrogram, one has to analyze the momentum variance

$$S(\tau) = \frac{\int d\mathbf{p}_f |\mathbf{p}_f|^2 \sigma(\mathbf{p}_f, \tau)}{\int d\mathbf{p}_f \sigma(\mathbf{p}_f, \tau)} - |\langle \mathbf{p}_f \rangle|^2, \quad (5.12)$$

where $\langle \mathbf{p}_f \rangle$ was defined in Eq. (5.4).

5.4 Approximation of the photoelectron distribution function

The photoemission process can be regarded as instantaneous, because the XUV pulse duration is short compared to the NIR period and its interaction with the solid is weak.

Moreover, any possible effect of electron transport in the solid is discarded and only the photoelectrons coming from the first few layers of material are taken into account, an assumption consistent with what reported in [Nep+12]. Furthermore, the photoelectron spatial distribution along the grating surface is a replica of the XUV pulse intensity profile. Thanks to these considerations n_e can be factorized as:

$$n_e(\mathbf{r}_i, \mathbf{p}_i, t_i - \tau) \simeq g_x(x_i) n_e(\mathbf{p}_i) \delta(y_i - y_s) \delta(t_i - \tau - t_0), \quad (5.13)$$

where y_s is the grating surface average position and g_x is the shape function of width w_x of the XUV focal spot.

The last point needing discussion concerns the nature of the angular dependence of the photoemission. For simplicity one can take into consideration only the two extremal cases where the initial momenta are either all orthogonal to the grating plane, or are all emitted in random directions. The conjecture behind this reasoning is that the actual physical situation falls between the two cases of unidirectional or isotropic photoemission, and has to be determined in a measurement without NIR field. It will be later shown that the unidirectional case can be “filtered out” from the isotropic one by choosing a proper measurement geometry, and that for either distribution, the reconstructed times closely reproduce the actual dynamics.

5.4.1 Unidirectional distribution of the photoelectrons

A unidirectional initial distribution can be expressed as $n_e(\mathbf{p}_i) = n_e(p_i \hat{\mathbf{n}}_s)$, where $p_i = |\mathbf{p}_i|$ and $\hat{\mathbf{n}}_s$ is the direction perpendicular to the grating plane. Substitution into Eq. (5.11) gives

$$\sigma(p_f, \tau) = \int_{-\infty}^{\infty} dx_i g_x(x_i) n_e(p_f - \hat{\mathbf{n}}_s \cdot \mathbf{a}(x_i, t_0 - \tau)),$$

where $\hat{\mathbf{n}}_s$ indicates the surface normal. In proximity of the grating, the plasmonic field is mostly perpendicular to the surface, hence the quantity $\hat{\mathbf{n}}_s \cdot \mathbf{a} = \mathbf{a}_y$ is approximately equal to the entire potential \mathbf{a}_{spp} . Computation of the variance in Eq. (5.12) for a Gaussian distribution of the initial electron momenta yields

$$S(\tau) = \Delta p^2 + \int_{-\infty}^{\infty} dx_i g_x(x_i) \mathbf{a}_{\text{spp}}^2(x_i, t_0 - \tau). \quad (5.14)$$

5.4.2 Isotropic distribution of the photoelectrons

For the case of isotropic XUV photo-electron emission, the initial distribution can be written as: $n_e(\mathbf{p}_i) = \frac{1}{\pi} n_e(p_i) = \frac{1}{\pi} n_e(|\mathbf{p}_f - \mathbf{a}|)$, where $p_i = |\mathbf{p}_i|$ was used. Also, $|\mathbf{a}| \ll |\mathbf{p}_f|$ is assumed to approximate $|\mathbf{p}_f - \mathbf{a}| \simeq p_f - \mathbf{a} \cdot \hat{\theta}$, where θ is the angle between the final momentum and the surface normal. The spectrogram can be now cast into

$$\sigma(p_f, \tau) = \frac{1}{\pi} \int_{-\infty}^{\infty} dx_i g_x(x_i) n_e(p_f - \mathbf{a} \cdot \hat{\theta}). \quad (5.15)$$

A lengthy but straightforward calculation for the angular integrations leads to the expression

$$S(\tau) = \Delta p^2 + \frac{1}{\pi} \int_{-\infty}^{\infty} dx_i g_x(x_i) |\mathbf{a}(x_i, \tau)|^2. \quad (5.16)$$

In any case, measuring the variance of the photoscopic spectrogram by use of Eqs. (5.14) or (5.16) provides direct access to the space-averaged vector potential \mathbf{a}^2 at the surface in the direction of the photoelectron detector. The vector potential $|\mathbf{a}|^2 = \mathbf{a}_x^2 + \mathbf{a}_{\text{spp}}^2$ also includes a_x , the NIR field incident on the grating surface.

5.5 Numerical simulation of the photoscopic spectrogram

As in Chapter 4, simulations of the plasmonic field were performed using MEEP [Osk+10]. The properties of the grating material were included by modeling the optical constants with Drude and Lorentz response functions as given in Eq. (4.10), with parameters taken from [Rak+98a]. A test of the goodness of the employed numerics is reported in Appendix A. We assumed a NIR pulse of temporal Gaussian profile, with 4 fs FWHM duration at a central wavelength of 800 nm. The grating parameters were optimized for maximal absorption of the NIR pulse. Beam waists of NIR and XUV were 5 and 10 μm , respectively.

The XUV photoemission is modeled by a Monte Carlo process, where the random ejection time, position and momentum are assigned according to the relative unidirectional or isotropic probability distribution described in Sec. 5.4. The electrons final momenta are calculated solving the Lorentz equations in the plasmonic field, for the corresponding initial conditions generated in the Monte Carlo simulation.

The key point is to understand whether the result of the low-speed approximation contained in Eq. (5.16), is accurate or not. Since it is possible to directly access the simulated plasmonic field, it can be checked whether the variance of the numerically simulated photoscopic spectrogram is in good agreement with Eq. (5.16) computed using directly the FDTD field.

The spectrogram variance obtained with the Monte Carlo simulation is compared in Fig. 5.3 with the space integral of the squared vector potential along the y -direction from

the FDTD simulation. We assumed isotropic initial momentum distribution and a time-of-flight (TOF) detector of acceptance angle 5° centered around the direction perpendicular to the grating.

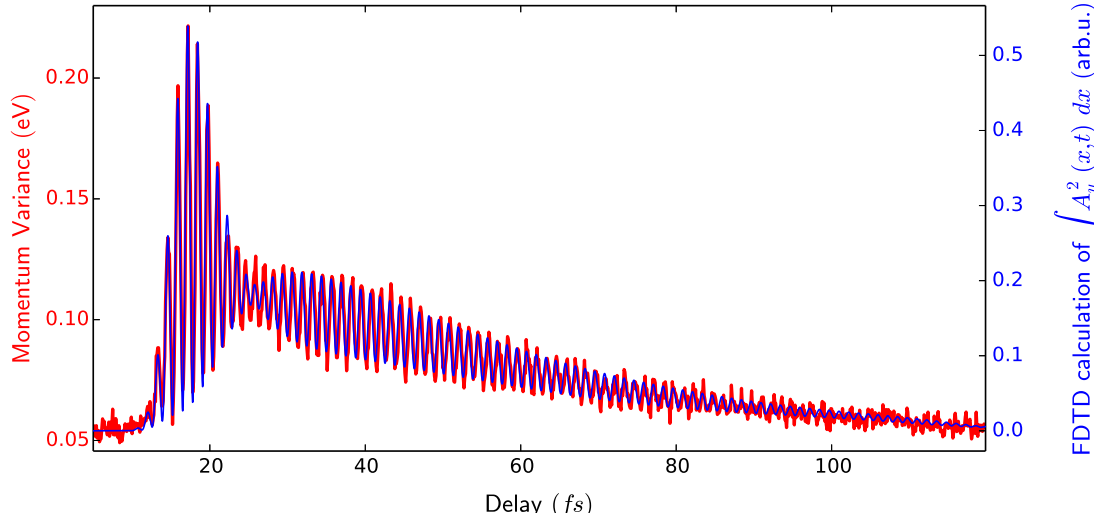


Figure 5.3: The figure shows a comparison of the momentum variance calculated from the spectrogram in the filtered isotropic emission case of photoelectron streaked by the FDTD field, and the integral of the superficial potential squared $\int |\mathbf{a}_y|^2$ calculated directly from the FDTD dataset. The offset of the momentum variance is due to the XUV pulse bandwidth. The perfect overlap of the curves proves the validity of the theoretical model and in particular of the low-speed approximation, cf. Sec. 5.3. Figure reproduced from [Lup+14].

It is worth noting that the variance calculated from the Monte Carlo simulation directly images the integral of the surface plasmonic field squared, without further assumptions or approximations from the theory.

The results are analogous for the unidirectional emission, meaning that the agreement is robust with respect to the angular distribution of the photoelectrons. Therefore, knowledge of the precise photoelectron spectrum of the grating is not crucial for the proposed experiment.

In Fig. 5.4 the calculated photoscopic spectrograms for a unidirectional and isotropic initial electron distribution are compared. In the isotropic case the contributions of both the parallel and perpendicular components of the total field are captured. To identify their origins, the recording process was simulated by using a time-of-flight (TOF) spectrometer placed respectively at normal and grazing incidence incidence w.r.t. the grating surface. The resulting “filtered” spectrograms are shown in Fig. 5.5. With an angular resolved TOF measurement, it is possible to isolate the parallel component, dominated by the NIR pulse reflected at the surface, from the perpendicular one, containing the excited plasmonic field. Note that the unidirectional case, showing only the plasmonic contribution, can be obtained by appropriate measurement also in the case of isotropic emission.

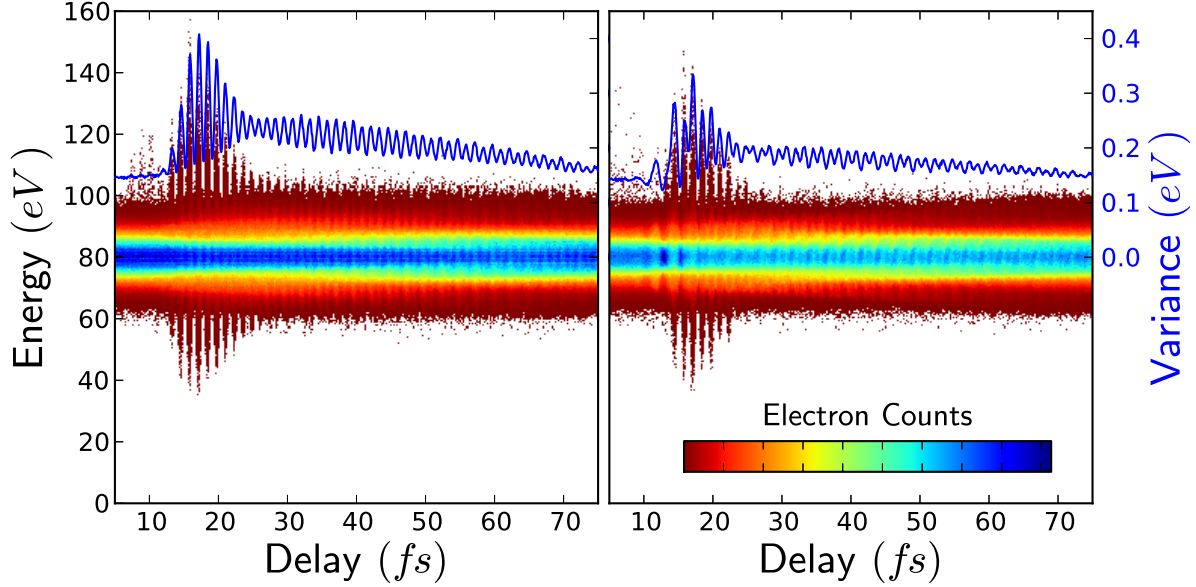


Figure 5.4: Photoscopic spectrograms obtained with a unidirectional (left) and isotropic (right) photoelectron distribution, with solid lines representing the relative variances.

For these reasons, the imaging of the fields in the isotropic case provides an *in situ* diagnosis of both the plasmonic field and the driving NIR pulse at the surface, allowing the possibility to investigate the distortion of the NIR pulse undergoing reflection on the grating surface.

5.6 Analytic model for the SPP field on a grating

A model for the excited plasmonic field has to be defined in order to extract the buildup- and life-times, as well as the bright and dark mode contributions to the photoscopic spectrogram. The field envelope is assumed to be a Gaussian: $\mathbf{a}_{\text{spp}} = \exp[i\varphi] \exp[-\varphi^2/2\omega_{\text{spp}}^2 T^2]$, with $\varphi = k_{\text{spp}}x - \omega_{\text{spp}}t$. There are two counter-propagating SPP wave-packets, each containing a bright ω_b and a dark ω_d frequency. In the chosen configuration both the bright and the dark mode can be excited at frequencies ω_b and ω_d , respectively. Here “bright” and “dark” refer to the coupling properties of the modes: with plane waves only the bright mode would be excited, and thus visible, but thanks to the k-vector dispersion of the tightly focused beam also the dark mode contributes to the spectrogram (cf. sec. 5.7). As shown in Figure 5.6, the two frequencies are well separated. Each counter-propagating plasmonic wavepacket contains both. In addition, a term describing the ringing of a localized mode excited in the focus of the NIR pulse is added (see [GV+99]). This term can be dominant for very deep gratings, but in the present configuration is smaller than the propagating

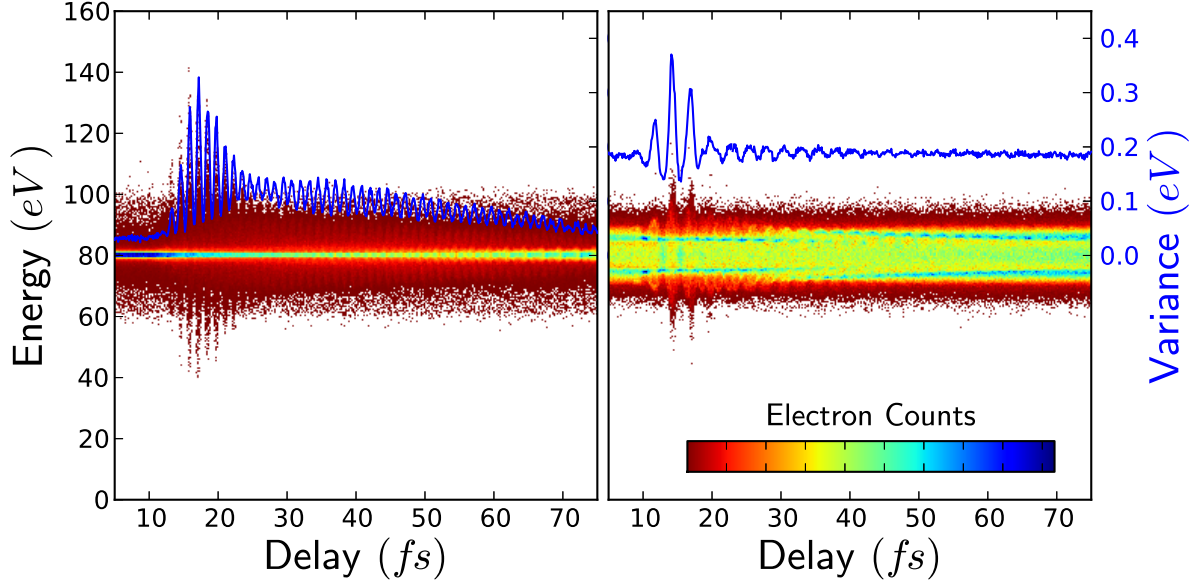


Figure 5.5: Photoscopic spectrograms at perpendicular (left) and grazing (right) electron emission. The filtering is performed by simply setting a TOF detector at 90° and 0° degrees with respect to the grating plane. The solid lines are the relative momentum variances, with which one can retrieve plasmonic and NIR field, respectively. Figure reproduced from [Lup+14].

components. The contributions of each mode $m = b, d$ to the plasmonic wavepacket are

$$P_m^{(\pm)} = e^{i\varphi_{\pm m}} e^{-\frac{\varphi_{\pm m}^2}{2\omega_m^2 T_m^2}}, \quad (5.17)$$

with the phase of the propagating plasmon

$$\varphi_{\pm m} = \pm k_m x - \omega(t - t_m) \quad (5.18)$$

and

$$P_m^{(0)} = \cos(\omega_m(t - t_m)) e^{-x^2/2\omega_{\text{nir}}^2}, \quad (5.19)$$

for the localized excitation.

Buildup and decay are assumed to obey a simple rate equation where a Gaussian-shaped buildup of width σ is depleted by decay at a constant rate τ :

$$\dot{f}(t) = e^{-\frac{t^2}{2\sigma^2}} - \frac{1}{2\tau} f(t). \quad (5.20)$$

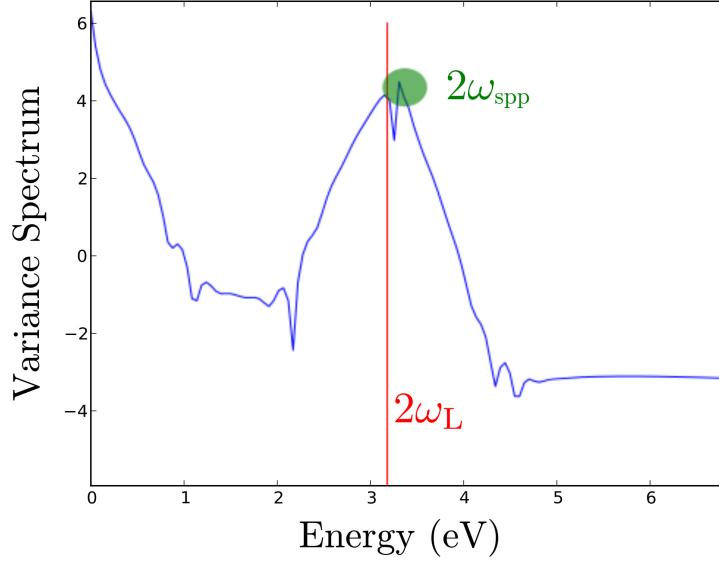


Figure 5.6: Fourier transform of the momentum variance of the photoscopic spectrogram calculated according to Eq. (5.16) on the dataset obtained from the FDTD calculation, with parameters given in sec. 5.5.

The resulting time-distribution is

$$\begin{aligned}
 f(t, \sigma, \tau) &= \int_0^t e^{-\frac{t'^2}{2\sigma^2}} e^{-\frac{t-t'}{2\tau}} dt' \\
 &= e^{\frac{\sigma^2 - 4\tau t}{8\tau^2}} \left[1 - \operatorname{erf} \left(\frac{\sigma^2 - 2\tau t}{2\sqrt{2}\tau\sigma} \right) \right].
 \end{aligned} \tag{5.21}$$

With these assumptions, the complete field is parametrized by

$$\begin{aligned}
 \mathbf{a}_y(x, t) &= \sum_{m=b,d} f(t-t_m, \sigma_m, \tau_m) \\
 &\quad \times \left\{ a_m \left[P_m^{(+)} - P_m^{(-)} \right] + c_m P_m^{(0)} \right\}.
 \end{aligned} \tag{5.22}$$

In practice, it is found that the bright mode decays so fast that its propagation can be neglected in the spectrogram variance, which allows to set $a_b \equiv 0$.

The buildup time of each mode is defined as $\xi_m = \sigma_m \sqrt{\ln(2)}$, the half-width half-maximum of the Gaussian function in Eq. (5.21), which permits a direct comparison with the NIR pulse FWHM duration.

It is found that the dark mode plasmon duration T has a measurable effect only during

the generation phase, when counter-propagating SPPs have not separated yet and form a standing wave. Since this process is superposed by the bright mode, it cannot be reliably retrieved from the fit. On the other hand, T is only weakly correlated with the dynamical parameters ξ_m, τ_m and ω_m . A conservative lower bound of T can be set to the diameter of the NIR spot size, and upper bound to that size plus the plasmon propagation during the excitation. The dynamical parameters for variations of T are shown in Table 5.1 over the range of [10, 20] fs (FWHM).

Table 5.1: Buildup-, life-time, and frequency of the bright and dark modes as obtained by fitting Eq. (5.16) with the parameterization (5.22), for a range of plasmon durations T_m . Times in fs, frequencies in eV, $T_{FWHM} = 2\sqrt{\ln 2}T$.

T	6	7	8	9	10	11	12	Var
T_{FWHM}	9.99	11.66	13.32	14.99	16.65	18.32	19.98	
ξ_b	1.933	1.964	1.987	2.004	2.016	2.025	2.031	5 %
τ_b	3.285	3.137	3.031	2.964	2.924	2.903	2.896	13 %
ξ_d	5.941	5.649	5.430	5.286	5.202	5.160	5.149	15 %
τ_d	34.18	34.41	34.57	34.63	34.62	34.57	34.47	< 1 %
ω_b	1.613	1.615	1.616	1.617	1.617	1.616	1.615	< 1 %
ω_d	1.645	1.645	1.645	1.645	1.645	1.645	1.645	< 1 %

The amplitudes of the respective plasmon modes are the remaining fitting parameters, which are not reported here, since the relevant free parameters in this study are the excitation buildup times ξ_b, ξ_d , the plasmon decay times τ_b, τ_d and the plasmon frequencies ω_b, ω_d for the bright and dark modes, respectively. The result of the fitting procedure for $T = 15$ fs (FWHM) is shown in Fig. 5.7.

5.7 Origin of the dark and bright modes

The values of the bright and dark mode frequencies are $\hbar\omega_b = 1.65$ eV and $\hbar\omega_d = 1.62$ eV, which are consistent with the plasmonic band gap of 14 nm given in Ref. [Rop+07].

It is interesting to comment on the origin of the bright and dark frequencies. In Figure 5.8 the plasmonic band structure of the grating is displayed. A plane wave at normal incidence would be able to couple only with the upper branch of the structure. However, the NIR source pulse is a tightly focused Gaussian pulse having a non-zero Δk spectral width, besides the $\Delta\omega$ bandwidth. Thus, the dark mode that would be otherwise impossible to excite, becomes visible due to k -components non-orthogonal to the grating plane. The coupling area is shown as a black rounded box in Fig. 5.8.

The result of the large beam divergence is that the excitation spectrum is not simply a cut of Fig. 5.8 at $\theta = 0$, but a convolution of the reflectivity with the angular spectrum of the Gaussian pulse. Thus, also the dark mode becomes visible. In Fig. 5.9 is reported

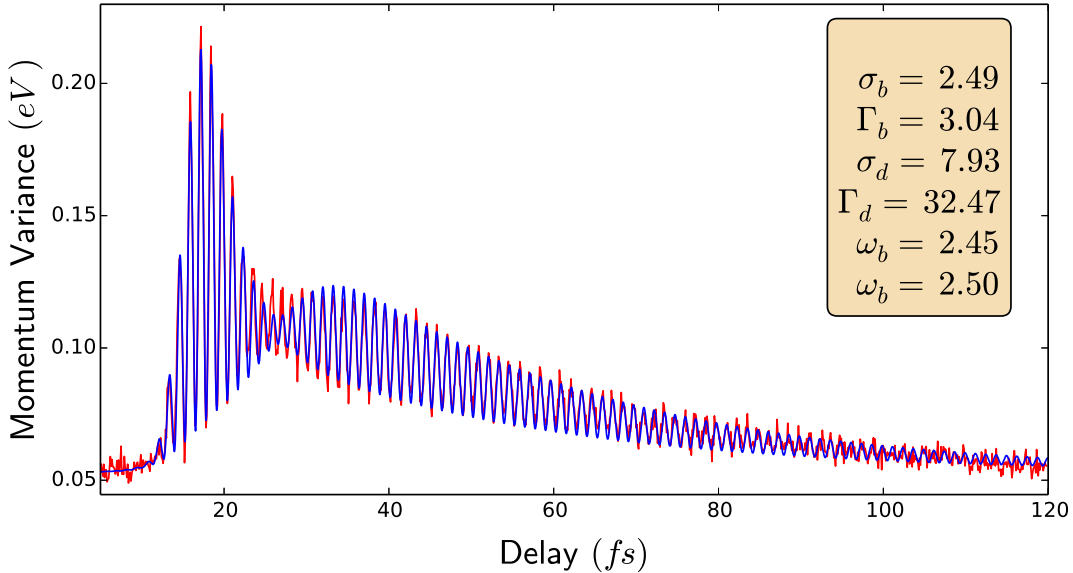


Figure 5.7: Best fit optimization of the plasmonic field model parameters against the variance of the photoscopic spectrogram in the filtered isotropic case. In the inset the errorless values of the relevant parameters as reported in Table 5.2.

a comparison between the reflectivity spectrum of the grating calculated for a normal incident plane wave and Gaussian beam of FWHM spot size of $4 \mu\text{m}$. The pulse duration is 4 fs FWHM for both cases. The extra peak appearing in Fig. 5.9 is consistent with the dark mode frequency obtained from the best fit optimization.

5.8 Results

In Table 5.2 the results for the buildup- and life-times obtained with $T = 15$ fs (FWHM) are reported. The plasmon pulse duration T has little influence on the variance, because of the spatial integration. Variations in the range between 10 and 20 fs have only a small effect on buildup and decay times. With a variation of about 0.7 fs, the effect is largest on the bright and dark mode decay times, due to their overlapping. For any given value of T in this interval, the buildup and decay times extracted from the FDTD surface field and from the spectrogram variance are in good agreement.

The plasmonic field enhancement can be evaluated from the comparison of the NIR vs. the plasmonic field in the two spectrograms shown in Figure 5.5. In the present case, it is ~ 1 . From the spectrogram at grazing direction, the NIR pulse duration is $\Delta t_{\text{fwhm}} = 4.5$ fs, in good agreement with the 4.6 fs from the FDTD code. This measurement constitutes an *in situ* diagnosis of the distortions of the NIR pulse while being reflected from the grating.

Summarizing, this method allows to image the plasmonic field of SPPs, using only al-

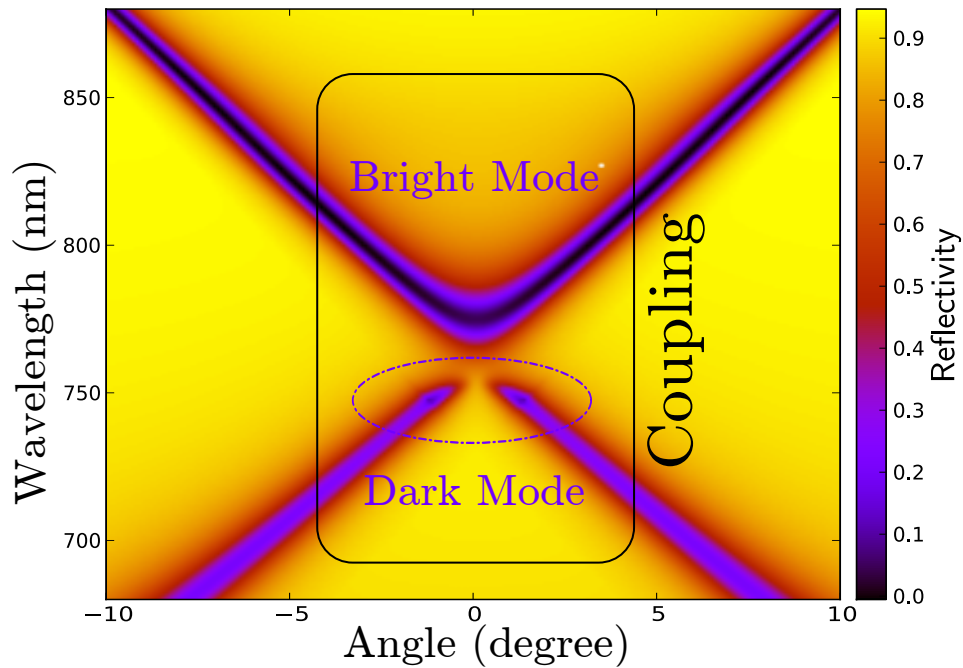


Figure 5.8: SPP excitation mechanism on a gold grating. When the excitation source is an ultrashort tightly focused Gaussian beam, the wave-vector and frequency broad bands allow coupling with the dark mode even at normal incidence. The beam divergence for a FWHM spot size of $5\ \mu\text{m}$ at $800\ \text{nm}$ is about 5° .

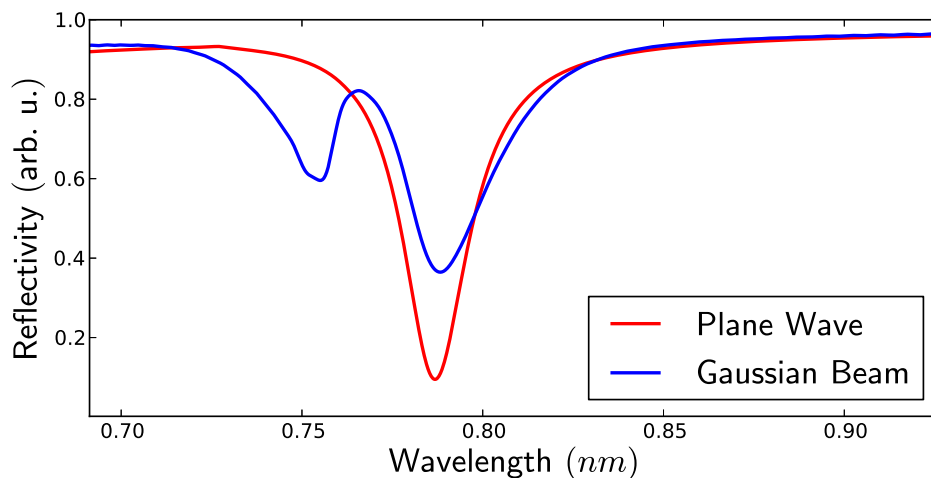


Figure 5.9: Comparison between the reflectivity spectra of the grating structure illuminated respectively with a plane wave and a Gaussian beam.

ready existing equipments typical of attosecond metrology. The technique can be easily

Table 5.2: Best fit optimization of the carrier frequency ω_m , buildup time ξ_m and lifetime τ_m against the numerically simulated data. The cases of isotropic emission with perpendicular detection (“filtered”), unidirectional emission, as well as values extracted directly from the FDTD calculation are shown. (Times in fs. Frequencies in eV), table taken from [Lup+14].

	Filtered Isotropic	Unidirectional	FDTD
ξ_b	2.07	2.06	2.01
τ_b	3.0	3.1	2.96
ξ_d	6.6	6.2	5.3
τ_d	32.5	33.3	34.6
ω_b	1.61	1.62	1.62
ω_d	1.65	1.65	1.65

extended to any kind of surface plasmonic excitation, by suitably reformulating the analytical model for the plasmonic field. Recent developments of the experimental apparatuses indicates the possibility to spatially separate the XUV and NIR pulse while keeping the attosecond precise synchronization. In this scenario, this technique could provide time *and space* resolved imaging of virtually any surface phenomena: by exciting a surface mode with the NIR pulse in some region, one can follow the dynamics of the excitation along complex nanostructured components by simply pointing the attosecond XUV pulse on the region of interest. The basic parameters important for the chosen configuration can then be determined by controlling the relative pulse delay. This allows the extraction of parameters such as buildup- and life-times. Within the same experiment, also an *in situ* diagnostics of the driver NIR pulse can be performed.

6

Modeling and Simulation of SPPs

In the previous chapters the excitation of plasmonic fields in the different configurations were calculated by numerically solving the Maxwell's equations in presence of an external source. In matrix form they read:

$$\frac{\partial \phi}{\partial t} = \frac{\partial}{\partial t} \begin{pmatrix} \mathbf{E} \\ \mathbf{H} \end{pmatrix} = \begin{pmatrix} 0 & \epsilon^{-1} \nabla \times \\ -\mu^{-1} \nabla \times & 0 \end{pmatrix} \begin{pmatrix} \mathbf{E} \\ \mathbf{H} \end{pmatrix} + \begin{pmatrix} -\epsilon^{-1} \mathbf{J} \\ 0 \end{pmatrix} = \hat{D} \phi + S \quad (6.1)$$

where the constitutive relations $\mathbf{D} = \epsilon \mathbf{E}$, $\mathbf{B} = \mu \mathbf{H}$ were used. ϵ and μ are respectively the dielectric and magnetic permittivity tensors, and contain the physical properties of the system under consideration. For frequency dependent dielectric and magnetic functions, it is more convenient to use a set of additional time dependent equations for the polarization \mathbf{P} and magnetization \mathbf{M} of the system, assuming a Drude-Lorentzian dependence of the form [Osk+10]:

$$\epsilon(\omega) = \epsilon_{\infty} - \frac{\omega_{\text{pl}}^2}{\omega^2 + i\omega\gamma} + \sum_{i=1}^N \frac{f_i \omega_i^2}{\omega_i^2 - \omega^2 - i\omega\gamma_i}, \quad (6.2)$$

where the first (Drude) term refers to the interacting free-electron gas response, and the additional (Lorentz) terms are usually employed for the modeling of interband transitions. Such a form corresponds to a set of time domain equations for each term in the dielectric function given by [Osk+10]

$$\frac{\partial^2 \mathbf{P}_i}{\partial t^2} + \gamma_i \frac{\partial \mathbf{P}_i}{\partial t} + \omega_i^2 \mathbf{P}_i = f_i \omega_i^2 \mathbf{E}, \quad (6.3)$$

for the Lorentz term and by [Osk+10]

$$\frac{\partial^2 \mathbf{P}_D}{\partial t^2} + \gamma \frac{\partial \mathbf{P}_D}{\partial t} = \omega_{\text{pl}}^2 \mathbf{E}, \quad (6.4)$$

for the Drude term. Then, the dielectric function is set to $\epsilon = \epsilon_{\infty}$ in Eq. (6.1) and the polarization term $\mathbf{P} = \mathbf{P}_D + \sum_i \mathbf{P}_i$ is added as source term in Eq. (6.1). The same

procedure must be performed also for the magnetization term. Such implementation is more convenient when solving the Maxwell's equations in the time domain, since it avoids Fourier transforming the fields in the whole space at each time step.

The solutions of Eq. (6.1) were obtained using MEEP [Osk+10], an open-source library which implements the Finite-Difference Time-Domain (FDTD) scheme for Maxwell's equations. In the FDTD method, both the time and space derivatives are computed on a staggered grid, in which the fields \mathbf{E} and \mathbf{H} are stored at grid positions shifted in space and time with respect to each other of $\Delta t/2$ and $(\Delta x, \Delta y, \Delta z)/2$. This grid, reported in Figure 6.1, is called the “Yee lattice” and allows to derive a numerical scheme that ensures second order accuracy of the first order derivatives as well as remaining explicit (for a comprehensive treatment, see [Taf05]).

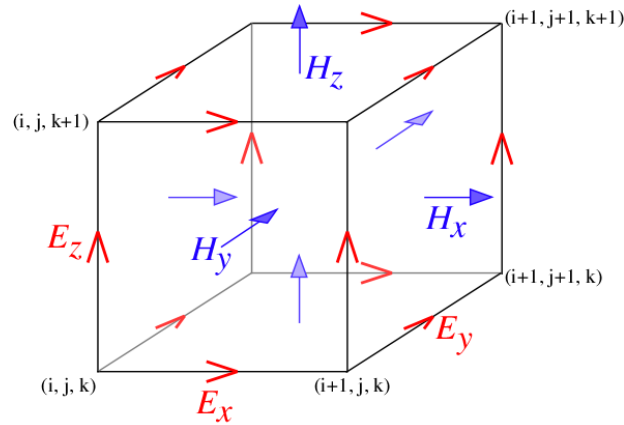


Figure 6.1: In the FDTD method, both time and space derivatives are computed on a staggered grid, in which the fields \mathbf{E} and \mathbf{H} are stored at grid positions shifted in space and time with respect to each other of $\Delta t/2$ and $(\Delta x, \Delta y, \Delta z)/2$. Here the 3D spatial grid with relative position of the electromagnetic field components is shown.

The solution propagating outside the simulation box is absorbed by boundary layers called Perfectly Matched Layers (PML) [Ber94], which allow for negligible reflection of the solution inside the simulation box. The reason why absorbing layers are needed is that asymptotic solutions of the wave equation are oscillating functions which decay slowly with r as $r^{(1-d)/2}$, with d the dimension of the problem. Thus, either a truncation of the simulation box would produce reflection, or a remapping of the outer region would increase the oscillation frequency in a way that it would not be resolved by the grid anymore.

The idea behind the PML is to define an absorbing region by *complex stretching* the spatial coordinates. The result is that in this domain the outgoing oscillating solution becomes exponentially decaying, without affecting the solution in the unstretched region.

6.1 Limitations of PMLs

PMLs typically fail when the simulation box contains materials which are not invariant with respect to the PML stretching direction. This happens because the solution is no longer separable in the coordinates and the standard formulation of the PMLs is not valid anymore [Joh10]. Unfortunately, one of the most common problem in plasmonics, the excitation of SPPs on diffraction gratings, falls exactly into this category. The reason is that a grating is not translation invariant in the direction of propagation of the SPP, in fact it owns a discrete translation invariance, whose discreteness is given by the grating periodicity. As a result, back coupling of the surface wave to the far field in the PML region generates incoming waves which grow exponentially.

This problem is the object of investigation of this chapter, together with a mathematical foundation of the absorbing properties of complex scaling in the case of Maxwell's equations, which, to the knowledge of the author, is lacking. The PML method is analyzed using a spectral decomposition and compared with the exterior complex scaling (ECS) method. The ECS was proposed in [Sim79] as an extension of the complex scaling method first established in [BC71] for Schrödinger operators and applied in general to the scaling of dispersive equations. Both methods can be derived through analytical continuations from unitary transformations. It is shown that the methods are mathematically and numerically distinct: ECS is a complex stretching that rotates the Schrödinger operator's spectrum into the complex plane, whereas PML is a complex gauge transform which shifts the Maxwell operator's spectrum in the complex plane.

6.2 Exterior Complex Scaling (ECS)

In this paragraph the method exposed in Ref. [SSM14] for building absorbing boundaries of equations of the form

$$i \frac{\partial}{\partial t} \phi[t](x) = \hat{D} \phi[t](x) \quad (6.5)$$

is illustrated. It contains the necessary concepts required to implement mathematically rigorous absorbing conditions for Maxwell's equations. In Eq. (6.5), ϕ is a multi-component wavefunction, and \hat{D} is a linear differential operator. The system Eq. (6.1) can be cast as in Eq. (6.5) by defining the 6×6 Maxwell's differential operator:

$$\hat{O}_M = i \hat{D} = i \begin{pmatrix} 0 & \epsilon^{-1} \nabla \times \\ -\mu^{-1} \nabla \times & 0 \end{pmatrix} \quad (6.6)$$

In the domain F the solution of Eq. (6.5) must remain unmodified by the absorption occurring in the boundary domain $x \notin F$. The idea is to convert the indefinitely propagating solution in the outer region to an exponentially decaying form by continuing it into the positive complex plane for $x \notin F$. Let the analytically continued solution be labeled by a

complex number η . For the new equation with exponentially decaying asymptotic solution

$$i \frac{\partial}{\partial t} \psi_\eta[t](x) = D_\eta \psi_\eta[t](x), \quad (6.7)$$

one requires that:

$$\phi[t](x) = \psi_\eta[t](x) \quad \text{for } x \in F, \forall t. \quad (6.8)$$

For this, a transformation can be constructed, such that it is unitary for real values of η and respects Eq. (6.8). For complex η an asymptotically decaying solution can be obtained such that (6.8) is maintained.

To arrive at the scaled equation (6.7) one can proceed in successive steps. At first, let us introduce a unitary scaling U_λ that leaves the solutions invariant on F for real values of λ . The exterior real scaling for instance is the transformation [SSM14]

$$(U_\lambda \psi)(x) = e^{\lambda \Theta_F(|x|)/2} \psi(z_\lambda(x)), \quad z_\lambda(x) := \frac{x}{|\lambda|} \int_0^{|x|} dr e^{\lambda \Theta_F(r)}, \quad (6.9)$$

with

$$\Theta_F(|x|) = 0 \quad \text{for } x \in F, \quad \Theta_F(|x|) > 0 \quad \text{for } x \notin F. \quad (6.10)$$

The transformation U_λ is unitary for all real values of λ . The choice of Θ_F is important only for the numerical problem, but in principle can also be discontinuous. The discontinuous function $\Theta_F(|x|) = 1$ for $x \notin F$ will be used, which leads to analytically simple scaling. With this, one can define the self-adjoint scaled operator $D_\lambda := U_\lambda D U_\lambda^{-1}$ and show its analyticity w.r.t. λ .

After that, Eq. (6.7) must be solved in the spectral domain and shown that $\psi_\lambda[t](x)$ is an analytic function of λ . Then the solution can be analytically continued to complex values $\eta = \lambda + i\theta$ and one can conclude that $\psi_\eta[t](x)$ does not depend on η for $x \in F$.

Finally, the stability of the time dependent problem must be ensured. For this, it is sufficient that the spectrum of the discrete representation of D is in the lower half of the complex plane, so that $\psi_\eta[t](x)$ does nowhere grow exponentially in time.

As an example, let us consider the one dimensional advection equation, $\hat{D} = -i\partial_x$. The scaled spectral eigenfunctions are [SSM14]

$$w_\lambda(x, k) \sim \exp[ike^\lambda \Theta_F(x)x]. \quad (6.11)$$

The solution of Eq. (6.7) in term of the spectral expansion for the case of global scaling can be shown to be (see [SSM14] for the derivation)

$$\psi_\lambda[t](x) = \int dk e^{-\lambda} w_\lambda(x, k) e^{-ie^{-\lambda} kt} \tilde{\psi}[0](k). \quad (6.12)$$

If in the unscaled solution $\psi[t]$ propagates outwards, then the scaled solution at fixed time t decays exponentially with $|x|$. However, for inwards propagating terms this procedure

will cause an exponential growth in time, because $k \sin(\theta)$ reverse its signs for the negative part of the spectrum of \hat{D} . Thus, while a rotation of the spectrum of an angle θ is a good solution for the scaling of the Laplace operator, it does not produce the desired effect for the advection operator, and in general for those operator whose spectrum covers the entire real axis.

To overcome this problem, in PMLs each spectral function is separately scaled by a k -dependent factor. For scaling of $-i\partial_x$ one replaces in (6.9) $e^{\lambda\Theta_F/2} \rightarrow 1 + \lambda/k\Theta_F$. A spectral shift by λ results in:

$$w_\lambda(x, k) \sim U_\lambda e^{ikx} = e^{ik(1+\lambda/k\Theta_F(x))x} = e^{i(k+\lambda\Theta_F(x))x}. \quad (6.13)$$

For $\lambda = i\theta$ all spectral functions decay equally with $e^{-\theta x}$, irrespective of their direction. The key effect is due to the k -dependent sign change, which ensures that both the positive and negative parts of the spectrum are simultaneously exponentially damped. The transformation U_λ in Eq. (6.13) is a local gauge transform

$$(U_\lambda \phi)(x) = e^{i\lambda\Theta_F(x)x} \phi(x), \quad (6.14)$$

thus being unitary for real values of λ . Let us compute the effect of the new transformation on $D = -i\partial_x$. On functions in the domain of the scaled operator $\chi \in \mathcal{D}(D_\lambda) = U_\lambda \mathcal{D}(D)$, the action of D_λ is

$$D_\lambda \chi = e^{i\lambda\Theta_F(x)x} D e^{-i\lambda\Theta_F(x)x} \chi = [D - \lambda\Theta_F(x)] \chi. \quad (6.15)$$

By choosing $\chi \in \mathcal{D}(D_\lambda)$, δ -like contributions at the border ∂F were excluded. Upon analytic continuation to $\lambda \rightarrow i\theta$, the gauge transformation resulting from the PMLs approach shifts the spectrum in the lower half of the complex plane $\sigma(D_\lambda) = k - i\theta$, instead than rotating it like in the ECS case.

In higher dimensions, the action of U_λ on the eigenfunction $\exp\{i\mathbf{k}\mathbf{x}\}$ is given in a similar way by:

$$U_\lambda e^{i\mathbf{k}\mathbf{x}} = e^{i\mathbf{k}\mathbf{x}} e^{i\lambda(x+y+z)}. \quad (6.16)$$

One can define a $\vec{\lambda} = (\lambda_x, \lambda_y, \lambda_z)$, so that

$$U_\lambda e^{i\mathbf{k}\cdot\mathbf{x}} = e^{i\vec{\lambda}\cdot\mathbf{x}} e^{i\mathbf{k}\cdot\mathbf{x}} \quad \text{and} \quad \nabla \longrightarrow \nabla + i\vec{\lambda}. \quad (6.17)$$

6.3 Scaling of Maxwell's equations

Before proceeding with the scaling, let us find a simpler form of Maxwell's operator Eq. (6.6). In the simple case of space-independent dielectric and magnetic tensor, by defining the new basis $\{\mathbf{E}, \mathbf{H}\} \longrightarrow \left\{ \mathbf{F}_+ = \frac{\mathbf{E}}{\sqrt{\epsilon}} + i\frac{\mathbf{H}}{\sqrt{\mu}}, \mathbf{F}_- = \frac{\mathbf{E}}{\sqrt{\epsilon}} - i\frac{\mathbf{H}}{\sqrt{\mu}} \right\}$, the Maxwell's operator can

be written in diagonal form

$$\begin{pmatrix} ic\nabla \times & 0 \\ 0 & -ic\nabla \times \end{pmatrix}, \quad (6.18)$$

where $c = 1/\sqrt{\epsilon\mu}$ is the speed of light. The quantities $(\mathbf{F}_+, \mathbf{F}_-)$ are the Riemann-Silberstein vectors [Sil07]. The curl operator $\nabla \times$ is an antisymmetric differential operator of the form

$$\begin{pmatrix} 0 & -\partial_z & \partial_y \\ \partial_z & 0 & -\partial_x \\ -\partial_y & \partial_x & 0 \end{pmatrix}. \quad (6.19)$$

By employing the spin-1 Pauli matrices

$$\sigma_x = \begin{pmatrix} 0 & 0 & 0 \\ 0 & 0 & -i \\ 0 & i & 0 \end{pmatrix}, \quad \sigma_y = \begin{pmatrix} 0 & 0 & i \\ 0 & 0 & 0 \\ -i & 0 & 0 \end{pmatrix}, \quad \sigma_z = \begin{pmatrix} 0 & -i & 0 \\ i & 0 & 0 \\ 0 & 0 & 0 \end{pmatrix} \quad (6.20)$$

and with the notation $\vec{\sigma} = (\sigma_x, \sigma_y, \sigma_z)$, the Maxwell's problem can be written in the compact notation:

$$\partial_t \mathbf{F}_\pm = \pm c \vec{\sigma} \cdot \nabla \mathbf{F}_\pm - \mathbf{J}. \quad (6.21)$$

In this form the physical meaning of the Riemann-Silberstein vector emerges naturally: the two component \mathbf{F}_\pm correspond to the electromagnetic field whose helicity, the projection of the spin on the wavevector, is ± 1 .

In the previous section it was shown that a PML approach for the setup of absorbing boundaries corresponds to a gauge transformation of the differential operator under consideration. In applying the same concept to Maxwell's equations one must consider that the equations are invariant under gauge transformation of the form $e^{i\lambda\phi(x)}$ up to a \pm sign w.r.t. each helicity component. Thus, a scaling with $e^{i\lambda\Theta_F(x)x}$ of \mathbf{F}_+ must be followed by a scaling with $e^{-i\lambda\Theta_F(x)x}$ of \mathbf{F}_- .

In one dimension, in Cartesian coordinates, one can set x as the propagation direction, $\mathbf{E} = E\hat{\mathbf{y}}$ and $\mathbf{H} = H\hat{\mathbf{z}}$. Furthermore, the norm of the electric and magnetic fields must be the same $E = H = f(x)$. It is easy to show that the Maxwell's problem for \mathbf{F}_+ reduces to

$$\frac{\partial \mathbf{F}_+}{\partial t} = \sigma_x \partial_x \mathbf{F}_+ = \begin{pmatrix} 0 & 0 & 0 \\ 0 & 0 & -i \\ 0 & i & 0 \end{pmatrix} \begin{pmatrix} 0 \\ 1 \\ i \end{pmatrix} \partial_x f(z) = \begin{pmatrix} 0 \\ 1 \\ i \end{pmatrix} \partial_x f(x) = \partial_x \mathbf{F}_+. \quad (6.22)$$

An analogous result, but with reversed signs, holds for \mathbf{F}_- . Thus, the one dimensional Maxwell's problem can be rewritten as

$$\frac{\partial}{\partial t} \begin{pmatrix} \mathbf{F}_+ \\ \mathbf{F}_- \end{pmatrix} = \begin{pmatrix} \partial_x \mathbb{1} & 0 \\ 0 & -\partial_x \mathbb{1} \end{pmatrix} \begin{pmatrix} \mathbf{F}_+ \\ \mathbf{F}_- \end{pmatrix} \quad (6.23)$$

Let us now perform the scaling of the Maxwell's operator. For illustration purposes, the effect of a simple gauge transform as in Eq. (6.15) is calculated, with the result:

$$\hat{O}_\lambda = U_\lambda \hat{O} U_\lambda^{-1} = \begin{pmatrix} \partial_x + i\lambda\Theta_F(x) & 0 \\ 0 & -\partial_x - i\lambda\Theta_F(x) \end{pmatrix} = \hat{O} - \begin{pmatrix} \lambda & 0 \\ 0 & -\lambda \end{pmatrix} \Theta_F(x). \quad (6.24)$$

Thus, taking a complex λ , for simplicity $\eta = i\lambda$, the spectrum of the right polarized component is shifted above the real axis, while the other below it, as reported in Fig. 6.2 (left). This is to illustrate the effects of violating the symmetry properties of the equations

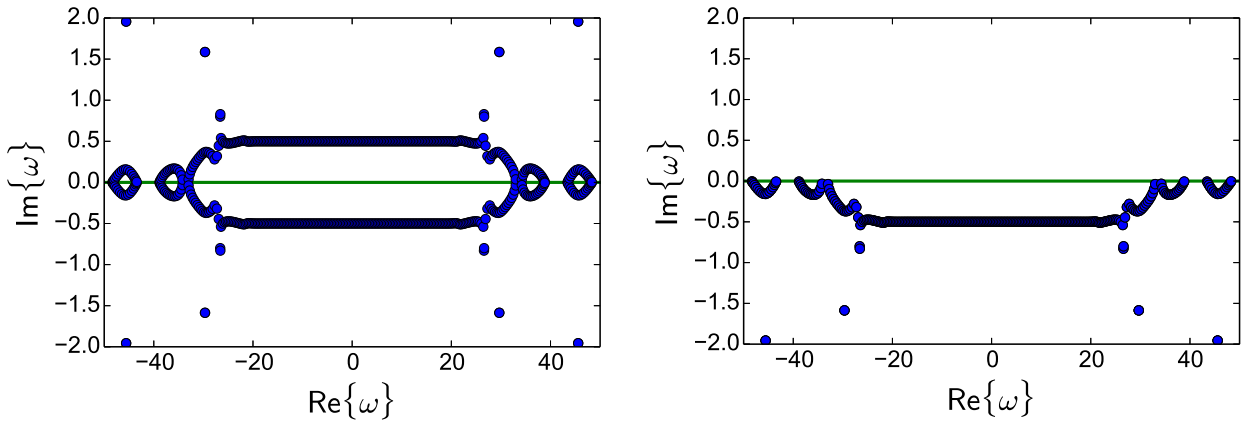


Figure 6.2: Spectrum of the scaled Maxwell operator in one dimension obtained with transformation Eq. (6.23) (left) and with transformation Eq. (6.25) (right). While a scalar gauge transformation of the derivative operators leads to the wrong scaling, respecting the gauge symmetry of the Riemann-Silberstein vectors ensures the correct exponential decay of both $(\mathbf{F}_+, \mathbf{F}_-)$ components simultaneously.

to scale. If the left polarized component \mathbf{F}_- is instead scaled with the term $e^{-i\lambda\Theta_F(x)x}$, the complex scaling transformation becomes

$$U_\lambda = \begin{pmatrix} e^{i\lambda\Theta_F(x)x} & 0 \\ 0 & e^{-i\lambda\Theta_F(x)x} \end{pmatrix}, \quad (6.25)$$

which upon application to \hat{O} yields

$$\hat{O}_\lambda = \hat{O} - \begin{pmatrix} \eta\Theta_F(x) & 0 \\ 0 & \eta\Theta_F(x) \end{pmatrix} = \hat{O} - \eta\Theta_F(x)\mathbb{1}. \quad (6.26)$$

The result of such scaling is reported in Figure 6.2 (right): now both components have their spectrum in the lower half of the complex plane, thus ensuring the desired exponential decay in the scaling region.

6.4 Numerical implementation of 1D scaling

The implementation of the scaling of Maxwell's equations is performed in a finite-element (FE) code named tRecX (*time-dependent Recursive indeX*) [Scr+14], which has been developed with the purpose of solving equations of the type 6.27:

$$i \frac{\partial}{\partial t} \phi[t](x) = \hat{H} \phi[t](x). \quad (6.27)$$

The code automatically creates a recursive index structure which allows handling of complex operators by simply defining them in a string.

The Hamiltonian for the Maxwell equation in 1d is $H = i\sigma_x \partial_x$. A source term of the kind $f(x)g(t)\hat{d}$ is employed, where \hat{d} is the polarization direction. For the determination of the absorption performances, a source with finite support in the time domain was used, like the cosine square function:

$$g(t) = E_0 s_2(t - t_0) \cos(\omega(t - t_0) + \phi_{\text{CEO}}),$$

$$s_n(t) = \begin{cases} \cos^n\left(\frac{\pi t}{T_n}\right) & \text{for } |t| < \frac{T_n}{2} \\ 0 & \text{for } |t| > \frac{T_n}{2} \end{cases}, \quad (6.28)$$

$$T_n = \frac{\pi\tau}{2 \arccos\left(2^{-\frac{1}{2n}}\right)}.$$

The time propagation and absorption in the outer region is shown in Figure 6.3. The dashed vertical lines mark the boundaries of the absorbing regions, which are implemented according to Eq. (6.26). The absorption performances can be tested by varying the parameters relevant for the absorbing region, e.g. the number of discretization coefficients NC , the absorbing region width ℓ and the absorption strength $|\eta|$. The width ℓ can be set equal to one wavelength, which is typically the minimum required in FDTD codes [Osk+10], while obtaining yet very good absorption performances. In Figure 6.4 the amount of reflection from the boundaries of the absorbing region is reported as a function of the number of discretization coefficients and of the absorption strength. The amount of reflection is calculated as the ratio between the norm of the reflected wavefunction and the norm of the wavefunction incident on the absorbing boundaries. A further improvement of the absorption performance can be achieved by employing infinite range basis functions in the absorbing region, as described in [Scr10], which is implemented by using Laguerre's exponentials. The comparison with the finite range basis is given in Figure 6.5.

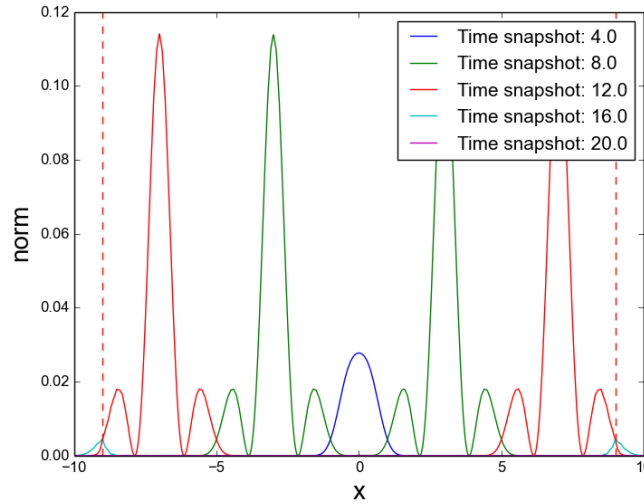


Figure 6.3: Propagation of the e.m. field in the computational box at different time stamps. The source term is localized at the center of the computational box, has a Gaussian spatial profile of $\sigma = 1$ and oscillates in time according to Eq. (6.28). A pair of opposite waves maintaining the temporal profile of the source propagate towards the absorbing regions, marked with dashed lines, where they are absorbed with no reflection.

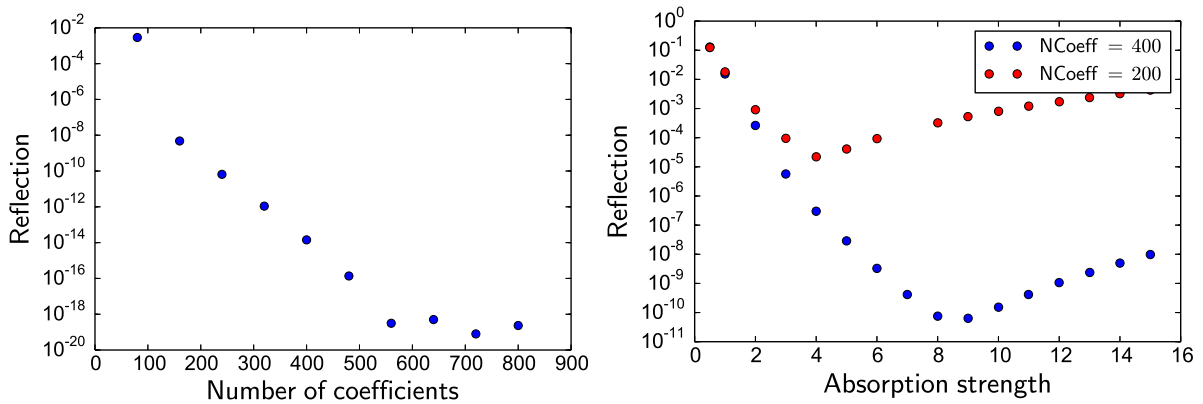


Figure 6.4: The absorption performances of the absorbing boundaries are quantified by the ratio of the norm of the reflected wavefunction and the norm of the incident one. The amount of reflection is reported for fixed absorption strength of $|\eta| = 5$ and varying number of discretization coefficients (left) and for fixed number of discretization coefficients (see legend) and varying absorption strength (right). In the former case it was set $\ell = 5$, in the latter $\ell = 1$.

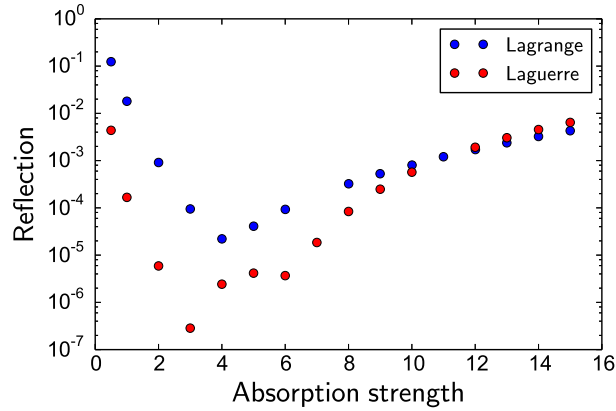


Figure 6.5: Reflection for varying absorption strength for different basis function type in the scaling region. An improvement of the absorption performances for small absorption strength with infinite range gauge scaling is observed.

6.5 Maxwell's equations in two dimensions

In dimensions greater than 1, some of the concepts elucidated in the previous section need to be generalized. It can be shown [BB96] that the wavefunction $\phi = (\mathbf{F}_+, \mathbf{F}_-)$ transforms according to:

$$\phi'(\mathbf{r}', t) = \begin{pmatrix} C & 0 \\ 0 & C^\dagger \end{pmatrix} \phi(\mathbf{r}, t), \quad (6.29)$$

where C is a three dimensional unitary matrix. The previously discussed one dimensional problem can easily be seen as a particular case of the more general one. Any multi-dimensional scaling transformation must be of the form of Eq. (6.29).

The definition of a matrix C capable of extending the absorption performances of the 1D case to 2D is the object of current investigation.

7

Conclusions

The aim of this work was to investigate possible extensions of attosecond physics into the field of plasmonics. The study of plasmonic excitations of both localized (LSPR) and propagating (SPP) type is interesting for a variety of multidisciplinary research fields, given the many technological applications which were demonstrated in the last years.

In this Thesis, ultrafast plasmonics as a mechanism for generating attosecond pulses was the first subject under consideration. The exploitation of plasmonic enhancement for HHG in tapered waveguides, introduced in [Par+11], was the object of extensive numerical study. In the setup used in our investigation, a NIR laser pulse of 800 nm carrier wavelength and 5 fs pulse duration (FWHM) is tightly focused into the large aperture of a silver tapered waveguide. The linearly polarized laser field couples to a cylindrical surface plasmon polariton (cySPP) with almost 100 % conversion efficiency, which propagates till its cutoff radius near the apex of the waveguide. The field intensity enhancement of more than two orders of magnitude allows to generate HHG from the noble gas filling the waveguide. Since the enhancement volume has sub-wavelength dimensions, no phase matching of the XUV harmonics is required.

It is shown that isolated attosecond pulses can be generated in the plasmonic enhancement volume, and that the best collimation properties are obtained for pulses propagating backwards along the waveguide cone. The symmetry of the single plasmonic mode responsible for the field enhancement is imprinted in the perfectly spherical wavefront of the attosecond beam, which makes it very useful for experimental applications. However, because of the small size of the active volume for HHG, the intensity of the attosecond pulse is ultimately smaller than what usually obtained with traditional setups. Therefore, plasmon enhanced attosecond extreme ultraviolet (PEAX) sources should be considered as an alternative in term of usability and affordability.

In the present work was also investigated the possibility of extending attosecond streaking experiments to the imaging of surface plasmon polaritons (SPPs) propagating on nanostructured surfaces. The technique has already been applied to solid Tungsten, and was proven to be capable of determining with attosecond precision the transport properties of photoelectrons inside the solid [Cav+07; Nep+12].

Here, a new technique called “attosecond photoscopia” was proposed, which can be used to probe the dynamics of surface plasmon excitations in the time domain, allowing a retrieval of the transient buildup time of the excitation. The technique is based on the attosecond streak camera and consists in a pump-probe experiment, where the pump is the plasmonic field excited by a NIR pulse. The collinear XUV attosecond pulse acts as a probe, releasing electrons into the plasmonic field, whose final momentum contains the contribution of the accelerating field at the time and position of photoemission. It is shown that the parameters of the streaking plasmonic field can be determined with sub-femtosecond resolution from the analysis of the momentum variance of the photoscopic spectrogram. The setup is thought for normal incidence of both pulses, but as soon as spatial separation of the XUV from the NIR is experimentally available, attosecond photoscopia can be performed for time- and space-imaging of any surface excitation. One excites a surface mode with the NIR pulse, and tailors *in situ* the dynamics of the plasmonic excitation on the supporting surface by shining the XUV attosecond pulse on the region of interest. This could prove of fundamental importance for the study of plasmonic based all-optical circuitry, where the interaction of the propagating plasmonic signal with the components of the chip needs to be carefully determined.

The last topic treated in this Thesis regards the absorbing boundary conditions of Maxwell’s equations. The rigorous operatorial formulation of the standard perfectly matched layer (PML) approach first derived in [SSM14] was presented, and its application to the numerical solution of Maxwell’s equations was discussed. While a successful implementation of the theory in the 1D case was demonstrated, its extension to higher dimension will be the object of future investigation. The aim is to solve the problems of the standard PMLs when applied to the absorption of SPPs propagating on nanostructured surfaces.

Speaking more generally, the study of plasmonic phenomena within the framework of attosecond science is one obvious step for extending attosecond metrology from atoms and molecules to solid state systems. In this sense the study of optical excitations on metal surfaces can be thought as a benchmark for the proposed attosecond photoscopia technique, since the properties of metals are well captured in the random phase approximation, which is intrinsically an equilibrium theory. Thus, it would be very fascinating to apply the attosecond photoscopia to the study of surface optical excitations of systems which cannot be described with simple theories, like strongly correlated materials, or systems which are driven out of equilibrium, accessing thus the ultrafast dynamics of non-linear phenomena.



Check of the numerics for the attosecond photostcopy technique

The experimental transmission spectrum of the grating structure shown in Figure A.1 is compared with the one obtained with our simulation tools. The spectra shown in Figure



Figure A.1: Grating structure of Ref. [Rop+05], used for benchmarking our numerics.

A.2 cast some suspects on the validity of our simulations. The discrepancies however can

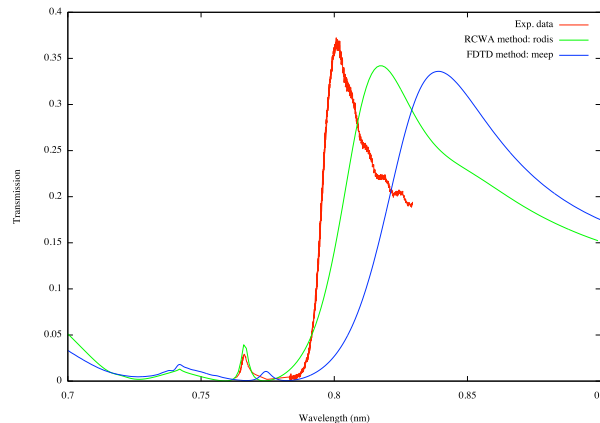


Figure A.2: Comparison among transmission spectra of grating structure reported in Fig. A.1, obtained with the RCWA method and the FDTD method.

be explained with the imperfection of the grating used in the experiments, or with the fact that the FDTD method uses an interpolation of the gold dielectric function taken from [Rak+98b], while the RCWA method uses the tabulated dielectric function from [Pal98].

To figure out the last objection a calculation of the reflectivity spectrum of the grating used in our experimental setup was performed using the RCWA and FDTD method, both with the gold dielectric function taken from Rakic's paper. The comparison is reported in Fig. A.3. Figure A.3 shows that the numerics is good, and any difference between

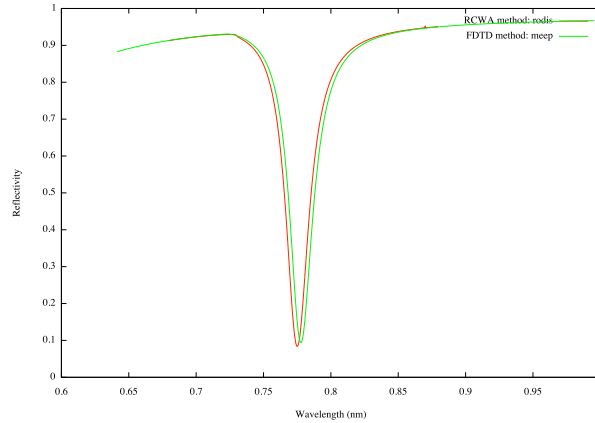


Figure A.3: Comparison of reflectivity spectra of the grating structure obtained with the RCWA method and the FDTD method

the experimental data and the simulations can be attributed to either imperfection of the experimental samples or to differences of the dielectric function taken from [Rak+98b].

Bibliography

- [AD04] P. Agostini and L. F. DiMauro. “The physics of attosecond light pulses”. en. In: *Reports on Progress in Physics* 67.6 (June 2004), pp. 813–855. ISSN: 0034-4885. DOI: 10.1088/0034-4885/67/6/R01.
- [Ago+79] P. Agostini, F. Fabre, G. Mainfray, G. Petite, and N. Rahman. “Free-Free Transitions Following Six-Photon Ionization of Xenon Atoms”. In: *Physical Review Letters* 42.17 (Apr. 1979), pp. 1127–1130. ISSN: 0031-9007. DOI: 10.1103/PhysRevLett.42.1127.
- [All96] P. B. Allen. “From Quantum Mechanics to Technology”. In: ed. by Z. Petru, J. Przystawa, and K. Rapcewicz. Springer, Berlin, 1996, pp. 125–141.
- [Ash+13] B. Ashall, J. F. López-Barberá, E. McClean-Iltén, and D. Zerulla. “Highly efficient broadband ultrafast plasmonics”. EN. In: *Optics Express* 21.22 (Nov. 2013), p. 27383. ISSN: 1094-4087. DOI: 10.1364/OE.21.027383.
- [Bal+03] A. Baltuška, T. Udem, M. Uiberacker, M. Hentschel, E. Goulielmakis, et al. “Attosecond control of electronic processes by intense light fields”. In: *Nature* 421 (2003), p. 611.
- [Bar+96] W. L. Barnes, T. W. Preist, S. C. Kitson, and J. R. Sambles. “Physical origin of photonic energy gaps in the propagation of surface plasmons on gratings”. In: *Physical Review B* 54.9 (1996), pp. 6227–6244. DOI: 10.1103/PhysRevB.54.6227.
- [BB96] I. Bialynicki-Birula. “Photon Wave Function”. In: *Progress in Optics* 36 (1996), pp. 245–294. ISSN: 00796638. DOI: 10.1016/S0079-6638(08)70316-0.
- [BC71] E. Balslev and J. M. Combes. “Spectral properties of many-body Schrödinger operators with dilatation-analytic interactions”. In: *Communications in Mathematical Physics* 22.4 (Dec. 1971), pp. 280–294. ISSN: 0010-3616. DOI: 10.1007/BF01877511.
- [BDE03] W. L. Barnes, A. Dereux, and T. W. Ebbesen. “Surface plasmon subwavelength optics.” In: *Nature* 424.6950 (2003). Ed. by J. Servaes, pp. 824–830.
- [Ber94] J.-P. Berenger. “A perfectly matched layer for the absorption of electromagnetic waves”. In: *Journal of Computational Physics* 114.2 (1994), pp. 185–200. ISSN: 0021-9991. DOI: 10.1006/jcph.1994.1159.
- [BLS71] D. Bradley, B. Liddy, and W. Sleat. “Direct linear measurement of ultrashort light pulses with a picosecond streak camera”. In: *Optics Communications* 2.8 (Jan. 1971), pp. 391–395. ISSN: 00304018. DOI: 10.1016/0030-4018(71)90252-5.

- [BW99] M. Born and E. Wolf. *Principles of Optics: Electromagnetic Theory of Propagation, Interference and Diffraction of Light*. 7th. Cambridge University Press, 1999. ISBN: 0521642221.
- [Cav+07] A. L. Cavalieri, N Müller, T. Uphues, V. S. Yakovlev, A Baltuska, et al. “Attosecond spectroscopy in condensed matter.” In: *Nature* 449.7165 (Oct. 2007), pp. 1029–32. ISSN: 1476-4687. DOI: 10.1038/nature06229.
- [Cha11] Z. Chang. *Fundamentals of Attosecond Optics*. 2011. ISBN: 1420089374.
- [Cho+12] J. Choi, S. Kim, I.-Y. Park, D.-H. Lee, S. Han, et al. “Generation of isolated attosecond pulses using a plasmonic funnel-waveguide”. In: *New Journal of Physics* 14.10 (2012), p. 103038.
- [Cia+14] M. F. Ciappina, J. A. Pérez-Hernández, T. Shaaran, M. Lewenstein, M. Krüger, et al. “High-order-harmonic generation driven by metal nanotip photoemission: Theory and simulations”. In: *Physical Review A* 89.1 (Jan. 2014), p. 013409. ISSN: 1050-2947. DOI: 10.1103/PhysRevA.89.013409.
- [Cin+05] M. Cinchetti, A. Gloskovskii, S. Nepjiko, G. Schönhense, H. Rochholz, et al. “Photoemission Electron Microscopy as a Tool for the Investigation of Optical Near Fields”. In: *Physical Review Letters* 95.4 (July 2005), p. 047601. ISSN: 0031-9007. DOI: 10.1103/PhysRevLett.95.047601.
- [Cin+12] A. Cingoz, D. C. Yost, T. K. Allison, A. Ruehl, M. E. Fermann, et al. “Direct frequency comb spectroscopy in the extreme ultraviolet”. In: *Nature* 482.7383 (2012), pp. 68–71.
- [Cor93] P. Corkum. “Plasma perspective on strong field multiphoton ionization”. In: *Physical Review Letters* 71.13 (Sept. 1993), pp. 1994–1997. ISSN: 0031-9007. DOI: 10.1103/PhysRevLett.71.1994.
- [DD95] B. Dhoedt and D. Delbeke. “RODIS”. 1995.
- [Dit+02] H. Ditlbacher, J. R. Krenn, N. Felidj, B. Lamprecht, G. Schider, et al. “Fluorescence imaging of surface plasmon fields”. In: *Applied Physics Letters* 80.3 (Jan. 2002), p. 404. ISSN: 00036951. DOI: 10.1063/1.1435410.
- [Dit+03] H. Ditlbacher, J. R. Krenn, A. Hohenau, A. Leitner, and F. R. Aussenegg. “Efficiency of local light-plasmon coupling”. In: *Applied Physics Letters* 83.18 (Oct. 2003), p. 3665. ISSN: 00036951. DOI: 10.1063/1.1625107.
- [DL04] R. A. Depine and S. Ledesma. “Direct visualization of surface-plasmon bandgaps in the diffuse background of metallic gratings”. In: *Optics Letters* 29.19 (2004), p. 2216. ISSN: 0146-9592. DOI: 10.1364/OL.29.002216.
- [Dre+02] M. Drescher, M. Hentschel, R. Kienberger, M. Uiberacker, V. Yakovlev, et al. “Time-resolved atomic inner-shell spectroscopy”. In: *Nature* 419.6909 (Oct. 2002), pp. 803–807.

- [Fan41] U. Fano. “The Theory of Anomalous Diffraction Gratings and of Quasi-Stationary Waves on Metallic Surfaces (Sommerfeld’s Waves)”. In: *Journal of the Optical Society of America* 31.3 (Mar. 1941), p. 213. ISSN: 0030-3941. DOI: 10.1364/JOSA.31.000213.
- [Fer+88] M. Ferray, A. L’Huillier, X. F. Li, L. A. Lompre, G. Mainfray, et al. “Multiple-harmonic conversion of 1064 nm radiation in rare gases”. In: *Journal of Physics B: Atomic, Molecular and Optical Physics* 21.3 (Feb. 1988), pp. L31–L35. ISSN: 0953-4075. DOI: 10.1088/0953-4075/21/3/001.
- [FW03] A. L. Fetter and J. D. Walecka. *Quantum Theory of Many-particle Systems*. 2003. Chap. IX. ISBN: 0486428273.
- [Gag11] J. Gagnon. “Attosecond Electron Spectroscopy”. PhD thesis. 2011.
- [Gou+04] E. Goulielmakis, M. Uiberacker, R. Kienberger, A. Baltuska, V. Yakovlev, et al. “Direct Measurement of Light Waves”. In: *Science* 305 (2004), pp. 1267–1269.
- [Gou+08] E. Goulielmakis, M. Schultze, M. Hofstetter, V. S. Yakovlev, J. Gagnon, et al. “Single-Cycle Nonlinear Optics”. In: *Science* 320.5883 (2008), pp. 1614–1617. DOI: 10.1126/science.1157846.
- [Gou+10] E. Goulielmakis, Z.-H. Loh, A. Wirth, R. Santra, N. Rohringer, et al. “Real-time observation of valence electron motion”. In: *Nature* 466.7307 (2010), p. 739. DOI: 10.1038/nature09212.
- [GV+99] F. Garcia-Vidal, J. Sanchez-Dehesa, A. Dechelette, E. Bustarret, T. Lopez-Rios, et al. “Localized surface plasmons in lamellar metallic gratings”. In: *Lightwave Technology, Journal of* 17.11 (Nov. 1999), pp. 2191–2195. ISSN: 0733-8724. DOI: 10.1109/50.803010.
- [GV08] G. Giuliani and G. Vignale. *Quantum Theory of the Electron Liquid*. 2008. ISBN: 0521527961.
- [Hen+01] M. Hentschel, R. Kienberger, C. Spielmann, G. A. Reider, N. Milosevic, et al. “Attosecond metrology.” In: *Nature* 414.6863 (Nov. 2001), pp. 509–13. ISSN: 0028-0836. DOI: 10.1038/35107000.
- [HGD93] B. Henke, E. Gullikson, and J. Davis. “X-Ray Interactions: Photoabsorption, Scattering, Transmission, and Reflection at $E = 50\text{--}30,000$ eV, $Z = 1\text{--}92$ ”. In: *Atomic Data and Nuclear Data Tables* 54.2 (July 1993), pp. 181–342. ISSN: 0092640X. DOI: 10.1006/adnd.1993.1013.
- [HK09] H. Haug and S. W. Koch. *Quantum Theory of the Optical and Electronic Properties of Semiconductors*. World Scientific, 2009, p. 469. ISBN: 981283883X.
- [HK90] H. J. Haug and S. W. Koch. *Quantum Theory of the Optical and Electronic Properties of Semiconductors*. World Scientific, 1990. ISBN: 9810200242.

- [Irv+06] S. Irvine, P. Dombi, G. Farkas, and A. Elezzabi. “Influence of the Carrier-Envelope Phase of Few-Cycle Pulses on Ponderomotive Surface-Plasmon Electron Acceleration”. In: *Physical Review Letters* 97.14 (Oct. 2006), p. 146801. ISSN: 0031-9007. DOI: 10.1103/PhysRevLett.97.146801.
- [Joh10] S. G. Johnson. *Notes on Perfectly Matched Layers (PMLs)*. Tech. rep. 2010.
- [Kel65] L. V. Keldysh. “Ionization in the field of a strong electromagnetic wave”. In: *Soviet Phys. JETP* 20.5 (1965), p. 1307.
- [KI09] F. Krausz and M. Y. Ivanov. “Attosecond physics”. In: *Reviews of Modern Physics* 81.1 (2009), pp. 163–234. ISSN: 0034-6861. DOI: 10.1103/RevModPhys.81.163.
- [Kie+04] R. Kienberger, E. Goulielmakis, M. Uiberacker, A. Baltuska, V. Yakovlev, et al. “Atomic transient recorder.” In: *Nature* 427.6977 (Feb. 2004), pp. 817–21. ISSN: 1476-4687. DOI: 10.1038/nature02277.
- [Kim+08] S. Kim, J. Jin, Y.-J. Kim, I.-Y. Park, Y. Kim, et al. “High-harmonic generation by resonant plasmon field enhancement”. In: *Nature* 453.7196 (2008), pp. 757–760.
- [Kim+12] S. Kim, J. Jin, Y.-J. Kim, I.-Y. Park, Y. Kim, et al. “Kim et al. reply”. In: *Nature* 485.7397 (2012), E1–E3.
- [KKV12] F. Kelkensberg, A. F. Koenderink, and M. J. J. Vrakking. “Attosecond streaking in a nano-plasmonic field”. en. In: *New Journal of Physics* 14.9 (Sept. 2012), p. 093034. ISSN: 1367-2630. DOI: 10.1088/1367-2630/14/9/093034.
- [Kra+14] C. M. Krauter, J. Schirmer, C. R. Jacob, M. Pernpointner, and A. Dreuw. “Plasmons in molecules: microscopic characterization based on orbital transitions and momentum conservation.” In: *The Journal of chemical physics* 141.10 (Oct. 2014), p. 104101. ISSN: 1089-7690. DOI: 10.1063/1.4894266.
- [Kre71] E. Kretschmann. “Die Bestimmung optischer Konstanten von Metallen durch Anregung von Oberflächenplasmaschwingungen”. In: *Zeitschrift für Physik* 241.4 (Aug. 1971), pp. 313–324. ISSN: 1434-6001. DOI: 10.1007/BF01395428.
- [KSH11] M. Krüger, M. Schenk, and P. Hommelhoff. “Attosecond control of electrons emitted from a nanoscale metal tip.” In: *Nature* 475.7354 (July 2011), pp. 78–81. ISSN: 1476-4687. DOI: 10.1038/nature10196.
- [KSK93] K. C. Kulander, K. J. Schafer, and J. L. Krause. “Dynamics of short-pulse excitation, ionization and harmonic conversion”. In: *Proceedings of the Workshop, Super Intense Laser Atom Physics (SILAP) III, edited by B. Piraux (Plenum, New York)* (1993).
- [Kub+05] A. Kubo, K. Onda, H. Petek, Z. Sun, Y. S. Jung, et al. “Femtosecond imaging of surface plasmon dynamics in a nanostructured silver film.” In: *Nano letters* 5.6 (June 2005), pp. 1123–7. ISSN: 1530-6984. DOI: 10.1021/nl10506655.

- [LKS13] M. Lupetti, M. F. Kling, and A. Scrinzi. “Plasmon-Enhanced-Attosecond-Extreme Ultraviolet Source”. In: *Physical Review Letters* 110.22 (May 2013), p. 223903. ISSN: 0031-9007. DOI: 10.1103/PhysRevLett.110.223903.
- [Lup+14] M. Lupetti, J. Hengster, T. Uphues, and A. Scrinzi. “Attosecond Photoscopy of Plasmonic Excitations”. In: *Physical Review Letters* 113.11 (Sept. 2014), p. 113903. ISSN: 0031-9007. DOI: 10.1103/PhysRevLett.113.113903.
- [Mai07] S. A. Maier. *Plasmonics: Fundamentals and Applications*. Springer, 2007. ISBN: 9780387331508.
- [Mos14] R. Moshhammer. <http://www.mpi-hd.mpg.de/pfeifer/page.php?id=145>. 2014.
- [Mul02] H. G. Muller. “Reconstruction of attosecond harmonic beating by interference of two-photon transitions”. In: *Appl. Phys. B* 74 (2002), S17.
- [Nep+12] S. Neppl, R. Ernstorfer, E. M. Bothschafter, A. L. Cavalieri, D. Menzel, et al. “Attosecond Time-Resolved Photoemission from Core and Valence States of Magnesium”. In: *Physical Review Letters* 109.8 (Aug. 2012), p. 087401. ISSN: 0031-9007. DOI: 10.1103/PhysRevLett.109.087401.
- [NH94] L. Novotny and C. Hafner. “Light propagation in a cylindrical waveguide with a complex, metallic, dielectric function”. In: *Physical Review E* 50.5 (Nov. 1994), pp. 4094–4106. ISSN: 1063-651X. DOI: 10.1103/PhysRevE.50.4094.
- [Oga+97] S. Ogawa, H. Nagano, H. Petek, and A. P. Heberle. “Optical Dephasing in Cu(111) Measured by Interferometric Two-Photon Time-Resolved Photoemission”. In: *Physical Review Letters* 78.7 (Feb. 1997), pp. 1339–1342. ISSN: 0031-9007. DOI: 10.1103/PhysRevLett.78.1339.
- [Osk+10] A. F. Oskooi, D. Roundy, M. Ibanescu, P. Bermel, J. Joannopoulos, et al. “Meep: A flexible free-software package for electromagnetic simulations by the FDTD method”. In: *Computer Physics Communications* 181.3 (2010), pp. 687–702.
- [Ott68] A. Otto. “Excitation of nonradiative surface plasma waves in silver by the method of frustrated total reflection”. In: *Zeitschrift für Physik A Hadrons and Nuclei* 216.4 (1968), pp. 398–410.
- [Ozb06] E. Ozbay. “Plasmonics: merging photonics and electronics at nanoscale dimensions.” In: *Science* 311.5758 (2006), pp. 189–193. ISSN: 1095-9203. DOI: 10.1126/science.1114849.
- [Pal98] E. D. Palik. *Handbook of Optical Constants of Solids*. Academic Press, 1998, p. 999. ISBN: 0080533787.
- [Par+11] I.-Y. Park, S. Kim, J. Choi, D.-H. Lee, Y.-J. Kim, et al. “Plasmonic generation of ultrashort extreme-ultraviolet light pulses”. In: *Nature Photonics* 5.11 (Oct. 2011), pp. 677–681. ISSN: 1749-4885. DOI: 10.1038/nphoton.2011.258.

- [Par+13] I.-Y. Park, J. Choi, D.-H. Lee, S. Han, S. Kim, et al. “Generation of EUV radiation by plasmonic field enhancement using nano-structured bowties and funnel-waveguides”. In: *Ann. Phys.* 525.1 (2013), p. 87.
- [Pau+01] P. M. Paul, E. S. Toma, P. Breger, G. Mullot, F. Auge, et al. “Observation of a train of attosecond pulses from high harmonic generation.” In: *Science (New York, N. Y.)* 292.5522 (2001), pp. 1689–1692. ISSN: 0036-8075. DOI: 10.1126/science.1059413.
- [Pau+94] G. Paulus, W. Nicklich, H. Xu, P. Lambropoulos, and H. Walther. “Plateau in above threshold ionization spectra”. In: *Physical Review Letters* 72.18 (May 1994), pp. 2851–2854. ISSN: 0031-9007. DOI: 10.1103/PhysRevLett.72.2851.
- [Pit+07] J. M. Pitarke, V. M. Silkin, E. V. Chulkov, and P. M. Echenique. “Theory of surface plasmons and surface-plasmon polaritons”. en. In: *Reports on Progress in Physics* 70.1 (Jan. 2007), pp. 1–87. ISSN: 0034-4885. DOI: 10.1088/0034-4885/70/1/R01.
- [Ple+05] A. Plech, V. Kotaidis, M. Lorenc, and J. Boneberg. “Femtosecond laser near-field ablation from gold nanoparticles”. In: *Nature Physics* 2.1 (Dec. 2005), pp. 44–47. ISSN: 1476-0000. DOI: 10.1038/nphys191.
- [Pre+13] J. S. Prell, L. J. Borja, D. M. Neumark, and S. R. Leone. “Simulation of attosecond-resolved imaging of the plasmon electric field in metallic nanoparticles”. In: *Annalen der Physik* 525.1-2 (Feb. 2013), pp. 151–161. ISSN: 00033804. DOI: 10.1002/andp.201200201.
- [Rak+98a] A. D. Rakić, A. B. Djurišić, J. M. Elazar, and M. L. Majewski. “Optical properties of metallic films for vertical-cavity optoelectronic devices”. In: *Appl. Opt.* 37.22 (1998), pp. 5271–5283. DOI: 10.1364/AO.37.005271.
- [Rak+98b] A. D. Rakic, A. B. Djurišić, J. M. Elazar, and M. L. Majewski. “Optical Properties of Metallic Films for Vertical-Cavity Optoelectronic Devices”. In: *Applied Optics* 37.22 (Aug. 1998), p. 5271. ISSN: 0003-6935. DOI: 10.1364/AO.37.005271.
- [Ram91] J. Rammer. “Quantum transport theory of electrons in solids: A single-particle approach”. In: *Rev. Mod. Phys.* 63 (4 1991), pp. 781–817. DOI: 10.1103/RevModPhys.63.781.
- [Ras13] M. B. Raschke. “High-harmonic generation with plasmonics: feasible or unphysical?” In: *Annalen der Physik* 525.3 (2013), A40–A42. ISSN: 1521-3889. DOI: 10.1002/andp.201300721.
- [Rau+08] S. Rausch, T. Binhammer, A. Harth, J. Kim, R. Ell, et al. “Controlled waveforms on the single-cycle scale from a femtosecond oscillator”. In: *Optics Express* 16.13 (2008), p. 9739. ISSN: 1094-4087. DOI: 10.1364/OE.16.009739.

- [Rem+06] T. Remetter, P. Johnsson, J. Mauritsson, K. Varju, Y. Ni, et al. “Attosecond electron wave packet interferometry”. In: *Nature Physics* 2.5 (2006), p. 323. DOI: 10.1038/nphys290.
- [Rit+68] R. Ritchie, E. Arakawa, J. Cowan, and R. Hamm. “Surface-Plasmon Resonance Effect in Grating Diffraction”. In: *Physical Review Letters* 21.22 (Nov. 1968), pp. 1530–1533. ISSN: 0031-9007. DOI: 10.1103/PhysRevLett.21.1530.
- [Rop+05] C. Ropers, D. J. Park, G. Stibenz, G. Steinmeyer, J. Kim, et al. “Femtosecond light transmission and subradiant damping in plasmonic crystals”. In: *Physical Review Letters* 94.11 (2005), p. 113901.
- [Rop+07] C. Ropers, T. Elsaesser, G. Cerullo, M. Zavelani-Rossi, and C. Lienau. “Ultrafast optical excitations of metallic nanostructures: from light confinement to a novel electron source”. In: *New Journal of Physics* 9.10 (2007), p. 397.
- [RZR12] G. Ruffato, G. Zacco, and F. Romanato. “Innovative Exploitation of Grating-Coupled Surface Plasmon Resonance for Sensing”. en. In: ed. by K. Y. Kim. InTech, Oct. 2012. Chap. 17. ISBN: 978-953-51-0797-2. DOI: 10.5772/2633.
- [Sch+02] O. Schmidt, M. Bauer, C. Wiemann, R. Porath, M. Scharte, et al. “Time-resolved two photon photoemission electron microscopy”. In: *Applied Physics B* 74.3 (Feb. 2002), pp. 223–227. ISSN: 0946-2171. DOI: 10.1007/s003400200803.
- [Sch+13] A. Schiffrin, T. Paasch-Colberg, N. Karpowicz, V. Apalkov, D. Gerster, et al. “Optical-field-induced current in dielectrics.” In: *Nature* 493.7430 (Jan. 2013), pp. 70–4. ISSN: 1476-4687. DOI: 10.1038/nature11567.
- [Scr+14] A. Scrinzi, J. Liss, A. Zilinski, and V. Majety. “tRecX - time-dependent recursive indexing code”. In: (*unpublished*) (2014).
- [Scr10] A. Scrinzi. “Infinite-range exterior complex scaling as a perfect absorber in time-dependent problems”. In: *Physical Review A* 81.5 (2010), pp. 1–10. ISSN: 1050-2947. DOI: 10.1103/PhysRevA.81.053845.
- [Sha+12] B. Sharma, R. R. Frontiera, A.-I. Henry, E. Ringe, and R. P. Van Duyne. “SERS: Materials, applications, and the future”. In: *Materials Today* 15.1-2 (Jan. 2012), pp. 16–25. ISSN: 13697021. DOI: 10.1016/S1369-7021(12)70017-2.
- [Sil07] L. Silberstein. “Elektromagnetische Grundgleichungen in bivectorieller Behandlung”. In: *Annalen der Physik* 327.3 (1907), pp. 579–586. ISSN: 00033804. DOI: 10.1002/andp.19073270313.
- [Sim79] B. Simon. “The definition of molecular resonance curves by the method of exterior complex scaling”. In: *Physics Letters A* 71.2-3 (Apr. 1979), pp. 211–214. ISSN: 03759601. DOI: 10.1016/0375-9601(79)90165-8.
- [Siv+12] M. Siviš, M. Duwe, B. Abel, and C. Ropers. “Nanostructure-enhanced atomic line emission”. In: *Nature* 485.7397 (2012), E1–E3.

- [Siv+13] M. Sivis, M. Duwe, B. Abel, and C. Ropers. “Extreme-ultraviolet light generation in plasmonic nanostructures”. In: *Nature Physics* 9.5 (2013), pp. 304–309.
- [SK11] F. Süssmann and M. F. Kling. “Attosecond nanoplasmonic streaking of localized fields near metal nanospheres”. In: *Physical Review B* 84.12 (2011).
- [Sol+06] I. J. Sola, E. Mevel, L. Elouga, E. Constant, V. Strelkov, et al. “Controlling attosecond electron dynamics by phase-stabilized polarization gating”. In: *Nature Physics* 2.5 (2006), p. 319. ISSN: 1745-2473. DOI: 10.1038/nphys281.
- [SSM14] A. Scrinzi, H. Stimming, and N. Mauser. “On the non-equivalence of perfectly matched layers and exterior complex scaling”. In: *Journal of Computational Physics* 269 (July 2014), pp. 98–107. ISSN: 00219991. DOI: 10.1016/j.jcp.2014.03.007.
- [Sto+07] M. I. Stockman, M. F. Kling, U. Kleineberg, and F. Krausz. “Attosecond nanoplasmonic-field microscope”. In: *Nature Photonics* 1.9 (2007), p. 539. DOI: 10.1038/nphoton.2007.169.
- [Sto04] M. Stockman. “Nanofocusing of Optical Energy in Tapered Plasmonic Waveguides”. In: *Physical Review Letters* 93.13 (Sept. 2004), p. 137404. ISSN: 0031-9007. DOI: 10.1103/PhysRevLett.93.137404.
- [Str41] J. A. Stratton. *Electromagnetic theory*. McGraw Hill Book Company, 1941.
- [Szi+94] R. Szipocs, K. Ferencz, C. Spielmann, and F. Krausz. “Chirped multilayer coatings for broadband dispersion control in femtosecond lasers”. In: *Optics Letters* 19.3 (Feb. 1994), p. 201. ISSN: 0146-9592. DOI: 10.1364/OL.19.000201.
- [Taf05] A. Taflove. *Computational Electrodynamics: The Finite - Difference Time - Domain Method*. 3rd ed. Artech House, 2005. ISBN: 0890067929.
- [TGB99] G. Tempea, M. Geissler, and T. Brabec. “Phase sensitivity of high-order harmonic generation with few-cycle laser pulses”. In: *Journal of the Optical Society of America B* 16.4 (Apr. 1999), p. 669. ISSN: 0740-3224. DOI: 10.1364/JOSAB.16.000669.
- [Wac+12] G. Wachter, C. Lemell, J. Burgdörfer, M. Schenk, M. Krüger, et al. “Electron rescattering at metal nanotips induced by ultrashort laser pulses”. In: *Physical Review B* 86.3 (July 2012), p. 035402. ISSN: 1098-0121. DOI: 10.1103/PhysRevB.86.035402.
- [Wey19] H. Weyl. “Ausbreitung elektromagnetischer Wellen über einem ebenen Leiter”. In: *Annalen der Physik* 365.21 (1919), pp. 481–500. ISSN: 00033804. DOI: 10.1002/andp.19193652104.

- [Wim+14] L. Wimmer, G. Herink, D. R. Solli, S. V. Yalunin, K. E. Echternkamp, et al. “Terahertz control of nanotip photoemission”. In: *Nature Physics* 10.6 (May 2014), pp. 432–436. ISSN: 1745-2473. DOI: 10.1038/nphys2974.
- [Woo02] R. Wood. “On a remarkable case of uneven distribution of light in a diffraction grating spectrum”. In: *Philos. Mag.* 4 (1902), pp. 396,402.
- [ZB07] R. Zia and M. L. Brongersma. “Surface plasmon polariton analogue to Young’s double-slit experiment.” In: *Nature nanotechnology* 2.7 (July 2007), pp. 426–9. ISSN: 1748-3395. DOI: 10.1038/nnano.2007.185.
- [Zha+12] K. Zhao, Q. Zhang, M. Chini, Y. Wu, X. Wang, et al. “Tailoring a 67 attosecond pulse through advantageous phase-mismatch”. In: *Opt. Lett.* 37.18 (2012), pp. 3891–3893.
- [ZMC11] D. Zhang, L. Men, and Q. Chen. “Microfabrication and applications of opto-microfluidic sensors.” en. In: *Sensors (Basel, Switzerland)* 11.5 (Jan. 2011), pp. 5360–82. ISSN: 1424-8220. DOI: 10.3390/s110505360.

Acknowledgments

I would like to thank my supervisor Prof. Armin Scrinzi for giving me the opportunity to conduct my research in a prestigious university such as the LMU Munich. In these three and a half years he always patiently guided my work, granting me the freedom to go after my personal interests and to work independently. For this, I am very grateful.

My thanks go also to my second supervisor Prof. Norbert Mauser, for covering the mathematical aspects of the numerical simulations performed in this thesis and extending my work in the form of a Co-tutelle between the Fak. Physik at LMU München and the Fak. Mathematik at Univ. Wien. Being a member of the Viennese FWF “doctoral school on nonlinear PDEs” was a very positive exchange experience and an invaluable occasion of further personal development.

I am also grateful for the continuous funding of my thesis by the FWF (Austrian Science Foundation), the SFB “Vienna Computational Materials Laboratory” (project No. F41), where my 2 PhD advisors jointly lead the subproject “dynamical correlated systems”, and by the MAP (Munich-Center for Advanced Photonics) project.

Another special thank go to Prof. Thorsten Uphues and Julia Hengster, for giving me the possibility through their experimental expertise, to let my work on “Attosecond Photoscopy” become real. Thorsten’s curiosity and enthusiasm for physics have been very stimulating throughout our scientific collaboration.

I am also very thankful to Prof. Matthias Kling, for providing useful insights and advices during the first part of my work, and also for assuming the role of coordinator of the International Max Planck Research School (IMPRS) of Advance Photon Science.

This brings me to thank all the people involved in the school, in primis the other coordinators Dr. Nicholas Karpowicz and Dr. habil. Vladislav Yakovlev, and the wonderful secretary Mrs. Wild. Meeting all the people from the school was a real privilege, and a great source of fun too. Further thanks go to Ass. Prof. Hans Peter Stimming for the advices on numerics and to Viennese colleagues of the SFB VICOM and the FWF doctoral school for the frequent exchanges we had.

Surviving the bureaucracy would have been impossible without Mrs. Stefanie Preuss (Univ. Wien) and Mrs. Ute Tobiasch (LMU), who kindly helped me in all aspects of administration.

Also, I would like to thank my officemates and colleagues for sharing our everyday life and giving each other support. A special thanks goes to Alejandro and Andreas for helping me with the “Zusammenfassung”, and to Kalle, for the huge amount of IT advices I received from him.

Staying abroad would have been much less enjoyable if it weren’t for my friends of the IMPRS school and the MCC association. So, thank you for all the amazing time we spent together!

I ringraziamenti finali vanno alla mia famiglia. Anche se non accetteranno mai la

distanza che ci separa, mi hanno sempre sostenuto in tutte le mie scelte. Infine, ringrazio la mia ragazza Giulia per tutto l'amore e l'affetto che mi dona ogni giorno. Senza di lei, la mia vita non sarebbe così vivace.

Mattia Lupetti

Address Lindwurmstraße 169,
80337, Munich, Germany
Telephone +49 176 30 711 778
Email Mattia.Lupetti@physik.uni-muenchen.de
Date of Birth 6 August 1987
Place of Birth Montegranaro (FM), Italy



Education

- 2011 **PhD Candidate**, joint project between the *Ludwig-Maximilians-Universität* (München, Germany) and the *Universität Wien* (Vienna, Austria).
Modeling and simulation of the interplay of ultrashort XUV pulses with surface optical excitations.
- 2011 **Laurea Magistrale in Fisica**, *Università di Pisa*, Pisa, Italy.
110/110 *cum laude*
Equivalent of MSc. Focus on Plasma Physics, Solid State Physics, Photonics, Fluid Mechanics.
- 2010 **Internship**, *LULI, École Polytechnique*, Paris, France.
Investigation of the influence of surface wave excitation at metal surfaces on laser-solid energy transfer in a regime of interest for inertial confinement fusion and fast ignition.
- 2009 **Laurea in Fisica**, *Università di Pisa*, Pisa, Italy.
110/110 *cum laude*
Equivalent of BSc. Major: Physics.

Scholarships & Fellowships

Study

- 2012 **Fellow of IMPRS-APS**, *MPI für Quantenoptik*, Garching, Germany.
International Max Planck Research School of Advanced Photon Science
- 2010 **Erasmus scholarship**, *Université Paris XI*, Paris, France.
- 2009 **SIF Scholarship**, *Società Italiana di Fisica*, Pisa, Italy.
"Progetto lauree scientifiche", 3-years scholarship funded by the Italian Physical Society.

Languages

Italian	Mother tongue	C2
English	Fluent	C1/C2
German	Fluent	C1
French	Fluent	B2/C1

Computer skills

Development

Languages C, C++, Python, Matlab
Frameworks Django

Web HTML, CSS, JavaScript
VCS Git

Office and Tools

Operating Systems Ubuntu, Linux, Mac OS, Windows
Graphics Gimp, Inkscape

Office OpenOffice/LibreOffice, Microsoft Office, iWork
Editing T_EX, L^AT_EX

Scientific activity & Awards

Book contribution *M. Lupetti and A. Scrinzi (2015). Attosecond XUV Pulses and Surface Plasmon Polaritons: Two Case Studies. In: Kitzler, M. and Gräfe, S., ed. Ultrafast dynamics driven by intense light pulses. From atoms to solids, from lasers to intense X-rays. Springer Series on Atomic, Optical, and Plasma Physics. In publication.*

Publication *M. Lupetti, J. Hengster, T. Uphues and A. Scrinzi. Phys. Rev. Lett. 113, 113903 (2014).*

Publication *M. Lupetti, M. F. Kling and A. Scrinzi. Phys. Rev. Lett. 110, 223903 (2013).*

Conference Presentation *Attosecond Photocopy: Imaging the Excitation of Surface Plasmon Polaritons. M. Lupetti. International Conference on Free Electron Lasers and Attosecond Light Sources (AttoFEL 2014), UCL, London, UK.*

Invited Presentation *Attosecond Photocopy: Imaging the Excitation of Surface Excitations. M. Lupetti. GRK Colloquium, Hamburg University, Germany.*

Best Poster Prize *High Power Laser-Grating Interaction. M. Lupetti, A. Macchi, C. Riconda. International Workshop on Laser-Plasma Interaction at Ultra-High Intensity, Dresden, Germany.*

Interests

Cooking Mediterranean cuisine.
Literature Science Fiction (American 50s-70s), History, Geopolitics, Comics.
Sport Soccer, Volleyball, Hiking.

Extra

Participation to the "app@night" of the LMU Entrepreneurship Center. 2 days event about the creation and development of a smartphone app.

Participation to the "DataCrunch2015" of the LMU Entrepreneurship Center. Workshop on data science, predictive modeling and machine learning.